Dissertation

Novel Techniques of Cavity Enhanced Spectroscopy for Trace Gas Sensing

A thesis submitted for the degree of

Doctor of Technical Sciences (Dr. techn.)

at

Technische Universität Wien

Faculty of Technical Chemistry

Institute of Chemical Technologies and Analytics

under supervision of

Univ. Prof. Dr. Bernhard Lendl

defended by

DI Jakob Hayden

Mat.Nr. 00928812

Wien, September 2019

Kurzfassung

Die Bedeutung der Messung von Molekülkonzentrationen in Gasen erstreckt sich über so unterschiedliche Gebiete wie Immissions- und Emissionsüberwachung, Arbeitsplatzsicherheit und die Analyse von Prozessgasen in der chemischen Industrie. Unter den Messmethoden für Gase und Spurengase zeichnet sich die Infrarotspektroskopie neben weiteren Vorteilen dadurch aus, dass Messungen ohne Einsatz von Reagenzien in Echtzeit direkt am „Ort des Geschehens“, also ohne Probenahme, erfolgen können. Für neue Entwicklungen und Anwendungen der Infrarotspektroskopie kommen meist Halbleiterlaser als Lichtquellen zum Einsatz. Diese wurden in den letzten beiden Jahrzehnten, insbesondere mit der Einführung des Quantenkaskadenlasers, rasant weiterentwickelt und haben damit die Erforschung neuer, immer empfindlicherer Techniken der laserbasierten Infrarotspektroskopie beflügelt. Die nachweisstärksten dieser Techniken nutzen die Erhöhung der Interaktionsstrecke zwischen Licht und Probe in optischen Resonatoren hoher Finesse, die auch als „optische Kavitäten“ bezeichnet werden. Diese Techniken werden unter dem Begriff „Resonatorverstärkte Spektroskopie“ zusammengefasst (engl. „cavity enhanced spectroscopy“).

Die vorliegende Arbeit untersucht insbesondere zwei zum gegenwärtigen Zeitpunkt unkonventionelle Vertreter resonatorverstärkter Infrarotspektroskopie: Quartz-verstärkte photoakustische Spektroskopie mit Resonatorverstärkung (I-QEPAS) und Cavity Ring-Down Faraday-Rotations-Spektroskopie (CRD-FRS). QEPAS basiert auf der Detektion von Schall, der durch den photoakustischen Effekt in der Probe entsteht, wenn Licht modulierter Intensität oder Wellenläng absorbiert wird. Der Faraday-Rotations-Spektroskopie und der CRD-FRS liegt hingegen der Faraday-Effekt zu Grunde. Dieser bezeichnet die Änderung der Orientierung linear polarisaten Lichts beim Durchtritt durch eine geeignete Probe, wenn ein zur Ausbreitungsrichtung parallel orientiertes magnetisches Feld angelegt wird.

Der größte Teil der Dissertation ist dem Konzipieren und der Realisierung eines experimentellen Aufbaus für die I-QEPAS basierte Messung von Kohlenmonoxid (CO) im mittleren infraroten Spektralbereich gewidment. Für die Resonatorverstärkung kam ein bisher wenig beachtetes Design optischer Kavitäten zum Einsatz: die Fabry-Pérot Kavität mit Brewsterfenster. Die über den Einfallswinkel variable Reflektivität des Brewsterfensters ermöglichte die Maximierung der in der Kavität zirkulierenden optischen Leistung. Darüber hinaus erlaubte dieses Design die Ausnutzung optischer Rückkopplung zwischen der Kavität und dem eingesetzten Quantenkaskadenlaser, um die Wellenlänge des Lasers zu stabilisieren. Dadurch wurde Licht effizient in die Kavität eingekoppelt und die optische Leistung von 25 mW außerhalb der Kapität auf 6.3 W am Punkt der Messung innerhalb der Kavität erhöht. Die Empfindlichkeit photoakustischer Messungen wurde dadurch entsprechend gesteigert, wodurch das Detektionslimit für CO auf unter 1 ppb (ein Teil in

einer Milliarde) gesenkt wurde. Die sehr hohe optische Intensität führte aber auch zu gesättigter Absorption durch CO. Der Einfluss gesättigter Absorption auf I-QEPAS – Messungen von CO wurde basierend auf bestehender Theorie der gesättigten Absorption quantitativ beschrieben und experimentell untersucht.

Allgemein ist es ein wesentliches Ziel dieser Arbeit, den experimentellen Arbeiten und Ergebnissen aus dem Labor ihren theoretischen Kontext zur Seite zu stellen und so ein tieferes Verständnis der beobachteten Vorgänge zu erhalten. Neben der Darstellung der entsprechenden Theorie ergänzen daher an mehren Stellen Simulationen die experimentellen Ergebnisse. Beispielsweise wurde der physikalische Entstehungsprozess photoakustischer Signale im Detail modelliert. Dadurch konnte der zunächst überraschende Verlauf des von CO ausgehenden photoakustischen Signals mit zunehmender Luftfeuchtigkeit als eine Konsequenz einer transienten, „kinetischen Abkühlung“ verstanden und quantitativ beschrieben werden.

Die experimentelle Arbeit zur zweiten untersuchten Technik der resonatorverstärkten Spektroskopie, CRD-FRS, wurde im Zuge eines zweimonatigen Aufenthalts an der Princeton University, USA, in der Forschungsgruppe von Prof. Dr. Gerard Wysocki durgeführt. Ein bestehender Aufbau zur Messung von Sauerstoff, anhand dessen CRD-FRS von Dr. Jonas Westberg und Prof. Dr. Gerard Wysocki kurz vor dem Aufenthalt demonstriert worden war, wurde experimentell weitereintickelt. Die Verbesserungen umfassten die Stabilisierung der Wellenlänge der Messung auf einen schwachen optischen Übergang von Sauerstoff bei 762.7 nm. Außerdem wurde der eingesetzte Diodenlaser mittels der Pound-Drever-Hall - Technik auf eine Resonanz der optischen Kavität stabilisiert, wodurch Konzentrationsbestimmungen mit einer wesentlich höheren Rate als zuvor von bis zu 9 kHz durchgeführt werden konnten. Im Vergleich zu anderen spekroskopischen Techniken ist CRD-FRS besonders geeignet für Messungen bei fester, auf eine Übergangsfrequenz des Analyten stabilisierter Wellenlänge, da der Verlust spektraler Information durch die zusätzliche Selektivität der Faraday-Rotations-Spektroskopie kompensiert wird. Darüber hinaus sind CRD-FRS - Messungenen unabhängig von Hintergrundsignalen, die nicht von der Probe herrühren (schwankende Laserleistung, Verluste der leeren Kavität), wodurch keine Hintergrundmessungen nötig sind und die Wellenlänge somit dauerhaft auf den Übergang des Analyten fixiert werden kann.

Die Abfassung der vorliegenden Dissertation als Monografie zielt darauf ab, einige zusätzliche Überlegungen und Ergebnisse in einem Umfang zu diskutieren, der oftmals mit der knappen Darstellung in wissenschaftlichen Publikationen schwer in Einklang zu bringen ist. Die Kurzfassungen der Publikationen, die im Lauf dieser Dissertation mit mir als Autor oder Mitautor entstanden sind, sind dem Dokument in einem Appendix angehängt.

Abstract

The relevance of measuring molecular concentrations in gases extends to such divers fields as ambient air – and emission monitoring, occupational health and safety and the analysis of process gases in the chemical industries. Amongst the various methods of gas- and trace gas sensing, infrared spectroscopy stands out, amongst other advantages, for the possibility of taking measurements in real time without the application of reagents directly at the point of interest, without taking a sample. Semiconductor lasers are now widely employed in the development of novel techniques and applications of infrared spectroscopy. These lasers have been improved tremendously over the past two decades or so, in particular with the introduction of quantum cascade lasers, and have thereby nourished the research in techniques of infrared spectroscopy of ever increasing sensitivity. The most sensitive amongst these techniques make use of the enhancement of the effective interaction pathlength between light and the sample in optical resonators of high finesse, that are also called "optical cavities". These techniques are summarized by the term "cavity enhanced spectroscopy".

The thesis at hand investigates two techniques of cavity enhanced infrared spectroscopy that to date are rather unconventional: Intracavity Quartz-Enhanced Photoacoustic Spectroscopy (I-QEPAS) and Cavity Ring-Down Faraday-Rotation Spectroscopy (CRD-FRS). QEPAS is based on detecting sound that is generated in the sample via the photoacoustic effect when light of modulated intensity or wavelength is absorbed. On the contrary, Faraday-rotation spectroscopy and CRD-FRS make use of the Faraday effect. This effect describes the change in orientation of linearly polarized light upon transmission through a suited sample, if a magnetic field is applied that is oriented parallel to the direction of propagation.

The largest part of the thesis is dedicated to the design and realization of an experimental setup for the measurement of carbon monoxide (CO) using I-QEPAS in the mid-infrared spectral range. For achieving cavity enhancement, a seldom employed cavity design was chosen: the Brewster window cavity. The variable reflectivity of the Brewster window, depending on its angle, allowed maximizing the optical power circulating inside the cavity. Furthermore, this cavity design enabled using optical feedback from the cavity to a quantum cascade laser to stabilize the wavelength of the laser. Thereby, light was efficiently coupled into the cavity and the optical power was enhanced from 25 mW outside the cavity to 6.3 W inside the cavity at the point of measurement. The sensitivity of photoacoustic measurements was increased accordingly, yielding a detection limit for CO below 1 ppb (one part in a billion by volume). The very high optical intensity, however, also gave rise to saturated absorption of CO. The influence of saturated absorption on I-QEPAS measurements of CO was investigated experimentally and described quantitatively based on existing theory of saturated absorption.

In general, one aim of this thesis is to also provide the theoretical context of the presented experimental observations and thereby obtain a deepened understanding of the studied processes. For this reason, simulations complement several experimental results. For example, the physical formation of photoacoustic signals was modelled in detail. Thereby, the peculiar trend of the photoacoustic signal of CO with increasing humidity of the gas could be understood as a consequence of a transient, “kinetic cooling” effect and described quantitatively in simulation.

The experimental work concerning the second technique of cavity enhanced spectroscopy, CRD-FRS, was carried out in the research group of Prof. Dr. Gerard Wysocki at Princeton University, USA, during a two month visit. An existing experimental setup for the measurement of molecular oxygen, that had been developed recently for the demonstration of CRD-FRS by Dr. Jonas Westberg and Dr. Gerard Wysocki, was further improved. The wavelength of measurements was stabilized to a weak optical transition of O_2 at 762.7 nm. Also, the diode laser employed in the setup was locked to a cavity resonance using the Pound-Drever-Hall technique, which lead to an increased rate of measurements of up to 9 kHz. As compared to other spectroscopic techniques, CRD-FRS is particularly suited for measurements in frequency locked mode because the loss of spectral information is compensated by the increased selectivity of Faraday-rotation spectroscopy. Furthermore, measurements using CRD-FRS are independent from background signals that are not associated with the sample (e.g. varying laser power, losses of the empty cavity), which makes off-resonance measurements unnecessary and allows keeping the wavelength fixed at the transition frequency of the analyte.

In writing this thesis as a monograph, it was my intention to include and discuss additional thoughts and results that are often incompatible with the compact presentation in scientific publications. Abstracts of publications I authored and co-authored in the course of this thesis are enclosed in an appendix to this document.

Acknowledgements

Looking back at the past three years and eight months, I feel great joy and gratitude that I did not walk the path towards this thesis alone but was accompanied by a fine selection of inspiring and loving people.

I want to thank my supervisor Bernhard Lendl, who has been a consistent supporter of my academic development since 2014, for creating and providing the working environment that allowed me to pursue my scientific ideas and interests. Also, I am grateful for his support of my attendance of numerous international conferences and other science related trips.

I also very much thank Gerard Wysocki for the inspiring time I could spend in his laboratory, as well as Jonas Westberg and Link Patrick for their great support during that time and beyond.

I thank my present and former colleagues at the Lendl-group for good times spent together on many occasions and for sharing their experienced and thoughtful opinions on numerous problems.

I want to thank my family, in particular my father, Franz Hayden, for the unconditional support and love I experienced throughout my life and my studies.

I want to express my utmost gratitude to my loving partner, Bettina Baumgartner, who has been such a close companion throughout these years, both in a personal and professional sense. I am grateful for the uncounted scientific discussions we had and your help and input in so many aspects of this work. Most importantly, however, thank you for your love and patience.

Finally, financial support that enabled my full-time dedication to this thesis should not go unmentioned. I sincerely thank the taxpayers and the republic of Austria for having financed my education. The research for this thesis was funded via the Competence Centre ASSIC - Austrian Smart Systems Integration Research Center, co-funded by the Federal Ministries of Transport, Innovation and Technology (bmvit) and Science, Research and Economy (bmwfw) and the Federal Provinces of Carinthia and Styria within the COMET – “Competence Centers for Excellent Technologies” Programme.

Table of content

Abbreviations

	Explanation	See section
2*f*-WM(S)	Wavelength Modulation (Spectroscopy) with Second Harmonic Detection	(1.3)
AOM	Acousto-Optic Modulator	(2.6)
APD	Avalanche Photo-Diode	(6.1)
BW	Band width	(1.5)
BW	Brewster Window	(2.2.2)
c.c.	Complex Conjugate (also denoted by superscript *)	(1.4)
CES	Cavity Enhanced Spectroscopy	(2)
CRD(S)	Cavity Ring-Down (Spectroscopy)	(2.6)
CRD-FRS	Cavity Ring-Down Faraday Rotation Spectroscopy	(4.3)
CW	Continuous Wave	(2.6)
DBR	Distributed Bragg-Reflector	(6.1)
DFB	Distributed Feedback	(2.5)
DL	Diode Laser	(1.3)
EC(-DL)	External Cavity (Diode Laser)	(2.4), (6.1)
EOM	Electro Optic Modulator	(1.4), (6.1)
FI	Faraday Isolator	(6.1)
FM(S)	Frequency Modulation (Spectroscopy)	(2.4), (6.1)
FP	Fabry-Pérot	(2.1)
FRS	Faraday Rotation Spectroscopy	(4)
FSR	Free Spectral Range	(2.1.2)
FWHM	Full Width at Half Maximum	(2.1.2)
I-QEPAS	Intracavity QEPAS	(5)
IR	Infrared	(1.2)
LED	Light Emitting Diode	(3.3)
LHCP	Left Hand Circularly Polarized	(4.1)
ln	natural logarithm	(5.3.4)
LP	Linear Polarization	(4.1)
MCB	Magnetic Circular Birefringence	(4.1)
MCD	Magnetic Circular Dichroism	(4.1)
MCT	Mercury-Cadmium-Telluride (detector)	(5.1.1)
MFC	Mass Flow Controller	(5.1.1)

NEA	Noise Equivalent Absorption Coefficient	(1.5)
NEC	Noise Equivalent Concentration	(1.5)
NIR	Near Infrared	(1.2)
NNEA	Power Normalized Noise Equivalent Absorption Coefficient	(3.4.2)
OA-ICOS	Off-Axis Integrated Cavity Output Spectroscopy	Overview
OF	Optical Feedback	(2.5)
OF-CEAS	Optical Feedback Cavity Enhanced Absorption Spectroscopy	(5.3.6)
PAS	Photoacoustic Spectroscopy	(3)
PD	Photodetector	(4.3)
PDH	Pound-Drever-Hall	(2.4)
PI(D)	Proportional-Integral-(Differential)	(5.3.2), (6.1)
ppm	parts per million	Overview
ppb	parts per billion	Overview
ppt	parts per trillion	Overview
QCL	Quantum Cascade Laser	(2.4.1)
QEPAS	Quartz-Enhanced Photoacoustic Spectroscopy	(3.3)
QTF	Quartz Tuning Fork	(3.3)
RHCP	Right Hand Circularly Polarized	(4.1)
R-T	Rotational - Translational (energy transfer)	(3.1.2)
SNR	Signal to Noise Ratio	(1.5)
SSH	Schwartz-Slawsky-Herzfeld	(3.1.2)
TLAS	Tunable Laser Absorption Spectroscopy	(1.3)
UV	Ultra Violet	(3.3)
V-T	Vibrational - Translational (energy transfer)	(3.1.2)
V-V	Vibrationa - Vibrational (energy transfer)	(3.1.2)

Symbols

Symbol	Explanation	See section
A	Absorption	(1.1)
$A_{i,j}$	Einstein A - Coefficient	(3.1.1)
B	Magnetic Field Strength	(4.1)
B_{ij}	Einstein B - Coefficient	(3.1.1)
c	Vacuum Speed of Light	(1.2)
c_{ac}	Speed of sound	(3.1.3)
c_p	Specific Heat Capacity at Constant Pressure	(3.1.3)
c_V	Specific Heat Capacity at Constant Volume	(3.1.3)
d	Distance	(2.5)
$D_{A\text{-}B}$	Collision Cross Section	(3.1.2)
D_{cr}	Cross Section Area	(3.1.3)
E	Electric field amplitude	(1.1)
$\mathcal{E}$	Energy	(5.2.1)
F	Cavity Finesse	(2.1.2)
f	Frequency (general, *e.g.* of modulation)	(2.4)
F_N	Normalized Overlap Integral	(3.1.3)
g	Statistical Weight (Degeneracy)	(3.1.1)
G	Gauss (unit)	(4.1)
G	Total Internal Partition Sum	(5.2.1)
g_m	g-factor (Magnetism)	(4.1)
h	Planck's Constant	(1.2)
H	Heat	(3.1.2)
$\mathfrak{H}$	Linear Spectral Transfer Function (of a cavity)	(2.4)
I	Intensity	(1.1)
I_{sat}	Saturation Intensity	(5.3.4)
Im	Imaginary Part (of an expression)	(2.4)
J	Total Angular Momentum Quantum Number	(1.2), (3.1.1), (4.1)
j	Laser Current	(1.3)
J_B	Bessel Function of First Kind	(2.4)
k	Boltzmann Constant	(3.1.2)

k_{cell}	Cell Constant	(3.1.3)
L	Length, Optical Pathlength	(1.1)
ℓ	Combined Half-Round-Trip Losses	(5.3.2)
L_{cav}	Cavity Length	(2.1.1)
M	Magnetic quantum number	(4.1)
n	Refractive Index	(1.1)
N	(molecular) number density	(1.1)
P	Optical Power	(2.2)
p	Pressure	
Q	Quality factor	(3.1.3)
R	Ideal Gas Constant	(1.1)
R	Reflectivity	(2.1.1)
r_m	reflection coefficient	(2.4)
Re	Real Part (of an expression)	(2.4)
S	Line Strength	(1.2)
T	Temperature	(1.1)
t	Time	(1.3)
T	Transmission	(2.1.1)
t_m	Transmission coefficient	(2.4)
w	$1/e^2$ beam radius	(2.1.1)
w_0	$1/e^2$ beam waist radius	(2.1.1)
x	Volume fraction, concentration	(1.1)
$\mathbf{x}$	Spatial coordinates	(3.1.3)
Y	Signal (*e.g.* Voltage from detector, QEPAS signal)	(1.5), (5.3.4)
z	Spatial Coordinate in Direction of Beam Propagation	(2.1.1)
Z	Collision Frequency per Molecule	(3.1.2)
z_0	Confocal Parameter	(2.1.1)
z_{center}	Beam Waist Position	(2.1.1)
$\hat{Z}$	Collision Number	(3.1.2)
α	Absorption Coefficient	(1.1)
α_H	Henry factor	(2.5)
β	Angle (general)	(2.2.2)
β_B	Brewster's angle	(2.2.2)
Γ	Line Shape Function	(1.2)

$\bar{\Gamma}$	Peak Normalized Line-Shape Function	(5.3.4)
γ	Specific Heat Capacity Ratio	(3.1.3)
$\gamma^{\uparrow}$	Rate of (coherent) Excitation	(3.1.1)
$\gamma^{\parallel}$	Rate of (collisional) Energy Transfer / Relaxation	(3.1.2)
η	Stability Parameter	(2.1.1)
Θ	Round-Trip Rotation Angle	(4.3)
κ	(Optical) Feedback Rate	(2.5)
λ	Wavelength	(1.1)
μ	Reduced Mass	(3.1.2)
μ_B	Bohr's magneton	(4.1)
ν	Frequency	(1.4)
$\tilde{\nu}$	Wavenumber / Spatial Frequency	(1.1)
ζ	Modulation Depth of Phase modulation	(2.4)
ρ	Radius of Curvature	(2.1.1)
σ	Standard Deviation	(1.5)
τ	Ring-Down Time	(2.6)
τ_0	Empty-Cavity Ring-Down Time	(2.6)
ϕ	Phase (of light)	(1.4)
φ	Angle (Orientation) of Linear Polarization	(4.2)
ω	Angular Frequency	(3.1.3)

Overview

The term "trace gas" is commonly used for constituents of a gas, typically air, accounting for less than approximately one per mill volume fraction. Although being minor constituents, trace gases can have a major impact on chemical processes. Amongst the best known examples for the importance of trace gases are ozone and ozone depleting substances. Ozone present in the stratosphere at concentrations of a few ppm (parts per million, 10^{-6}) protects against UV radiation, but is considered hazardous to humans at concentrations of ~ 100 ppb (parts per billion, 10^{-9}). The concentration of ozone in the atmosphere is influenced by molecular species, such as the infamous chlorofluorocarbons (CFCs) as well as naturally occurring species such as the OH and HO_2 radicals, whose concentrations fall in the ppb- and ppt-range (parts per trillion, 10^{-12}) or even below [1]. Besides in atmospheric chemistry and environmental monitoring, trace gases are important in a variety of disciplines ranging from medicine (breath analysis [2], isotope breath tests [3]) over semiconductor and chemical industry (need for high purity gases, monitoring of catalyst poisoning substances, *etc.*) to emission monitoring and fundamental sciences (*e.g.* trace radical species for the study of reaction mechanisms and kinetics [4,5]), to name a few.

With the importance of trace gases in such diverse areas comes the need for measuring their concentrations. Numerous technologies, such as electrochemical sensors, mass spectrometry, gas chromatography, chemi-luminescence, non-dispersive absorption, and others are available for this task, each with its unique benefits and drawbacks. Amongst these technologies, optical spectroscopy stands out for its selectivity (low cross sensitivities), minimum sample treatment without consumption of chemicals or reference gases, very low response times (suitable for real time and online measurements) and the traceability of measurements to absolute physical parameters of the sample, avoiding frequent re-calibration or even enabling quantification without any calibration [6]. Optical spectroscopy, in particular infrared absorption

spectroscopy, has found widespread use in the above-mentioned fields for these reasons. The range of applications and possibilities of optical spectroscopy has been widened dramatically in the past ~ two decades through the introduction and commercialization of cavity enhanced spectroscopy, mostly cavity ring-down spectroscopy (CRDS) and off-axis integrated cavity output spectroscopy (OA-ICOS) [7,8]. Utilizing highly reflective mirrors forming a resonator for light, *i.e.* an optical cavity, these techniques vastly increase the pathlength over which light interacts with the sample and, accordingly, the sensitivity of measurements. Although CRDS and OA-ICOS are quite different from an experimental point of view, both are based on measuring the absorption by the sample by detecting the intensity of light transmitted through it. In other words, both fall in the category of direct absorption spectroscopy and hence obey a similar set of trading rules. The enhanced sensitivity brought about by the optical cavity ("cavity enhancement") can, however, also be utilized for other types of spectroscopy.

It is the aim of this thesis to investigate two of these alternative, cavity enhanced spectroscopic approaches for trace gas sensing, namely photoacoustic spectroscopy (PAS) with a focus on quartz-enhanced PAS (QEPAS), and Faraday rotation spectroscopy (FRS). Chapter 1 gives an introduction to the fundamentals of (laser-) spectroscopic gas sensing and discusses state-of-the art direct absorption as well as dispersion spectroscopy. Chapter 1 lays the foundation for the following introductions to PAS, QEPAS and FRS given in chapters 3 and 4 as well as the discussion on their distinct features for the analysis of trace gases. Chapters 3 and 4 also include the state of the art in combining cavity enhancement with PAS and FRS, respectively. Theoretical and practical aspects of high finesse optical cavities and their use in cavity enhanced spectroscopy are provided in chapter 2. While the first four chapters have introductory character, chapters 5-7 present original results obtained during the work on this thesis over the past three years and eight months. Photoacoustic measurements are presented in chapter 5. Mid-infrared QEPAS measurements of CO without cavity enhancement are presented that reveal a peculiar scaling of QEPAS signals with humidity. The observed behavior is explained quantitatively based on a kinetic model for the energy transfer from ro-vibrationally excited CO to N_2 and H_2O and is replicated in simulations. An experimental setup for cavity enhanced QEPAS based on a Brewster window cavity and optical feedback locking is introduced and described in detail. The achieved cavity enhancement of intracavity power is quantified and strong optical saturation of CO is observed. The effects of saturation are described quantitatively and cavity enhanced QEPAS sensing of CO is demonstrated in the strongly saturated regime. Chapter 6 presents advances in cavity ring-down FRS (CRD-FRS), a recently developed technique for cavity enhanced FRS. Here, measurements in line-locked

operation are presented, together with strongly increased repetition rates of CRD-FRS measurements enabled by actively locking the laser frequency to a cavity resonance. The unique properties of CRD-FRS, together with the stabilization of the wavelength to the center of an absorption line of O_2, allowed retrieving concentrations of O_2 independent from any off-resonance background measurement. The final chapter 7 gives an outlook on future developments and potential improvements based on the results in the previous chapters. Abstracts of publications I authored and co-authored in the past three years are given in an Appendix.

Parts of the work presented in this thesis were published in refs. [9–11].

1. Introduction to Gas-phase Spectroscopic Sensing

To detect and quantify trace gases using optical spectroscopy, the effects of interaction between light and the targeted molecule are measured. Generally, these effects can be observed macroscopically by either detecting changes in the state of light or the gas. Because most of the detectable changes in the gas are the result of a relatively complex series of elementary steps, spectroscopic techniques following the latter approach are referred to as "indirect" techniques, while approaches based on measuring the properties of light are called "direct". To date, the vast majority of direct and indirect techniques for spectroscopic gas sensing is based on absorption measurements. Section 1.1 will briefly introduce the fundamentals of absorption as well as dispersion, the second important measurement principle for spectroscopic gas sensing, as well as their relation to molecular concentration of a trace gas. The infrared spectra of molecular gases, whose rich structure facilitate their identification and selective quantification, are discussed in section 1.2. The following sections 1.3 and 1.4 give an introduction to the principles and instrumental realization of direct absorption and dispersion spectroscopic trace gas sensing. The chapter is concluded in section 1.5 by introducing parameters frequently used to compare spectroscopic gas analyzers against each other and to quantify their performance.

1.1. Absorption and Dispersion, Lambert-Beer's Law

As light passes through a volume filled with a homogeneous sample of any aggregate state, its amplitude and phase as compared to a passage through the empty (evacuated) volume will change. The complex electric field amplitude E after passing the filled volume can be described as

$$E = E_0 \exp\left(-\frac{\alpha}{2}L\right)\exp(i2\pi(n-1)L\tilde{\nu}). \tag{1.1}$$

Herein, E_0 refers to E one would measure for the empty volume, L is the distance travelled through the volume (optical pathlength), $\tilde{\nu}$ is the vacuum wavenumber, also referred to as (spatial) frequency in this thesis (inverse of vacuum wavelength λ), and α and n are sample- and wavelength specific quantities, referred to as absorption coefficient and refractive index, respectively, that describe the response of the sample. Generally, for a given wavelength and sample, both α and n are not given by single real values. On the one hand, it must be taken into account that the electric field is a vector whose orientation defines the polarization of light. Generally, the response of the sample will depend on the orientation between the molecules and the electric field, and α and n are consequently not the same for the components of the electric field amplitude. Since gases are isotropic, the sample response is the same for orthogonal linear polarization states [12]. However, even in isotropic samples, orthogonal circular polarization states may experience different values of α and n if the sample is chiral or subjected to a static magnetic field (compare chapter 4). On the other hand, the response of the sample in general depends on the strength of the electromagnetic field, *i.e.* α and n are influenced by the intensity of light and must be expanded in powers of E. Only if the electric field E of light is weak compared to the fields present within the molecules, the molecular response described by α and n can be considered independent from the intensity of light. This is the regime of linear optics and linear spectroscopy, in which almost all spectroscopic trace gas sensors operate. Although state-of-the art spectroscopic gas sensing is mostly linear and performed on achiral molecules, the polarization- and intensity dependence of α and n will prove important in the context of this work.

Independent whether measurements are performed in a linear or non-linear regime on chiral or achiral molecules, all trace gas applications are based on the fact that α and n of a gas are proportional to the number of molecules per unit volume, *i.e.* number density N. For trace gases, the sample typically consists of a few major constituents (N_2, O_2, Ar, H_2O, CO_2) summarized as the sample matrix and the targeted analyte species. The number density N_A of the analyte in an ideal gas in mol/m^3 is directly proportional to its volume fraction x_A, *i.e.* its concentration x_A.

$$N_A = \frac{p_A}{RT} = x_A \frac{p}{RT} \tag{1.2}$$

Herein, p_A is the partial pressure of the analyte, p is the overall sample pressure, R is the ideal gas constant and T is absolute temperature. The absorption coefficient and refractive index of the gas can be simply expressed as the linear sum of the contributions from all molecular species i present in the gas

$$\begin{aligned} \alpha &= x_A \alpha_A + \sum x_i \alpha_i \\ n &= x_A n_A + \sum x_i n_i \end{aligned} \tag{1.3}$$

Herein, α_i and n_i are the absorption coefficient and refractive index of the pure substance i at a given p and T (compare section 1.2). If the wavelength of a measurement is chosen such that the absorption coefficient α_A of the analyte is much bigger than that of the matrix, changes of x_i due to displacement of the matrix by the analyte can be neglected and the summing term in equation (1.3) is constant for small changes of x_A. Hence, inserting in equation (1.1) yields

$$E = E_0 \exp\left(-(x_A\alpha_A + \sum x_i\alpha_i)\frac{L}{2}\right)\exp(i2\pi(x_A n_A + \sum x_i n_i - 1)L\tilde{\nu}) = E_{0,M}\exp\left(-x_A\alpha_A\frac{L}{2}\right)\exp(i2\pi x_A n_A L\tilde{\nu}). \tag{1.4}$$

Herein, $E_{0,M}$ was defined as the electric field amplitude measured for the pure matrix ($x_A = 0$). Both, the absorption coefficient and phase scale linearly with x_A. When turning from E to the intensity $I \sim |E|^2$, Lambert-Beer's law connecting a measurement of absorbance A to the concentration x_A is derived from equation (1.4)

$$A := \ln\left(\frac{I_0}{I}\right) = x_A\alpha_A L. \tag{1.5}$$

Note that absorbance is commonly defined in the chemical sciences using the logarithm to base 10, rather than the natural (napierian) logarithm used in this work.

1.2. Infrared Spectra of Molecular Gases

Up to this point, α and n were introduced in a phenomenological way without specifying their physical origin. To discuss the origin and spectral properties of α and n, the discussion is limited to the infrared (IR) spectral range due its outstanding relevance for trace gas sensing. The mid-IR and near-IR spectral ranges are typically defined as $400\,\mathrm{cm}^{-1} < \tilde{\nu} < 4000\,\mathrm{cm}^{-1}$ and $4000\,\mathrm{cm}^{-1} < \tilde{\nu} < 13333\,\mathrm{cm}^{-1}$, respectively. The photon energy $h\tilde{\nu}c$ (h: Planck's constant, c: speed of light) in the mid-IR coincides with fundamental vibrational transitions of most molecules, while the near-IR is mostly home to overtones of vibrational transitions. Although the number of vibrational modes ($3 \cdot N_{atoms} - 6$; $3 \cdot N_{atoms} - 5$ for linear molecules) is small for most gas molecules due to the low number of atoms N_{atoms}, each mode couples in the infrared spectrum to rotational transitions. Depending on the symmetry (the "top") of the molecule, this gives rise to a large number of ro-vibrational absorption lines for each vibrational transition [13]. Further, since the energy gaps between rotational states are small, higher lying rotational states are thermally populated to a significant extent at ambient conditions. Therefore, ro-vibrational transitions from different rotational ground-states can be observed, further increasing the number of lines associated with a given vibrational transition. This "forest" of lines can be categorized into three branches differing in the change of rotational quantum number J by -1 (P-branch), 0 (Q-branch) and +1 (R-branch). A more detailed discussion on ro-vibrational infrared spectra is omitted at this point and the interested reader is referred to extensive literature available on the topic [13,14].

Fortunately, for the experimentalist, mature and freely accessible databases exist that list calculated and experimental line positions and line strengths of most relevant molecules, as well as all further practically relevant parameters associated with an absorption line. As an example, Figure 1.1 shows absorption lines of H_2O and CO obtained from the HITRAN2016 database [15].

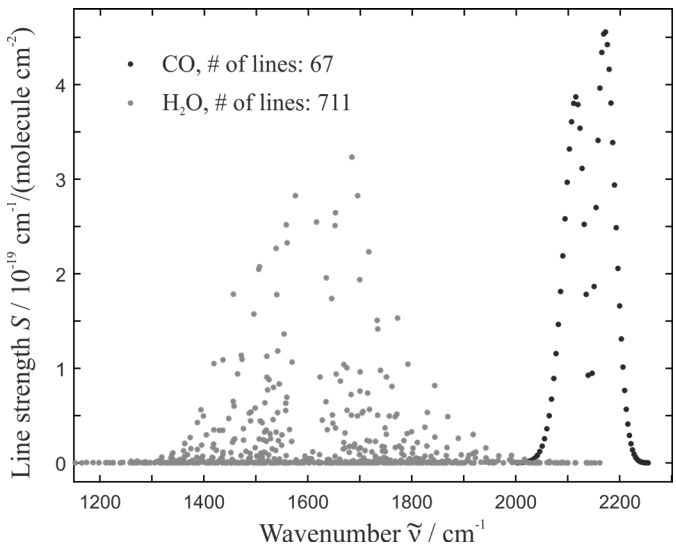

Figure 1.1. Absorption lines obtained from the HITRAN database for the most abundant isotopologues of H_2O and CO. The given numbers of lines refer to lines with line-strength S larger than 10^{-4} of the strongest line in the plotted range. The complete list obtained from HITRAN includes 7258 lines for H_2O and 224 lines for CO.

With a few exceptions, the 49 molecules (and 124 isotopologues) for which absorption lines are included in the HITRAN2016 database have less than six atoms. Besides their lower abundance associated with their decreasing vapor pressure, the reason for not including larger molecules is the vast number of lines as well as the decreasing rotational energy spacing (inversely proportional to the moment of inertia, compare section 5.2.1) of these molecules. Hence, under practically relevant conditions, the large number of strongly overlapping lines yield broad spectral features without the clear rotational fine-structure observed for small molecules. For larger molecules, the HITRAN2016 database therefore includes absorption cross sections, rather than individual absorption lines.

The extent to which individual absorption lines of a molecule overlap depends on their energy spacing and the width of the individual lines. The line-width is described by the so called line-shape function $\Gamma(\tilde{\nu} - \tilde{\nu}_0)$. Γ is an area normalized function that relates the spectral absorption coefficient associated with a particular line of a molecule A centered at $\tilde{\nu}_0$ to the line-strength S [16]

$$\alpha(\tilde{\nu}, T, p) = N_A S(T) \Gamma(\tilde{\nu} - \tilde{\nu}_0, T, p). \tag{1.6}$$

Herein, the number density N_A is given by equation (1.2). The line-strength varies with temperature T since it includes the temperature dependent population of the ro-vibrational ground-state (compare section 5.2.1). The width of the line-shape function Γ increases with temperature and pressure based on the two dominant underlying broadening mechanisms: collisional broadening and Doppler broadening. A considerable number of functions based on assumptions of varying complexity have been introduced for Γ, and dedicated conferences were held on the topic and the International Union of Pure and Applied Chemistry (IUPAC) installed a task group to define a recommended function for Γ that is now the so-called Hartmann-Tran profile [17]. Despite the recommendation for the Hartmann-Tran profile, the Voigt profile is still used in many cases, in particular in trace gas sensing. The Voigt profile is a convolution of a Gaussian profile that accounts for Doppler broadening and a Lorentzian profile describing collisional broadening. For the convenience of users, web-pages [18] as well as a programming interface for Python [19] exist for computing the spectral absorption coefficient of a molecule based on the parameters listed in the HITRAN2016 database.

It should be mentioned that the gas pressure not only influences the width of the line-shape function, but, to a small amount, also the line position $\tilde{\nu}_0$ (*e.g.* by $2.6 \cdot 10^{-3}$ cm^{-1} atm^{-1} for the R9 transition of CO at 2179.77 cm^{-1}).

1.3. Direct Absorption Spectroscopy

Today, the most mature and widely employed technique for laser spectroscopic trace gas sensing is tunable laser absorption spectroscopy (TLAS) [20]. The principles of TLAS are summarized in Figure 1.2 [20]. Light emitted by a tunable laser, *e.g.* a diode laser or quantum cascade laser, is transmitted through a gas cell and detected by a photodetector. Typically, multipass cells, such as the Herriot cell [21], are used to increase the optical pathlength through the gas. The sample gas is pumped through the gas cell using a membrane vacuum pump and the pressure is typically stabilized to a reduced pressure between 50 mbar and a few hundred mbar to reduce the width of absorption lines and decrease the overlap of the targeted line with interfering lines of the matrix. The laser current is ramped, which tunes the laser wavenumber $\tilde{\nu}$ across the desired spectral range. For every period of modulation, the laser is briefly switched off by swiftly decreasing the laser current j below the threshold j_{thr}. This is necessary to determine the zero-level of the detector signal, corresponding to 100 % absorption. The transmission signal from the detector is digitized, synchronized to the modulation signal and analyzed on a computer. The detector signal recorded while $\tilde{\nu}$ sweeps across an absorption line can be described as

$$I(t) = k_0 + k_1 \cdot (j(t) - j_{thr}) \cdot \exp\left(-\alpha\left(\tilde{\nu}(t)\right)L\right). \tag{1.7}$$

Herein, k_0 and k_1 are a detector offset and a proportionality factor, respectively, and L is the pathlength through the gas cell.

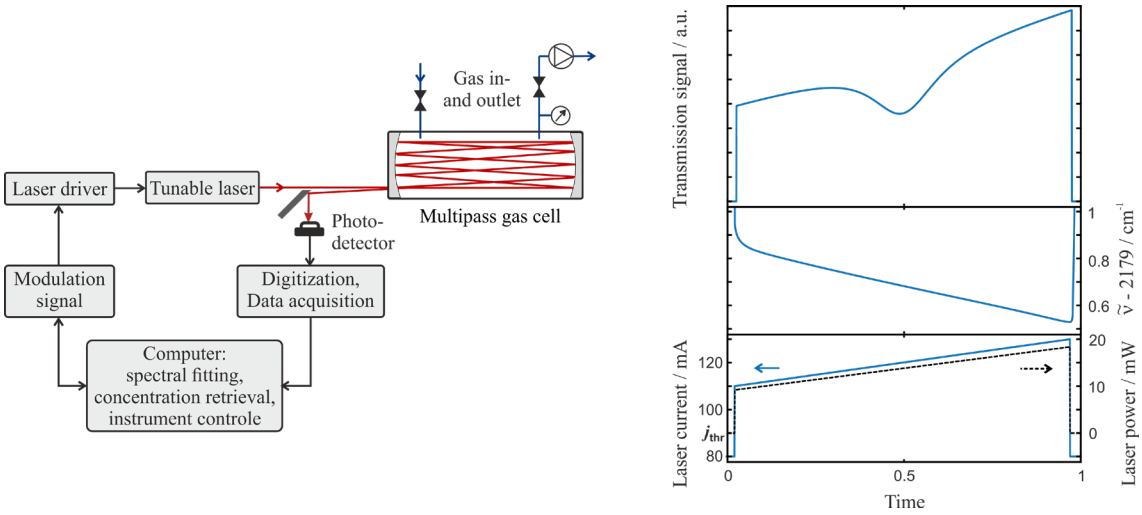

Figure 1.2. Left: Schematic of an experimental setup for tunable laser absorption spectroscopy. Right: Illustration of signals and laser parameters (wavenumber $\tilde{\nu}$ and emitted power) during a period of current modulation.

The wavenumber tuning $\tilde{\nu}(t)$ is typically described by a polynomial function whose coefficients are determined beforehand, *e.g.* using an etalon of known free spectral range [22]. The spectral absorption coefficient $\alpha(\tilde{\nu})$ is described by one or the sum of multiple absorption line profiles given by equation (1.6). Inserting (1.6) with a given line-shape function (typically a Voigt profile) in (1.7) allows retrieving the number density or concentration of the species corresponding to an absorption line by means of fitting of the recorded detector signal. An important advantage of TLAS is that the recorded signal can be directly traced back to the absorption coefficient of the sample and, with the line-strength from databases, to the molecular concentration. Therefore, concentrations can be retrieved without any calibration. A technical challenge of TLAS is that small changes of signal associated with sample absorption must be detected on a large background signal. This requires a large dynamic range of the detector and the digitizer, as well as a very high signal to noise ratio in the recording of the background (the baseline $(k_0 + k_1 \cdot (j(t) - j_{thr})$ in equation (1.7)). Fringes commonly spoil measurements and increase the noise floor far above the shot-noise level and above the detector- and laser intensity noise, especially for long averaging times. Nevertheless, with the necessary know-how and careful system design, fractional absorptions of $\sim 5 \cdot 10^{-6}$ or even below 10^{-6} can be achieved in 1 s integration time, translating to typical trace gas concentrations of tens of ppt for a pathlength on the order of 100 m [20].

Another technique of direct absorption spectroscopy closely related to TLAS, 2*f* - wavelength modulation spectroscopy (2*f*–WMS), shall be briefly mentioned [14,23]. Here, the optical setup is identical to TLAS, but the laser wavenumber is modulated sinusoidally around the targeted absorption line at a few kHz. After demodulation of the accordingly modulated transmission signal at the second harmonic (hence 2*f*) of the modulation

frequency by a lock-in amplifier, a signal is obtained that is directly proportional (for small absorptions) to the molecular concentration. The advantages and challenges of 2*f*-WMS are very similar to those of TLAS, but 2*f*–WMS is particularly simple to implement since no fitting procedure is required. However, the direct traceability of signals to molecular concentrations is somewhat lost, which is why 2*f*-WMS instruments typically require calibration to quantify trace gases.

1.4. Dispersion Spectroscopy

In recent years, increasing efforts were taken to develop novel dispersion spectroscopic techniques, both for liquid phase [24] and trace gas sensing, to complement established absorption based schemes. Dispersion spectroscopy measures the spectral refractive index $n(\tilde{\nu})$ of a sample, rather than $\alpha(\tilde{\nu})$ based on a measurement of the phase of light. The phase ϕ picked up by light upon transmission through a gas cell of length L is given by (compare equation (1.1))

$$\phi = 2\pi n L \tilde{\nu}. \tag{1.8}$$

The dispersion and absorption spectrum of an isolated line of CO is shown in Figure 1.3. The dispersion profile associated with an absorption line can be calculated from the absorption spectrum based on Kramers-Kronig transformation [25]. For a Voigt-shaped absorption line, an analytic expression for the refractive index spectrum exists based on the Faddeeva function [26]. For an isolated Lorentzian – and Gaussian absorption profile of unity peak absorbance (base 10), the peak-to-trough variation of ϕ around a molecular resonance is independent from the width of the profile and given by 66.0° and 80.5°, respectively. Like absorption, the dispersion of a line is directly proportional to the number density and concentration of the absorbing molecule.

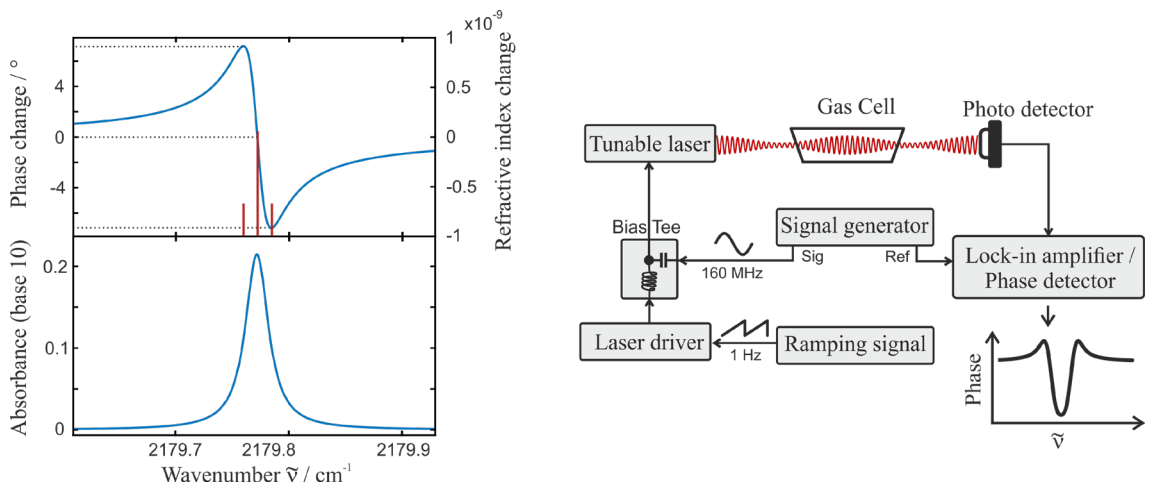

Figure 1.3. Left: Absorption and dispersion profile of an absorption line of CO. The red vertical lines illustrate the three spectral components of amplitude modulated light experiencing different refractive indices. The refractive index was calculated based on a pathlength of 100 m. Right: Schematic of a setup for heterodyne dispersion spectroscopy with a directly modulated laser.

Since the phase of light cannot be detected directly by a photodetector, it must be measured by observing the interference with light whose phase is considered as the reference. This is typically done by splitting a beam into a sample-beam that is transmitted through a sample and a reference beam that is not sent through the sample and recombining the two at a detector (*e.g.* in Michelson or Mach-Zehnder geometry [24,27]). Here, both beams share a common wavenumber $\tilde{\nu}$, so the phase of light is detected in a homodyne fashion. More recent developments for trace gas sensing focus on heterodyne techniques. Here, the sample-beam is overlapped with a reference beam whose frequency is shifted by an amount $\Delta\nu$. This results in a beating of the intensity at a frequency $\Delta\nu$ at the detector whose phase is proportional to the difference between the refractive indices n_{sample} and n_{ref} experienced by the sample- and reference beam. Assuming equal pathlength L for both beams, the intensity is given by

$$\begin{aligned} I &= \left(E_{ref} + E_{sample}\right) \cdot c.c. \\ &= \left[E_{0,ref} \exp\left(i2\pi\left[(\tilde{\nu}c + \Delta\nu)t + n_{ref}\left(\tilde{\nu} + \frac{\Delta\nu}{c}\right)L\right]\right)\right. \\ &\left. + E_{0,sample} \exp(-\alpha(\tilde{\nu})L/2) \exp\left(i2\pi\left[\tilde{\nu}ct + n_{sample}\tilde{\nu}L\right]\right)\right] \cdot c.c. \end{aligned} \tag{1.9}$$

Herein, c.c. denotes the complex conjugate of the expression in brackets. With $I_{0,ref} := E_{0,ref}E^*_{o,ref}$ and $I_{0,sample} := E_{0,sample}E^*_{o,sample}$, this simplifies to

$$\begin{aligned} I &= I_{0,ref} + I_{0,sample} \exp(-\alpha(\tilde{\nu})L) \\ &+ 2\sqrt{I_{0,ref}I_{0,sample}} \exp(-\alpha(\tilde{\nu})L/2) \cos\left(2\pi\left[\Delta\nu t + \frac{\Delta\nu}{c} n_{ref}L\right.\right. \\ &\left.\left. + \tilde{\nu}L\left(n_{ref} - n_{sample}\right)\right]\right) \end{aligned} \tag{1.10}$$

The third summand in equation (1.10) oscillates in time at the difference frequency $\Delta\nu$. Of the two terms in the cosine describing the phase of the oscillation (those independent from t), the first one, proportional to $\Delta\nu$, is a constant offset, while the second one follows the refractive index profile $n_{sample}(\tilde{\nu})$ of the sample (compare Figure 1.3). Hence, by analyzing the phase of the oscillating detector signal, the refractive index of the sample, as compared to the reference, can be retrieved.

Intriguingly, the dispersion profile can even be retrieved if both, the reference and sample beam, are transmitted through the sample without spatially separating the two beams. This is achieved by choosing the frequency difference $\Delta\nu$ comparable to the width of the anomalous dispersion profile (typically tens to a few hundred MHz). In this case, the spectral components of the single beam are sufficiently detuned in frequency to experience significantly different refractive indices in the vicinity of the molecular resonance (spectral components illustrated in Figure 1.3 as three vertical red lines in the dispersion spectrum). The recorded phase spectrum then follows the spectral difference $n_{sample}(\tilde{\nu})$ - $n_{sample}\left(\tilde{\nu} \pm \frac{\Delta\nu}{c}\right)$,

rather than the difference $n_{ref} - n_{sample}$ between two gases. This configuration has the important advantage that both "beams" (spectral components) share a common optical path and experience identical non-sample related phase changes, *e.g.* due to vibrations or thermal drifts, which circumvents the need for vibration isolation typical for interferometric measurements.

To generate two phase coherent beams of different frequency, an acousto-optic modulator was used in the pioneering work by Wysocki and Weidmann [28]. Alternatively, electro-optic modulators as well as direct current modulation can be employed. Both these techniques yield intensity modulation of the laser output at a moderate amplitude, in which case the laser spectrum is composed of three lines of significant amplitude lying at the center wavenumber $\tilde{\nu}_0$ and wavenumbers $\tilde{\nu}_0 \pm \nu/c$ shifted to lower and higher wavenumbers by the modulation frequency ν (compare Figure 1.3, see also section 2.4). At the detector, the beating between the center wavenumber and the wavenumber components shifted to higher and lower wavenumber oscillate at the modulation frequency, and the vector sum of both oscillations yield the detected phase [29].

A schematic setup for heterodyne (phase sensitive) dispersion spectroscopy (HPSDS [30]) is shown in Figure 1.3. A laser is directly modulated and the intensity modulated light is detected by a fast photodetector. The phase of the modulation is retrieved by means of lock-in detection. The phase spectrum recorded by slowly scanning the laser center wavenumber across the absorption line resembles the group index of the sample [31]. In a very similar configuration, coined "chirped laser dispersion spectroscopy" (CLaDS), the laser center wavenumber is swiftly chirped, rather than slowly ramped, which causes an accordingly rapid variation of the phase. This rapid change in phase is detected as a small change in modulation frequency via a spectrum analyzer [28,32]. HPSDS as well as CLaDS performed under direct current modulation requires taking into account the effects of simultaneous intensity- and frequency modulation, a discussion of which can be found in [26,29,32,33].

The motivation for using dispersion spectroscopy for trace gas sensing comes from the different trading rules that apply to dispersion spectroscopy measuring phase as compared to those of absorption spectroscopy measuring optical power [31,34]. Most notably, dispersion measurements are widely immune to fluctuations in optical power reaching the detector, which is particularly interesting for remote sensing based on back-reflection from a diffusely reflecting target [35,36]. While the transmission, as recorded by TLAS and 2*f*-WMS, scales linearly with concentration only within the approximation $\mathrm{e}^{-x} \approx 1 - x$ valid for small concentrations, the recorded phase scales linearly with molecular concentration, even for high optical densities, yielding a large dynamic range of measurements [37]. Despite dispersion spectroscopic trace gas sensing still being a relatively young field, an open-path

trace gas analyzer based on heterodyne dispersion spectroscopy is now commercially available [38].

1.5. Performance Characteristics of Spectroscopic Gas Analyzers

To characterize trace gas analyzers and compare them against each other, a variety of parameters and properties of the instruments must be considered. In scientific publications on spectroscopic trace gas analysis, the biggest attention is often drawn to the limits of detection (LOD) achieved with the introduced apparatus. What may be considered a simple single value corresponding to the smallest concentration that could be detected in an experiment is actually significantly more complex. A variety of quantities, the most important of which will be introduced in the following, is frequently quoted to characterize detection limits, and an even larger variety of approaches to determine those quantities exist. In analytical chemistry, the LOD and limit of quantification (LOQ) are defined in norms [39] and are often approximated as three times (LOD) and nine times (LOQ) the standard deviation σ_x of repeated measurements of the concentration x of a blank sample [40]. In manuscripts on spectroscopic trace gas sensing, the noise equivalent concentration (NEC) and other noise equivalent parameters are quoted more frequently than LOD. The NEC in units of volume fraction per $\mathrm{Hz}^{-1/2}$, is defined as the concentration x would give a signal Y that equals the noise floor, *i.e.* the standard deviation σ_Y of the signal, in a measurement of a blank sample, normalized by the square root of the measurement bandwidth (~ inverse integration or averaging time).

$$NEC = \frac{\sigma_Y}{\frac{dY}{dx} \cdot \sqrt{bandwidth}}. \tag{1.11}$$

The normalization to the square root of the bandwidth is chosen because the signal to noise ratio (SNR) generally increases with the square root of the averaging time or number of samples. In order to compare measurements on absorption lines of different line strength S and with different optical pathlength L, the noise equivalent absorption coefficient (NEA) is often used as a quantity to describe the performance of absorption based gas analyzers.

$$NEA = \frac{\sigma_Y}{\frac{dY}{dA} \cdot L \cdot \sqrt{bandwidth}}. \tag{1.12}$$

The NEA allows estimating the NEC and LOD ($\approx 3 \cdot$ NEC) that would be obtained if the same system was transferred to another application, *i.e.* to another molecular gas and absorption line or a longer/shorter gas cell of given length L. Analogous to the definition of NEA, a noise equivalent phase or refractive index can be defined for dispersion spectroscopy, or a noise equivalent polarization rotation angle for Faraday rotation spectroscopy (compare chapter 4). In any case, quoting any of these values should always be accompanied by a clear description of how the noise floor σ_Y was measured. Although the measurement of σ_Y should resemble the procedure for an actual measurement of gas

concentration, it is not uncommon to find values for σ_Y derived from distinctly different measurements.

Another interesting consideration is the role of the bandwidth, *i.e.* signal averaging, for the obtained figures of merit. For short averaging times, the SNR typically increases with the square root of the averaging time. However, this trend is in practice limited to short averaging times due to various slow drifts, *e.g.* of the spectral position of optical fringes. The detection limits for varying integration time are typically investigated following the procedure proposed by Peter Werle *et al.* by means of Allan variance analysis [41]. The obtained Allan deviation is typically plotted in a log-log plot against the averaging time ("Allan-Werle plot", compare Figure 6.8).

Besides the limits of detection, many other parameters are relevant to assess the applicability of a spectroscopic trace gas analyzer for a given problem. The (linear) dynamic range is defined as the ratio of largest and smallest concentration that can be quantified, where the largest concentration is often defined as the upper limit of linear instrument response [42]. A large dynamic range is not only needed for measurements of strongly varying concentrations, but is also a prerequisite for measurements of high precision. Assuming the noise floor remains constant with increasing concentration, the relative accuracy, defined as the standard deviation of consecutive concentration measurements over their mean value, for the largest concentration would equal the inverse dynamic range. In practice, however, the noise floor typically increases towards higher concentrations. The accuracy of a measurement, defined as the deviation of the measured average concentration from the true concentration, depends critically on accurate calibration as well as the stability of the calibration over time. Hence, the necessary interval between calibration and re-calibration is another practically relevant parameter for trace gas sensing.

Although infrared spectroscopy features very high selectivity, different techniques of spectroscopic trace gas sensing vary strongly in their sensitivity to the concentration of other gas constituents (matrix composition). The robustness of calibrations against changes in matrix composition is particularly important for indirect spectroscopic techniques, such as photoacoustic spectroscopy (compare section 3.1.2 and 5.2). Further important practical aspects include the size, weight and power consumption of an instrument, that determine, together with its overall mechanical robustness, its portability, *e.g.* on airplanes, cars, humans and drones. For measurements of rapidly varying concentrations, *e.g.* in the exhaust of a combustion engine, the readout frequency of concentration measurements is of importance. Most spectroscopic systems for trace gas sensing are inherently fast (typically in the kHz range), but practically limited by either the integration time necessary to achieve a sufficient SNR or by the rate at which the sample gas is exchanged in the gas cell. Gas cells of small volume are hence desirable for fast gas exchange, but also for measurements on limited sample volumes.

2. Cavity Enhanced Spectroscopy

The term "Cavity enhanced spectroscopy" (CES) encompasses a variety of spectroscopic techniques that exploit the properties of high finesse optical cavities for measurements with increased sensitivity and/or precision [43]. Optical cavities are resonators for light that have been studied extensively over decades, mostly in the context of lasers [44]. It was, however, not before the 1980s when optical cavities were used initially for determining mirror losses [45,46] and later for cavity ring-down spectroscopy (CRDS) [47]. Today, commercial instruments based on CRDS and off-axis integrated cavity output spectroscopy (OA-ICOS) are available and applied mostly to atmospheric gas sensing. Besides CRDS and OA-ICOS, numerous other techniques that exploit the unique properties of optical cavities for highly sensitive spectroscopic measurements have been investigated [48].

Prior to discussing two of these techniques, namely intracavity photoacoustic spectroscopy and cavity ring-down Faraday rotation spectroscopy, this chapter gives an introduction to the properties of optical cavities and how they can be exploited for spectroscopic gas sensing. The first section of this chapter introduces the relevant properties of high finesse cavities that make them attractive for spectroscopy. The gain in sensitivity arises from the increase of optical pathlength or optical power inside the cavity, which will be derived in section 2.2. The following sections discuss experimental aspects of working with high finesse cavities. A brief introduction to the coupling of light from a laser to a high finesse cavity is given in section 2.3. To achieve the high intracavity power levels desired for intracavity photoacoustic spectroscopy (section 5.3) as well as to increase the acquisition rate of cavity ring-downs in cavity ring-down Faraday rotation spectroscopy (chapter 6), the laser wavenumber must be stabilized to a cavity resonance. Sections 2.4 and 2.5 discuss two methods for realizing this stabilization. Due to its outstanding role in cavity enhanced spectroscopy and its use in sections 5.3 and 6, the final section of chapter 2 gives a brief introduction to cavity ring-down spectroscopy.

2.1. General Properties of High-Finesse Cavities

While a wide variety of optical cavity designs exists, the majority of CES is performed in Fabry-Pérot (FP) cavities. Although this chapter focuses mostly on FP cavities, the findings of this section hold, with minor corrections, for other cavities.

2.1.1. Spatial Modes

The FP cavity consists of two curved mirrors of reflectivity R and transmission T facing each other. Hence, the FP cavity is a kind of FP interferometer. In the context of CES and this work, the term cavity is used only for stable resonators, *i.e.* interferometers for which electromagnetic modes exist that, after one round-trip through the cavity, exactly overlap with themselves. The classic FP interferometer consisting of two plane reflective surfaces is hence not considered a cavity in this sense since light diverges with consecutive roundtrips. Three examples of FP resonators, two of which are stable optical cavities, are shown in Figure 2.1.

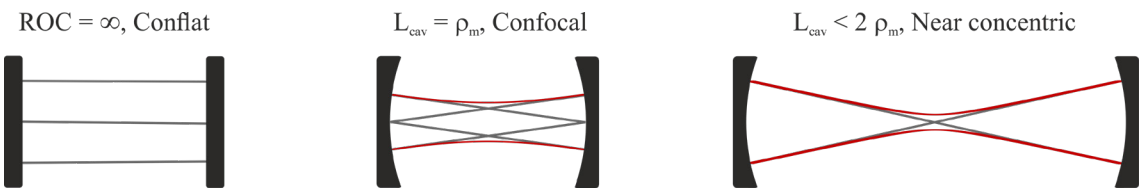

Figure 2.1. Three types of Fabry-Pérot resonators. The conflat resonator does not support stable optical modes.

The stable modes in FP cavities are well known due to their relevance as laser resonators [49]. At the surfaces of the mirrors, the radius of curvature ρ_{pf} of the phase front of stable modes equals the radius of curvature ρ_m of the cavity mirrors [50]. This criterion can be fulfilled by Gaussian modes, whose approximately spherical phase front is defined by its radius [51]

$$\rho_{pf}(z) = (z - z_{center})\left(1+\left(\frac{z_0}{(z-z_{center})}\right)^2\right). \tag{2.1}$$

Herein, z is the direction of propagation (the cavity axis), z_{center} is the beam waist position and z_0 is the confocal parameter describing the divergence of the mode. Inserting $\rho_{pf}(0) = \rho_{m,1}$ and $\rho_{pf}(L_{cav}) = \rho_{m,2}$ in (2.1), with L_{cav} being the cavity length and subscript 1 and 2 denoting the first and second mirror, allows solving for z_{center} and z_0. It is convenient to define the parameters $\eta_i = 1 - \frac{L_{cav}}{\rho_{m,i}}$ for each mirror (often called "stability parameter" and denoted by g_i in literature) [50]. The solutions are then given by

$$z_{center} = L_{cav}\frac{(1-\eta_1)\eta_2}{\eta_1 + \eta_2 - 2\eta_1\eta_2} \tag{2.2}$$

and

$$z_0 = \frac{L_{cav}}{\eta_1+\eta_2-2\eta_1\eta_2}\sqrt{\eta_1\eta_2(1-\eta_1\eta_2)}. \tag{2.3}$$

From (2.3), it follows that real valued solutions for z_0 and hence stable modes exist only if the stability criterion

$$0 < \eta_1 \eta_2 < 1 \tag{2.4}$$

is fulfilled. The only exception to the stability criterion (2.4) is the stable confocal cavity, for which $\eta_1 = \eta_2 = 0$. The radial intensity profile of the Gaussian mode is given by

$$I(r) = I_0 \frac{w_0^2}{w^2(z)} \exp\left(-\frac{2r^2}{w^2(z)}\right) \tag{2.5}$$

The $1/e^2$ - beam radius $w(z)$ is related to z_{center} and z_0 via

$$w(z) = w_0 \sqrt{1 + \left(\frac{z - z_{center}}{z_0}\right)^2} \tag{2.6}$$

Herein, $w_0 = w(z_{center}) = \sqrt{\lambda * \frac{z_0}{\pi}}$ is the beam waist radius.

$$w_0^2 = \frac{\lambda L_{cav}}{\pi} \frac{\sqrt{\eta_1 \eta_2 (1 - \eta_1 \eta_2)}}{|\eta_1 + \eta_2 - 2\eta_1 \eta_2|} \tag{2.7}$$

Most cavities employed in CES are symmetric, $\rho_{m,1} = \rho_{m,2}$, $\eta_1 = \eta_2 = \eta$. In the symmetric case, the beam waist $w_{0,sym}$ is in the center of the cavity, $z_{center} = L_{cav}/2$, and given by

$$w_{0,sym}^2 = \frac{\lambda L_{cav}}{\pi} \frac{\sqrt{(1 - \eta^2)}}{2|1 - \eta|} \tag{2.8}$$

Figure 2.2 shows $w(z)$ (Equation (2.6)) of the Gaussian mode for a symmetric cavity with $\rho_m = 15$ cm at varying L_{cav}.

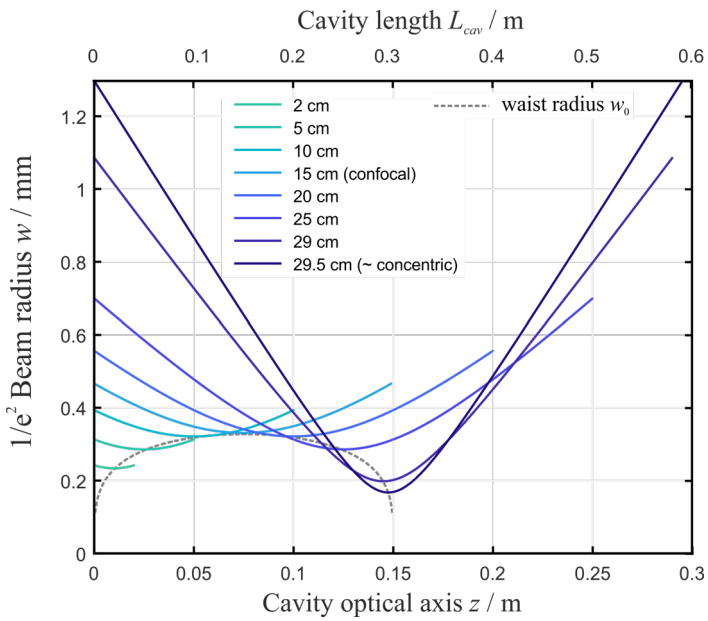

Figure 2.2. Solid lines, bottom axis: $1/e^2$ radius $w(z)$ of the fundamental Gaussian mode of a symmetric Fabry-Pérot cavity with $\rho_m = 15$ cm for different cavity length (as indicated) along the cavity axis z. Dashed line, top axis: Waist radius w_0 versus cavity length L_{cav}.

As will be discussed in section 5.3.1, the cavity mode is an important design consideration in CES. The confocal configuration has the largest beam waist and smallest divergence. This is beneficial to reduce the intracavity intensity to avoid optical saturation. The concentric cavity has a small beam waist suitable for intracavity QEPAS (section 5.3). It should be noted that, besides the fundamental Gaussian mode, other modes of suitable phase front curvature exist. The Laguerre Gaussian modes as well as the Hermite Gaussian modes feature the same phase front curvature as the Gaussian mode and are hence stable modes of the FP cavity [49–51]. In an experiment, these so called "higher order modes" can be observed if the mode-matching of the incoupling beam is not optimized [52]. The resonance frequency of higher order modes is shifted to higher frequencies due to the additional Gouy phase of these modes [48]. The appearance of additional resonances of small amplitudes is hence a clear indication of poor alignment and inadequate mode-matching.

2.1.2. Spectral Transmission and Resonances

Due to their resonant nature, all optical cavities show well defined resonance frequencies for which light is coupled into and transmitted through the resonator. Neglecting phase shifts upon reflection as well as the Gouy phase of the cavity mode, the transmission profile $T_{cav}(\tilde{\nu})$ of a FP cavity with two identical mirrors of reflectivity R and transmission T is described by [50]

$$T_{cav}(\tilde{\nu}) = \frac{T^2}{(1-R)^2}\left[1 + \frac{4R\sin^2(2\pi L_{cav}\tilde{\nu})}{(1-R)^2}\right]^{-1} \tag{2.9}$$

Equation (2.9), sometimes referred to as *Airy function*, is plotted for $T = 1 - R$ and different R in Figure 2.3. The transmission spectrum shows evenly spaced resonances. The spacing between consecutive resonances, commonly referred to as free spectral range (FSR), is given by

$$FSR = \frac{1}{2nL_{cav}} \tag{2.10}$$

Herein, n is the refractive index of the gas in the cavity. The comb-like structure of cavity resonances is used in CES as a frequency ruler and spectra are usually recorded by stepping $\tilde{\nu}$ across consecutive resonances while keeping the L_{cav} and n fixed. Alternatively, a given cavity resonance $\tilde{\nu}_{res}$ can be tuned by changing the cavity length, *e.g.* via a piezoelectric actuator. The change in resonance frequency is hereby given by

$$\frac{d\tilde{\nu}_{res}}{dL_{cav}} = -\frac{\tilde{\nu}_{res}}{2nL_{cav}}. \tag{2.11}$$

As can be seen from Figure 2.3, the resonances become increasingly sharp with increasing mirror reflectivity (decreasing round-trip losses).

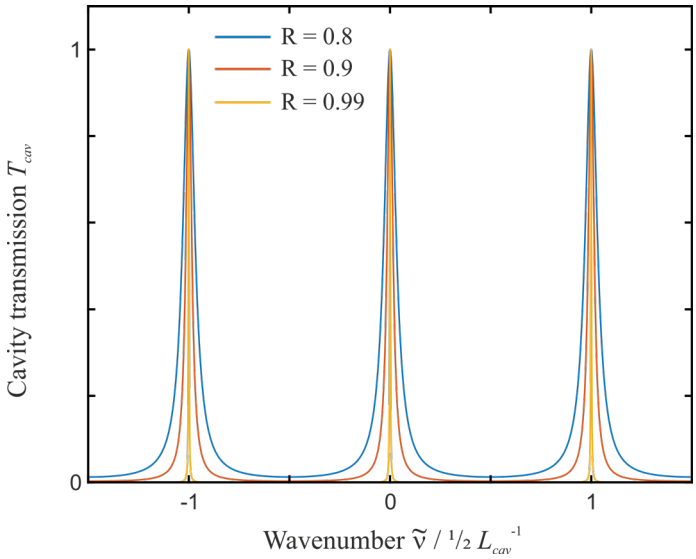

Figure 2.3. Transmission of a FP cavity with two identical mirrors calculated using equation (2.9) for different mirror reflectivity R and $T = 1\text{-}R$.

For $R > \sim 0.9$, the resonance profile can be approximated by a Lorentzian function. The full width at half maximum (FWHM) of the Lorentzian resonance profile is given by

$$FWHM = \frac{1}{2\pi n L_{cav}} \frac{1-R}{\sqrt{R}} \tag{2.12}$$

Typical parameters for cavities employed for CES are $\sim 0.1\ \mathrm{m} < L_{cav} < 1\ \mathrm{m}$ and $0.99 < R < 0.9999$. Therefore, the resonances can be extremely narrow, between $10^{-4}\ \mathrm{cm}^{-1} < FWHM < 10^{-7}\ \mathrm{cm}^{-1}$ for the values of L_{cav} and R given above. The challenges associated with this stringent resonance condition and ways to tackle them will be discussed in sections 2.3, 2.4 and 2.5.

The ratio between FSR and FWHM of a cavity defines the finesse F of a cavity.

$$F = \frac{FSR}{FWHM} = \pi \frac{\sqrt{R}}{1-R} \approx \frac{\pi}{1-R} \tag{2.13}$$

Herein, the approximate equal sign holds for R close to unity. F is an important parameter to characterize optical cavities since the pathlength enhancement as well as power enhancement of a cavity on resonance are directly proportional to F.

2.2. Pathlength – and Power Enhancement in High-Finesse Cavities

2.2.1. The Fabry-Pérot Cavity

On resonance, the cavity transmission T_{cav} of a symmetric FP cavity is given by [53,54]

$$T_{cav} = \frac{P_{trans}}{P_0} = \frac{T^2}{(1-R+\alpha L_{cav})^2} \approx \frac{T^2}{(1-R)^2}\left(1 - \frac{2\alpha L_{cav}}{1-R}\right) \tag{2.14}$$

Herein, $2\alpha L_{cav}$ are round-trip losses due to absorption of gas in the cavity, but can also include other losses, such as scattering losses or losses at an aperture inside the cavity. The

approximate equal sign holds for $2\alpha L_{cav} \ll 1 - R$. The reflectivity R of both mirrors is assumed equal. The measured absorption from the gas,

$$1 - \frac{T_{cav}(\alpha)}{T_{cav}(\alpha = 0)} = \frac{2\alpha L_{cav}}{1 - R} = \frac{2}{\pi} F \alpha L_{cav} \tag{2.15}$$

is increased as compared to the absorption αL_{cav} on a single passage through the cavity length by a factor close to the cavity finesse F. It is important to note that this is only true at an exact resonance wavelength of the cavity. If the cavity is used in a non-resonant fashion, *e.g.* when broad-band light sources are used or in cavity ring-down spectroscopy, the increase in pathlength is decreased by a factor 2 [48].

The power P_{intra} circulating inside a cavity can be simply derived by considering that the transmitted light, since it is transmitted through the rear cavity mirror, must be equal to the optical power impinging on that mirror, *i.e.* $P_{intra}/2$, times the transmission T of the mirror.

$$P_{intra} = 2P_0 \frac{T_{cav}}{T} = 2P_0 \frac{2T}{(1 - R + \alpha L)^2} \approx 2P_0 \frac{T}{(1 - R)^2} \left(1 - \frac{2\alpha L_{cav}}{(1 - R)}\right) \tag{2.16}$$

Herein, the factor of two originates from the sum of light passing through any plane perpendicular to the cavity axis in both directions, while only one direction contributes to the transmission through the rear mirror. For $T \approx 1 - R$ and $\alpha = 0$, the intracavity power enhancement P_{intra}/P_0 equals the pathlength enhancement given by $2F/\pi$. Especially for mirrors of high R, T is often significantly smaller than R, yielding a strongly decreased power enhancement. This is illustrated in Figure 2.4, which shows P_{intra}/P_0 (compare (2.16)) against mirror losses $1 - R$ for different levels of absorption and scattering losses $\ell_{AS} = 1 - R - T$.

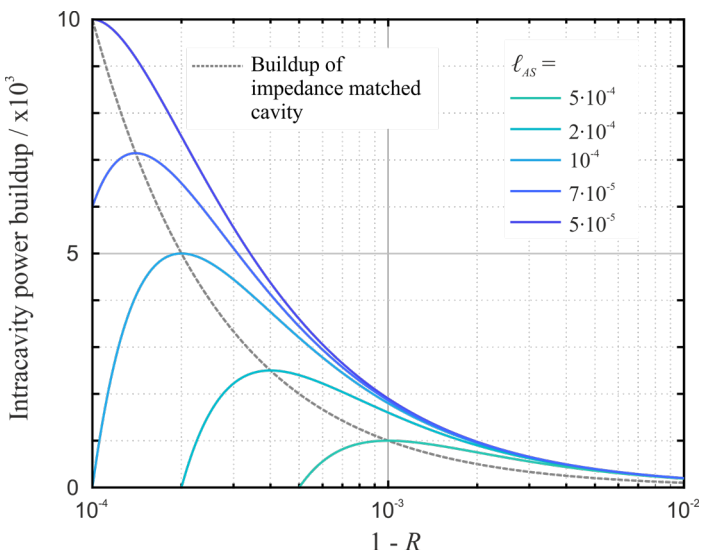

Figure 2.4. Intracavity power buildup P_{intra}/P_0 in a symmetric FP cavity with different absorption and scattering losses ℓ_{AS} of the mirrors plotted against overall mirror losses $1 - R$.

For a given L_{AS} of a mirror, the maximum power buildup without gas absorption ($\alpha = 0$),

$$\frac{P_{intra,max}}{P_0} = \frac{1}{1 - R_{max}} = \frac{1}{1 - 2L_{AS}} \tag{2.17}$$

is found for $R_{max} = 2\ell_{AS}$ or, equivalently, $T_{max} = \ell_{AS}$. Mirrors fulfilling this criterion are sometimes referred to as optically impedance matched. Increasing the mirror reflectivity R and cavity finesse F only increases the power buildup as long as the mirror transmission is larger than the combined other mirror (and cavity) losses. For dielectric mirrors, R and T are defined by the coating design and can hence not be adjusted for a given pair of mirrors. In the next section, a different cavity design is introduced that does allow adjusting R and T freely to achieve maximum power buildup, namely the Brewster window cavity.

It should be stressed that the optical pathlength enhancement (compare equation (2.15)) is independent from the mirror transmission and increases steadily with F (although some cavity transmission is, of course, necessary). Hence, the cavity and cavity mirrors for indirect and direct cavity enhanced spectroscopy follow different design considerations, as will be discussed in more detail in section 5.3.1.

2.2.2. The Brewster Window Cavity

Due to its use in this work, the Brewster window (BW) cavity will be introduced in this section and its pathlength- and power enhancement factors will be derived. The BW cavity illustrated in Figure 2.5 is a FP cavity into which a transparent window of refractive index n is inserted at an angle β, defined between the cavity axis and the surface normal of the BW, close to Brewster's angle $\beta_B = \arctan(n/n_{air})$ anywhere along the cavity axis [55].

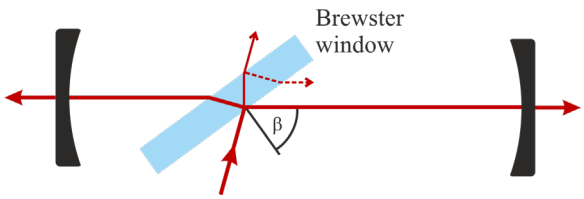

Figure 2.5. Basic schematic of the Brewster window (BW) cavity. Light can be coupled into the cavity via transmission through a cavity mirror, reflection off the front surface and rear surface of the BW.

For p-polarized light, the loss at the BW upon Fresnel reflection R_{BW} is given by [25,56]

$$R_{BW} = \left| \frac{n^2\cos(\beta) - n_{air}\sqrt{n^2 - n_{air}^2\sin^2(\beta)}}{n^2\cos(\beta) + n_{air}\sqrt{n^2 - n_{air}^2\sin^2(\beta)}} \right|^2 \approx \frac{(n^4-1)^2}{4n^6}(\beta - \beta_B)^2 \tag{2.18}$$

Herein, the approximate equal sign holds for the refractive index of air $n_{air} \approx 1$ and $\beta \approx \beta_B$ (inserted in radians in (2.18)).

Although light can be coupled into the BW cavity through the mirrors, it is more useful to couple in *via* reflection at the BW. This has two important advantages: First, it allows

exploiting optical feedback for stabilizing the laser wavelength to the cavity since only resonant light is reflected back to the laser (compare section 2.5). Second, since R_{BW} can be tuned via β, it can be optimized for maximum power enhancement.

The intracavity power $P_{intra,BW}$ and reflectivity $R_{cav,BW}$ of the BW cavity can be derived directly from equations (2.14) and (2.16) given above by defining an equivalent FP cavity. As illustrated in Figure 2.6, this is achieved by collecting the losses for a round trip through the BW cavity and defining the mirrors' reflectivity R_{eq} of the equivalent FP cavity such that the losses match those of the BW cavity and their transmission T_{eq} corresponds to R_{BW}.

$$\begin{aligned} R_{eq} &= R \cdot T_{BW}^2 \approx R - 2R_{BW} \\ T_{eq} &= R \cdot R_{BW} \approx R_{BW} \end{aligned} \tag{2.19}$$

Herein, the first approximation holds for small R_{BW} and $R_{BW} = 1 - T_{BW}$, the latter approximation holds for $R_M \approx 1$. Substituting T_{eq} for T and R_{eq} for R in (2.14) and (2.16) yields

$$P_{intra,BW} = P_0 \frac{2R_{BW}}{(1 - R + 2R_{BW} + \alpha L)^2} \tag{2.20}$$

$$T_{cav,eq} = R_{cav,BW} = \frac{2R_{BW}^2}{(1 - R + 2R_{BW} + \alpha L)^2} \tag{2.21}$$

The largest buildup $\frac{P_{intra,BW}}{P_0} = \frac{1}{4}\frac{1}{(1-R+\alpha L)}$ is found for $R_{BW} = \frac{1}{2}(1 - R + \alpha L)$, *i.e.* for R_{BW} matching half the combined half round-trip losses of all other elements in the cavity. In section 5.3.1, experimental results on finding this so called optical impedance matching condition by changing the BW angle β will be shown.

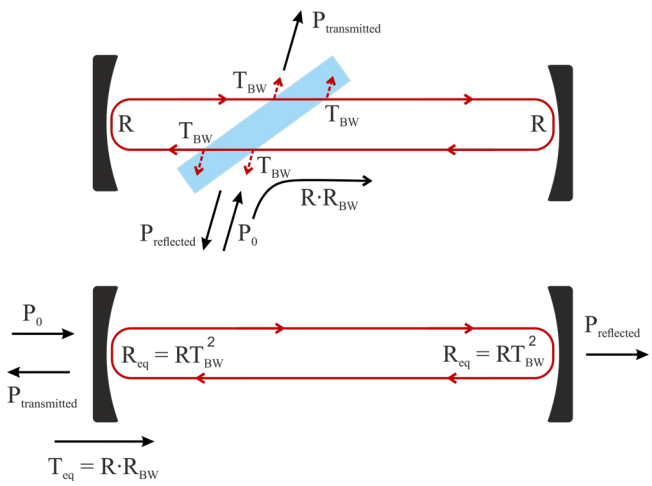

Figure 2.6: Illustration of the round-trip losses of the Brewster window (BW) cavity (top) and the equivalent FP cavity (bottom).

So far, coupling into the cavity was assumed to only occur due to reflection at the front surface of the BW. Depending on the cavity design, Brewster window thickness and alignment of the incoming beam, light reflected off the rear surface of the BW may also couple to the cavity. In particular if the BW is thin as compared to the $1/e^2$ radius w of the cavity mode, the displacement of the beam reflected off the rear surface (dashed line in Figure 2.5) from the one reflected off the front surface is sufficiently small to also couple to cavity modes. In this case, the two reflections will overlap and interfere. Since the phase of interference changes with wavelength, an etalon effect is observed in the cavity transmission and buildup. For thick BWs, the displacement of the second beam may be so large that the alignment for this beam is too far off to yield noticeable coupling to cavity modes. Otherwise, coupling of the rear beam can be avoided by means of spatial filtering using an aperture inside the cavity that increases the losses for higher order modes. Furthermore, contributions from reflections off the rear surface can be avoided by using a slightly wedged window. If the angle of the wedge is carefully chosen such that the rear surface is at the exact Brewster's angle, this offers the additional advantage of eliminating reflective losses at this surface and increasing the maximum cavity buildup and reflection by a factor of two as compared to equations (2.20), (2.21) (compare section 7.2).

2.3. Coupling Light into High-Finesse Cavities: Setup of a Cavity, Mode-Matching and Frequency Noise

Coupling light into a high finesse cavity begins on a design level. Estimating the expected finesse and transmission of a cavity gives a feeling for the expected complexity of cavity alignment. In particular, the FWHM of resonances as compared to the laser linewidth is an important factor to be taken into account. The short term linewidth (ms timescales, excluding slow frequency drifts) of most semiconductor lasers is on the order of a few MHz or even above ten MHz [57]. Since this is much larger than the FWHM of typical high finesse cavities, only a small fraction of the emitted laser power is resonant with the cavity, which drastically decreases the overall cavity transmission and makes cavity alignment accordingly harder since small signals from misaligned cavities remain buried in the noise floor. Therefore, the first step in implementing a CES setup may be to characterize and reduce the frequency noise of the free running laser (compare section 2.4.1).

Another important design consideration that must be addressed prior to the experimental setup of the cavity is mode-matching [57]. Mode-matching refers to the spatial overlapping of the laser beam with the desired mode of the cavity (usually the fundamental Gaussian mode), such that the beam waist position and divergence are identical to the cavity mode. This is achieved using appropriately positioned lenses or focusing mirrors. To design the focusing lens arrangement for mode-matching, the waist position and divergence of the laser beam must be known, either from specifications by the manufacturer or from

measurements using *e.g.* beam profiling cameras or the knife-edge technique[58,59]. The correct lens arrangement for mode-matching can be found using the ABCD-matrix formalism to calculate the propagation of the Gaussian beam through the optical elements [51,60]. Note that the transmission through the substrate of the coupling mirror, which typically acts as a plano-concave lens, must be included in the calculations. Commercial as well as free-ware computer programs, such as Winlens 3D [61], are a convenient choice to rapidly simulate and visualize Gaussian beam propagation through lens arrangements and to find the right lens positions and focal lengths for mode-matching. In principle, arrangements of different numbers of lenses of different focal lengths can be used for mode-matching. Typically, two lenses are used to have full control over the beam waist position and divergence. The focal lengths of the lenses should not be chosen too short in order to increase the positioning tolerance.

An excellent introduction to the experimental procedures for setting up and aligning high finesse FP-cavities was given, amongst others, by Fox *et al.* [57]. For invisible light (IR, UV), visible alignment lasers should be used if possible. After shaping the incoming beam in accordance with the mode-matching calculations, the first step should be to install only the rear mirror of the FP cavity. With the beam aligned to the cavity axis (centered on front mirror position as well as rear mirror), the rear mirror is adjusted such that the beam is reflected back onto itself. Next, the front mirror is mounted in place and tilted in the same way. Now, a photodetector behind the cavity should show buildup signals as the laser wavelength is tuned across a few FSRs of the cavity. After several iterations of adjusting the cavity mirrors and the pointing of the incoming beam, signals from higher order modes that can be identified based on their shift in resonance frequency should be largely eliminated and the buildup of the fundamental mode should dominate in the swept frequency scan.

The procedure for aligning a BW cavity is similar. At the design level, the angle β and corresponding reflectivity R_{BW} of the BW should be chosen based on the (expected) mirror transmission R for sufficient reflection $R_{cav,BW}$ (compare equation (2.21)). Starting at higher R_{BW} ensures large buildups and an easier cavity alignment. Using a rotation stage, β can be adjusted after cavity alignment for optimum finesse or power buildup (compare section 5.3.2). For the first setup of the BW cavity, it is very useful to use *s*- rather than *p*-polarized light. First, the cavity finesse is very low for *s*-polarization due to the much larger reflectivity of the BW. A BW cavity well aligned for *s*-polarization is a good starting point for the high finesse *p*-polarized modes. Second, in a dark environment, it is possible to observe the beam reflected at the first mirror (right-hand mirror in Figure 2.5) and back to the laser at the BW, which is useful for aligning the incoming beam. The beam from the laser should be aligned such that it hits the first mirror at its center and is reflected back onto itself. The first mirror is aligned such that the second mirror is also hit at its center.

Since the alignment condition for the first mirror depends on the pointing of the incoming beam and vice versa, several iterations may be necessary to fulfill both conditions. Finally, once the first and second mirror are hit at their center and the beam is reflected back onto itself towards the laser, the second mirror can be adjusted. The partial beam circulating once through the cavity before being reflected back to the laser should be observable at a similar intensity as the one reflected only at the first mirror. Once this partial beam is overlapped with the incoming beam via adjustment of the second mirror, buildup signals should be observable on a photodetector placed in the beam transmitted through the Brewster window. After changing the incoming polarization to parallel, *e.g.* using a half-wave plate, the cavity mirrors and incoming beam can be adjusted based on the detector signal as described above for the FP cavity.

In principal, aligning the FP cavity as described above prior to the insertion of the BW is feasible as well. However, especially due to the possibility of exploiting low-finesse *s*-polarized modes for a first alignment, the setup of the BW cavity as described worked well during the course of this thesis and avoids the additional effort of a second beam path necessary for coupling to the BW cavity via a mirror.

As mentioned previously, the buildup in a high finesse cavity will be noisy and incomplete, even after perfect alignment and mode-matching, if the laser frequency noise (which is proportional to its linewidth) exceeds the cavity modes' FWHM. Therefore, CES often requires stabilization of the laser frequency to the cavity. The next two sections will introduce two popular ways of locking the laser frequency to a cavity resonance.

2.4. Pound-Drever-Hall Locking

The most widely employed technique for locking the frequency of a laser to a cavity resonance is Pound-Drever-Hall (PDH) locking [62]. The technique was originally developed for the laser interferometry gravitational-wave observatory (LIGO) [63,64] and was employed in a large number of CES experiments since then.

PDH locking is based on establishing an electronic feedback loop that uses some signal that is proportional to the detuning $\Delta\tilde{\nu} = \tilde{\nu} - \tilde{\nu}_{res}$ between the laser frequency $\tilde{\nu}$ and the cavity resonance frequency $\tilde{\nu}_{res}$ ("error signal") as an input and acts on the laser frequency, *e.g.* via the laser current, to minimize the detuning (compare Figure 2.7). To be useful in a feedback loop, the error signal must be signed, *i.e.* it must have opposite sign for $\pm\Delta\tilde{\nu}$. The cavity transmission signal is no suitable error signal since it is symmetric around $\tilde{\nu}_{res}$ (compare Figure 2.3). The same problem is encountered whenever a laser is to be locked to the top of some resonance, which is often tackled by modulation techniques.

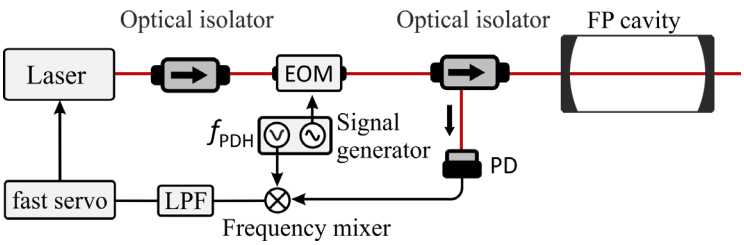

Figure 2.7. Schematic of a setup for PDH locking a laser to a FP cavity. EOM: electro optic modulator, PD: photodetector, LPF: low pass filter

This also applies to PDH locking. Here, laser frequency modulation (FM) is applied, *e.g.* using an electro-optic modulator or via direct current modulation, at a frequency f_{PDH} that is much larger than the FWHM of the cavity mode. As will be discussed below, the signal from a photodetector (PD) recording the backreflected light, demodulated at f_{PDH}, gives a signed error signal that is used for the electronic feedback loop. To avoid optical feedback from the cavity, optical isolators, *e.g.* Faraday isolators, are used. Optical isolators are also used to pick up the backreflection from the cavity without attenuating the beam in the forward direction.

The back-reflected light at the PD can be described in the time domain as the inverse Fourier transform of the complex amplitude spectrum of the incident light $E_0(\tilde{\nu})$ multiplied by a complex valued function $\mathcal{H}_{r,FP}(\tilde{\nu})$ describing the response of the cavity (its reflection coefficient).

$$E_r = \int E_0(\tilde{\nu}) \exp(-i \cdot 2\pi\tilde{\nu}ct)\, \mathcal{H}_{r,FP}(\tilde{\nu}) \mathrm{d}\tilde{\nu} \tag{2.22}$$

For a symmetric FP cavity with mirror transmission and reflection coefficients t_m and r_m, respectively, $\mathcal{H}_{r,FP}(\tilde{\nu})$ is given by

$$\mathcal{H}_{r,FP} := \frac{E_r(\tilde{\nu})}{E_0(\tilde{\nu})} = r - \frac{t_m^2 r_m}{\exp(i \cdot 4\pi\tilde{\nu}nL_{cav}) - r_m^2} \tag{2.23}$$

The spectrum $E_0(\tilde{\nu})$ of a FM laser field with modulation frequency f_{PDH} is composed of discrete lines of amplitudes $E_0 \cdot J_{B,j}(\xi)$ shifted in frequency from the center frequency $\tilde{\nu}_c$ by $j\frac{f_{PDH}}{c}$, with $j = \ldots, -2, -1, 0, 1, 2, \ldots$. $J_{B,j}$ is the j-th order Bessel-function of the first kind and $\xi = c \cdot \delta\tilde{\nu}/f_{PDH}$ is the modulation depth, with $\delta\tilde{\nu}$ being the amplitude of the modulation of instantaneous frequency. For PDH locking, typically $\xi \ll 1$, so only $j = -1, 0, 1$ have significant amplitude. Hence, E_r is given by

$$E_r = E_0 \cdot \sum_{j=-1}^{1} J_{B,j}(\xi) \exp\left(-i \cdot 2\pi\left(\tilde{\nu}_c + j\frac{f_{PDH}}{c}\right)ct\right) \cdot \left[r - \frac{t_m^2 r_m}{\exp\left(i \cdot 4\pi\left(\tilde{\nu}_c + j\frac{f_{PDH}}{c}\right)nL_{cav}\right) - r_m^2}\right] \tag{2.24}$$

The intensity I_r at the detector is proportional to $|E_r|^2 = E_r E_r^*$. The product of the summands in (2.24) yields, besides non-oscillating terms, terms oscillating at frequencies

f_{PDH} and $2 \cdot f_{PDH}$ [62]. With $J_{B,-1} = -J_{B,1}$ and ignoring terms oscillating at $2 \cdot f_{PDH}$, I_r can be written as

$$\begin{aligned} I_r &= I_0 \left[\sum_{j=-1}^{1} J_{B,j}^2 \left| \mathcal{H}_{r,FP}\left(\tilde{\nu}_c + j\frac{f_{PDH}}{c}\right)\right|^2 \right. \\ &+ 2J_{B,1}J_{B,0} \left[\mathrm{Re}\left(\mathcal{H}_{r,FP}(\tilde{\nu}_c)\, \mathcal{H}_{r,FP}^*\left(\tilde{\nu}_c + \frac{f_{PDH}}{c}\right) - \mathcal{H}_{r,FP}^*(\tilde{\nu}_c)\, \mathcal{H}_{r,FP}\left(\tilde{\nu}_c - \frac{f_{PDH}}{c}\right)\right) \cos(2\pi f_{PDH} t) \right. \\ &\left. \left. + \mathrm{Im}\left(\mathcal{H}_{r,FP}(\tilde{\nu}_c)\, \mathcal{H}_{r,FP}^*\left(\tilde{\nu}_c + \frac{f_{PDH}}{c}\right) - \mathcal{H}_{r,FP}^*(\tilde{\nu}_c)\, \mathcal{H}_{r,FP}\left(\tilde{\nu}_c - \frac{f_{PDH}}{c}\right)\right) \sin(2\pi f_{PDH} t) \right] + \cdots \right] \end{aligned} \tag{2.25}$$

Herein, Re and Im denote the real and imaginary part, respectively, of an expression. In PDH-locking, the signal oscillating at f_{PDH} is shifted in frequency to DC using a frequency mixer and isolated from signals at other frequencies by means of low-pass filtering. The phase of the reference frequency for the frequency mixer is chosen to be 90° relative to the laser FM, which effectively isolates the sine term in (2.25). The resulting error signal is then given by

$$\begin{aligned} Y_{err} = I_0 \cdot J_{B,1}J_{B,0} \\ \cdot \mathrm{Im}\left(\mathcal{H}_{r,FP}(\tilde{\nu}_c)\, \mathcal{H}_{r,FP}^*\left(\tilde{\nu}_c + \frac{f_{PDH}}{c}\right) \right. \\ \left. - \mathcal{H}_{r,FP}^*(\tilde{\nu}_c)\, \mathcal{H}_{r,FP}\left(\tilde{\nu}_c - \frac{f_{PDH}}{c}\right)\right) \end{aligned} \tag{2.26}$$

The error signal calculated for a cavity of varying finesse F is shown in Figure 2.8. At the resonance frequency, Y_{err} is zero and has a steep slope $dY_{err}/d\Delta\tilde{\nu}$ within a range defined by the FWHM of the cavity resonance. Hence, a servo that acts on the laser frequency and whose output is proportional to $-Y_{err}$ will tune $\tilde{\nu}$ to the cavity resonance and lock the laser.

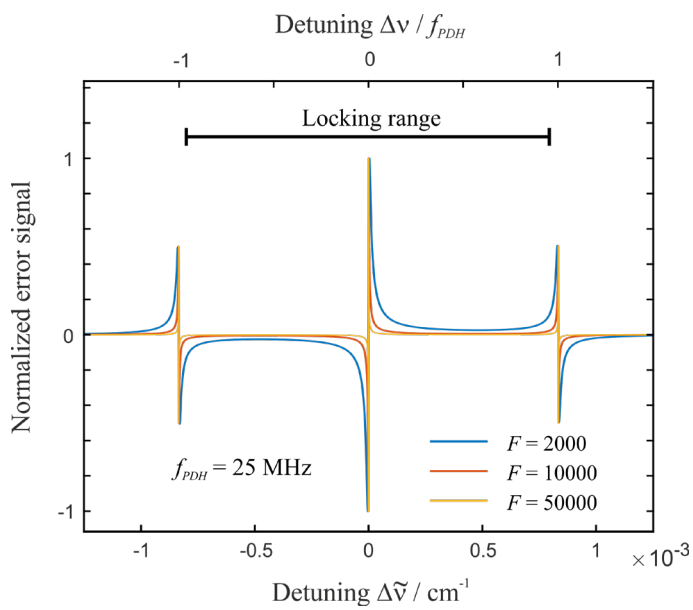

Figure 2.8. Pound-Drever-Hall error signal Y_{PDH}, calculated for FP cavities of $L = 30$ cm and varying finesse F as indicated for a modulation frequency $f_{PDH} = 25$ MHz.

For larger detuning up to $|\Delta\tilde{\nu}| < f_{PDH}$, the (absolute) error signal decreases with a more shallow slope. Nevertheless, within this range, the servo will still tune $\tilde{\nu}$ towards the resonance frequency. As an example, let us follow Y_{err} for $F = 2000$ in Figure 2.8 starting at $\Delta\tilde{\nu} \approx 0.25\, f_{PDH}$. Since Y_{err} is positive, the servo will decrease $\tilde{\nu}$ (since its output is proportional to $-Y_{err}$). Hence, Y_{err} will increase and $\tilde{\nu}$ will be further decreased, until $\Delta\tilde{\nu}$ approaches zero. For $\Delta\tilde{\nu} < 0$, Y_{err} is negative, yielding a tuning towards larger $\tilde{\nu}$ by the servo. In practice, the locking range can be smaller than $|\Delta\tilde{\nu}| < f_{PDH}$ because the error signal around $|\Delta\tilde{\nu}| = f_{PDH}/2$ is too small.

2.4.1. Practical Aspects of PDH Locking

Achieving a tight frequency lock between a laser and a high finesse cavity by PDH locking requires careful experimental design. A practical overview of PDH locking of diode lasers was given by Fox *et al.* [57]. First, the necessary bandwidth and frequency response of the feedback loop must be considered. The necessary bandwidth depends on the spectrum of the frequency noise of the laser. Due to their short laser resonators, semiconductor lasers without external cavities typically exhibit considerable frequency noise up to tens of MHz. Hence, the required bandwidth of the servo must be accordingly high to correct for these fast fluctuations. In addition to having a high bandwidth, the gain and phase of the feedback loop must be tailored to the FM response of the laser [65]. Achieving this for the whole locking bandwidth requires knowledge of the FM response of the laser. In semiconductor lasers, frequency tuning with injection current follows different mechanisms: thermal tuning and tuning with carrier density [57]. At low frequencies, thermal tuning dominates. At frequencies > ~1 MHz, frequency tuning is driven by changes in carrier density (plasma effect [66]), which has opposite sign as compared to thermal tuning. This yields a complex amplitude and phase response of laser frequency with injection current [26,33,67] that must be compensated by the feedback loop.

Next, the signal to noise ratio (SNR) of the error signal must be sufficiently high, even for the free-running laser. Since the error signal is obtained from a measurement of backreflection from the cavity, which is close to one for almost all $\tilde{\nu}$ except the resonance frequency, the error signal is measured with a very large background intensity (non-oscillatory terms in (2.25)). Although this background is centered around DC and should ideally not contribute to the error signal, intensity noise from the laser at frequencies close to f_{PDH} will contribute to the noise floor of the error signal. On the other hand, the PDH error signal obtained when scanning the free running laser across a cavity resonance will typically be much smaller than the signal calculated using (2.26) since the linewidth of the laser is much larger than the cavity resonance and a convolution of Figure 2.8 with the emission spectrum of the laser is observed. A too large discrepancy between the laser linewidth and the FWHM of the cavity mode will hence not allow for observing an error signal of sufficient quality to lock the laser. In this case, the laser frequency noise must be

reduced before PDH locking. For semiconductor lasers this is typically achieved using an external cavity (EC) laser design. In EC lasers, the current tuning rate $\frac{d\tilde{\nu}}{dj}$ is approximately reduced by a factor $\left(1+\frac{L_{EC}}{nL_{FP}}\right)^{-1}$, where L_{EC} and L_{FP} are the length of the external cavity and the FP laser resonator and n is the refractive index of the FP resonator [68]. Therefore, the impact of laser current noise, which is typically the dominant source of noise in semiconductor lasers and especially in quantum cascade lasers (QCL), on the frequency noise of the laser is strongly decreased (compare Figure 6.3), yielding an improved SNR of the PDH error signal.

So far, the discussion was limited to purely FM modulated laser fields. In practice, however, frequency modulation is always accompanied by residual amplitude modulation (RAM), which causes an offset of Y_{err} from zero as well as a small asymmetry of the PDH error signal. For well-adjusted electro-optic modulators, RAM is usually negligible. Under direct current modulation, however, the laser intensity follows the modulated current, yielding large RAM. While the offset can, in principle, be subtracted from Y_{err}, slow drifts of the background remain. Since the exact offset to be subtracted depends on the laser intensity reaching the detector, any small change in intensity, *e.g.* due to drifts of the laser itself or etalons or absorption in the beam path, would shift Y_{err} up or down in Figure 2.8. Hence, the locking point (zero crossing of Y_{err}) would be shifted from the exact resonance frequency. Also, offsets decrease the locking range because Y_{err} changes sign on one side of the cavity resonance around $|\Delta\tilde{\nu}| \approx 0.5\, f_{PDH}$.

Despite the discussed difficulties in PDH locking of semiconductor lasers to high finesse cavities, the technique has been successfully implemented in a large variety of CES applications [69]. In particular for semiconductor lasers exhibiting relatively large frequency noise, optical feedback locking can be a more straight forward alternative that shall be discussed in the following.

2.5. Optical Feedback Locking

Lasers are well known to be sensitive to (re-)injection of light into the gain medium. Optical feedback (OF, light from the laser reflected back into itself) and injection (injection of light from another laser) is usually avoided using optical isolators or tilted optical elements since it may lead to increased frequency and intensity noise or even damage to the device. OF and optical injection can, however, also be exploited to stabilize the laser frequency to the frequency of another laser (optical injection locking [70,71]) or to optical cavities. Optical feedback locking will be used in section 5.3 for exciting photoacoustic signals within a cavity at high efficiency and low noise and will hence be discussed in some detail in the following.

Under OF, the source of the feedback (here the cavity) can be considered as a second resonator in addition to the laser resonator (*e.g.* the DFB resonator). The laser emission is

hence a solution to the coupled system of laser and cavity [72]. For weak feedback, the frequency $\tilde{\nu}$ emitted by the coupled semiconductor laser is related to the frequency $\tilde{\nu}_{free}$ of the free running laser (without OF) in an implicit form as [73]

$$\tilde{\nu}_{free} = \tilde{\nu} + \frac{\sqrt{\kappa(1+\alpha_H^2)}}{4\pi^2\tau_{DL}c}\left[\mathrm{Re}\big(\mathcal{H}(\tilde{\nu})\big)\sin(4\pi\tilde{\nu}d_{cav-las} + \arctan(\alpha)) - \mathrm{Im}\big(\mathcal{H}(\tilde{\nu})\big)\cos(4\pi\tilde{\nu}d_{cav-las} + \arctan(\alpha))\right] \tag{2.27}$$

Herein, $\kappa = P_{OF}/P_0$ is the feedback rate, with P_{OF} and P_0 being the optical power reflected back into the laser and emitted by the laser, respectively, α_H is the Henry factor (also known as linewidth enhancement factor [74]), τ_{DL} is the photon lifetime of the laser resonator (equivalent to ring-down time, compare section 2.6), $d_{cav-las}$ is the laser-cavity distance and $\mathcal{H}(\tilde{\nu})$ is the transfer function of the cavity defined in equation (2.23).

In section 2.2.2, the reflectivity $R_{cav,BW} = \left|\mathcal{H}_{r,BW}(\tilde{\nu})\right|^2$ of the BW cavity on resonance was derived from the results for the FP cavity by defining an equivalent FP cavity (compare Figure 2.6). In the same way, $\mathcal{H}_{r,BW}(\tilde{\nu})$ can be derived from the transmission (!) transfer function $\mathcal{H}_{t,FP}(\tilde{\nu})$ of the FP cavity [48]

$$\mathcal{H}_{t,FP}(\tilde{\nu}) := \frac{E_t}{E_0} = \frac{t_{m,1}t_{m,2}\exp(-i\cdot 2\pi\tilde{\nu}nL_{cav})}{1 - r_m^2\exp(-i\cdot 4\pi\tilde{\nu}nL_{cav})} \tag{2.28}$$

Herein, $t_{m,1}$ and $t_{m,2}$ are the transmission coefficients of the in-coupling cavity mirror and the out-coupling cavity mirror, respectively, and r_m is the reflection coefficient of the mirrors (assumed equal for both mirrors). The differentiation between $t_{m,1}$ and $t_{m,2}$ is necessary due to a small asymmetry in the BW cavity. Light is coupled into the cavity only after reflection at the BW *and* the first mirror, while the circulating optical power is coupled out via single reflection at the BW. The transmission and reflection coefficients of the equivalent FP cavity are hence

$$\begin{aligned} t_{m,1,eq} &= r_{m,BW}r_m \\ t_{m,2,eq} &= r_{m,BW} \\ r_{m,eq} &= t_{m,BW}^2 r_m \end{aligned} \tag{2.29}$$

Herein, $r_{m,BW}$ is given by the expression in absolute value brackets of equation (2.18) and $t_{m,BW} = \sqrt{T_{BW}}$. Another correction to (2.28) necessary for the BW cavity is the phase term in the numerator that corresponds to the single passage of light through the cavity. For the BW cavity, it must be replaced by the phase picked up during the passage over the distance $2d_{BW-mir}$ from the BW to the first mirror and back.

$$\mathcal{H}_{r,BW}(\tilde{\nu}) := \frac{E_{reflected,BW}}{E_0} = \frac{E_{transmitted,eq}}{E_0} = \frac{r_{m,BW}^2 r_m\exp(-i\cdot 4\pi n\tilde{\nu}d_{BW-mir})}{1 - r_m^2 t_{BW}^4\exp(-i\cdot 4\pi\tilde{\nu}nL_{cav})} \tag{2.30}$$

As before (compare section 2.2.2), the reflected amplitude $E_{reflected}$ of the BW cavity corresponds to the transmitted amplitude $E_{transmitted,eq}$ of the equivalent FP cavity (compare $P_{reflected}$ and $P_{transmitted}$ in Figure 2.6). $\mathcal{H}_{r,BW}(\tilde{\nu})$ is plotted in Figure 2.9 for an impedance matched BW cavity of $r_m = -\sqrt{0.9992}$, $r_{m,BW} = \sqrt{4\cdot 10^{-4}}$ and $t_{m,BW} = \sqrt{1 - r_{BW}^2}$ of length $L_{cav} = 28\,\mathrm{cm}$ (compare section 5.3.2).

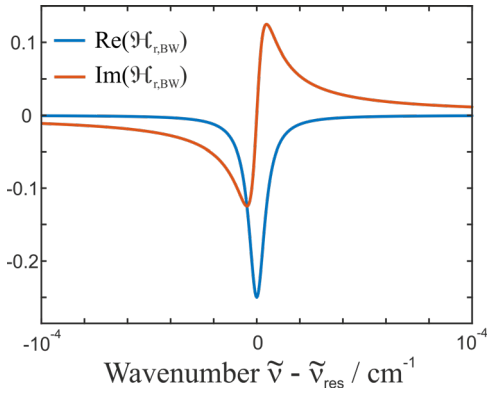

Figure 2.9. Reflective transfer function of an impedance matched BW cavity (compare equation (3.4)). $R = 0.9992$, $R_{BW} = 4{\cdot}10^{-4}$, $T_{BW} = 0.9996$, $L_{cav} = 28$ cm.

Off-resonance, the transfer function $\mathcal{H}_{r,BW}(\tilde{\nu})$ is close to zero, *i.e.* no light is back-reflected and the laser frequency $\tilde{\nu}$ is unaffected by OF. Only close to a cavity resonance, OF occurs and influences $\tilde{\nu}$. Hence, the BW cavity provides OF selectively for resonant frequencies, yielding a pulling effect on $\tilde{\nu}$ towards the cavity resonance frequency.

The laser frequency $\tilde{\nu}$ as calculated using (2.27) is shown in Figure 2.10 (left panel, dashed lines) for different $d_{cav\text{-}las}$, *i.e.* different phase of the light returning to the laser ("OF phase"). The cavity parameters were chosen as above (compare Figure 2.9). The values for $\tau_p = 30$ ps [75] and $\alpha_H = 0.5$ [76] were estimated from literature and $\kappa = 0.5$ is a rough estimate for the setup described in section 5.3.2 (the back-reflection was not attenuated artificially). Around a cavity resonance, (2.27) gives two solutions $\tilde{\nu}$ to every $\tilde{\nu}_{free}$. The actual laser frequency $\tilde{\nu}$ in a scan of $\tilde{\nu}_{free}$ depends on the scan direction (solid lines in Figure 2.10, left).

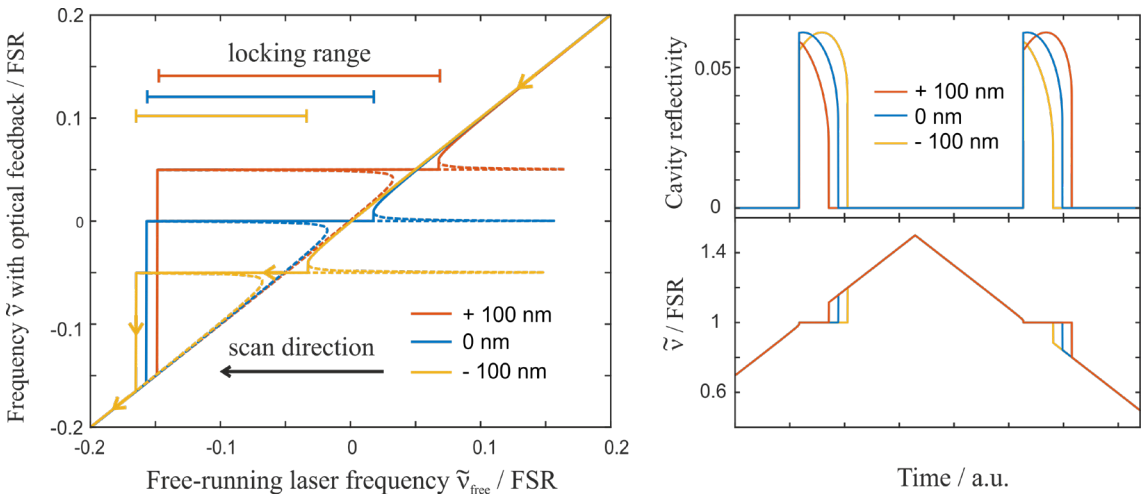

Figure 2.10. Laser frequency $\tilde{\nu}$ under the influence of optical feedback from a BW cavity. Left: Dashed lines: Function graphs of equation (2.27) for different laser-cavity distances $d_{cav\text{-}las}$ as indicated. The cavity resonance frequency was shifted by 0.05 FSR for different $d_{cav\text{-}las}$ for better visibility. When scanning $\tilde{\nu}_{free}$, frequency jumps occur ($\tilde{\nu}$, solid lines). Right, bottom: $\tilde{\nu}$ during a triangular modulation of $\tilde{\nu}_{free}$ for different $d_{cav\text{-}las}$. Right, top: Reflectivity $\left|\mathcal{H}_{r,BW}(\tilde{\nu})\right|^2$ of the cavity during the same triangular modulation.

Frequency jumps occur at the turning points. The range between the two frequency jumps in a scan is referred to as the locking range. Within this range of $\tilde{\nu}_{free}$, $\tilde{\nu}$ tunes slowly across the cavity resonance frequency. Since the locking range is much larger than the typical fluctuations of $\tilde{\nu}_{free}$, $\tilde{\nu}$ is effectively immune to noise in $\tilde{\nu}_{free}$ within the locking range, yielding stable and low-noise buildup of optical power in the cavity. Note, however, that $\tilde{\nu}$ does not come to a full stop but tunes slowly with $\tilde{\nu}_{free}$ across the cavity resonance. After the second frequency jump, $\tilde{\nu}$ returns to $\tilde{\nu}_{free}$. The OF phase ($\sim d_{cav\text{-}las}$) strongly influences the width of the locking range. As shown in the right-bottom panel of Figure 2.10, the influence of $d_{cav\text{-}las}$ on the width of the locking range is antisymmetric with respect to the scan direction of $\tilde{\nu}_{free}$: an increase of $d_{cav\text{-}las}$ yields an increase of the locking range for the positive scanning direction, while a smaller locking range is observed for the negative scanning direction, and vice-versa for a decrease of $d_{cav\text{-}las}$. The top right panel of Figure 2.10 shows the reflectivity $\left|\mathcal{H}_{r,BW}(\tilde{\nu})\right|^2$ of the BW cavity during triangular modulation of $\tilde{\nu}_{free}$. The cavity reflectivity, resembling the intracavity power buildup, varies within the locking range since $\tilde{\nu}$ slowly tunes across the cavity resonance. The shape of the buildup is indicative of the feedback phase and can be used to actively compensate for thermal drifts in $d_{cav\text{-}las}$.

2.5.1. Optical Feedback in Quantum Cascade Lasers

The first experiments with OF locking for CES were performed with diode lasers emitting in the near infrared spectral region [77,78] and the effect of OF locking was described before that for these lasers [79]. For the transfer of this technique to quantum cascade lasers (QCL), some distinct differences of these lasers as compared to diode laser must be considered. While the Henry factor α_H ranges approximately from three to eight in heterostructure diode lasers [78], it is close to zero for QCLs and can even take negative values [76,80,81]. Therefore, the effect of OF is significantly smaller in QCLs for a given feedback ratio κ. This effect, together with the particularly short carrier lifetime in QCLs, was shown to cause an enhanced tolerance of QCLs against high levels of OF, avoiding the instabilities typically observed in diode lasers at large κ [82]. Therefore, OF experiments with QCLs can be performed without attenuating the backreflected light from the cavity (compare section 5.3).

2.6. Cavity Ring-Down Spectroscopy

Amongst the techniques of CES, cavity ring-down spectroscopy (CRDS) stands out for its simplicity, its technological and commercial maturity and the number of scientific publications on the topic. For an overview over the large range of techniques and applications of CRDS, the interested reader is referred to the book by Giel Berden and Richard Engeln [83]. Here, the fundamentals of continuous wave (CW-) CRDS shall be briefly reviewed in the context of trace gas sensing.

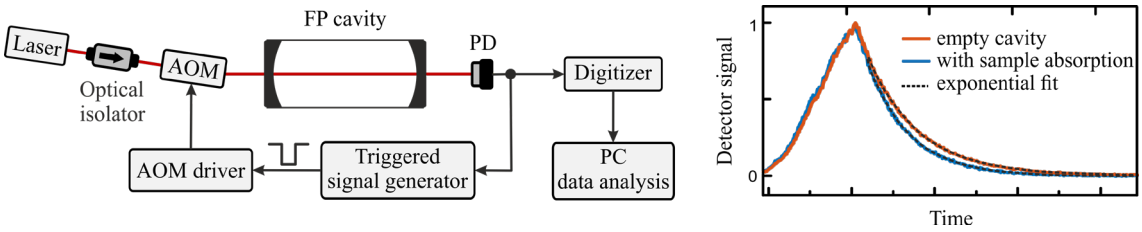

Figure 2.11. Left: Basic setup for CRDS. AOM: acousto optic modulator, PD: photodetector; Right: Exemplary ring-down signals and exponential fits recorded without absorption in the cavity ("empty cavity") and in the presence of an absorbing sample.

In CRDS, an optical cavity filled with the sample gas is illuminated by a laser (here, a CW semiconductor laser) and the transmission is monitored by a photodetector (PD, compare Figure 2.11). The laser wavelength is modulated around or fixed at a cavity resonance. When the laser comes into resonance with the cavity and the transmission signal from the PD exceeds a preset threshold, the laser is rapidly shut off, *e.g.* by triggering an acousto optic modulator or by reducing the laser current below the lasing threshold. When the laser is shut off, the light stored in the cavity decays with time as it is transmitted through the cavity mirrors and absorbed by gas phase molecules on every round-trip through the cavity. On every round-trip, which takes $2L_{cav}/c$ seconds, the intensity is reduced by R^2 due to two-fold reflection at the mirrors and by $\exp(-2\alpha L_{cav})$ due to absorption in the gas phase. Hence, the intracavity intensity and hence also the intensity at the PD decay exponentially as

$$I(t) = I_0 R^{tc/L_{cav}} \exp(-\alpha c t) \approx I_0 \exp\left(-tc \cdot \left[\frac{1-R}{L_{cav}} + \alpha\right]\right) = I_0 \exp\left(-\frac{t}{\tau}\right) \tag{2.31}$$

Herein, the time constant of the exponential decay τ (the average time a photon remains in the cavity), called ring-down time, was defined as $\tau^{-1} = \frac{c(1-R)}{L_{cav}} + c\alpha$, and I_0 denotes the intensity at $t = 0$. The approximate equal sign holds for R close to 1. If L_{cav} and R are known, the absorption coefficient α of the gas and hence the concentration of an absorbing species can be retrieved from a measurement of τ. To measure τ, the detector signal is recorded while the intensity decays (compare Figure 2.11) and the so obtained ring-down signal is fitted by an exponential function on a personal computer or other hardware (signal processors, FPGAs) to retrieve τ. To determine the reflective losses, the so called empty cavity ring-down time τ_0, defined as

$$\tau_0^{-1} := c\frac{1-R}{L_{cav}} \tag{2.32}$$

is recorded in a separate measurement, either by purging the cavity with a non-absorbing gas, by tuning the laser wavelength away from an absorption line or by scanning an absorption line and fitting of the line-profile including τ_0^{-1} as a constant offset.

Besides its simplicity, the most important advantages of CRDS are A) the possibility to directly determine absorption coefficients and hence molecular concentrations from ring-

down measurements without any calibration and B) the independence of measurements from I_0. The latter aspect is particularly important for high finesse cavities whose resonance linewidth is much narrower than the linewidth of most lasers, resulting in noisy transmission signals that are ill-suited for measuring small changes due to intracavity absorption. Since the ring-down time is, however, independent from I_0, measurements can be performed without the need for tight laser locking and a low-noise transmission signal.
A potential disadvantage of CRDS as compared to other techniques of CES is that the retrieval of τ from a large number of recorded ring-downs is often not performed in real-time, but in post-processing due to the necessary sampling rate of typically several MHz at a vertical resolution of ~ 16 bit and the resulting high computational bandwidth and power. Real-time analysis of the recorded signals hence requires specialized hardware. Although alternative techniques for determining τ from ring-down signals without fitting procedures exist, these techniques are not fully immune to intensity noise and/or suffer from other disadvantages [84].
It is also worth noting that the effective pathlength in CRDS, which is given by the average distance light travels through the cavity during a ring down, $\tau c = \frac{L_{cav}}{1-R}$, is a factor of two smaller than the effective pathlength in resonant CES techniques performed with the laser frequency fixed to a cavity resonance [85]. This can be understood as a consequence of the broader spectrum of light during a ring-down (Fourier limited by the ring-down time), which means that not all spectral components are on resonance and experience the same resonant enhancement.

3. Photoacoustic Spectroscopy

Photoacoustic spectroscopy (PAS) is an indirect spectroscopic technique. As outlined in section 1, the term "indirect optical spectroscopy" summarizes techniques that detect changes of physical properties of a sample upon interaction of light, rather than the effect of that interaction on light (direct spectroscopy). Absorption is the most widely employed light-matter interaction, especially in sensing applications. Indirect absorption spectroscopic signals are usually derived from changes in temperature and the associated variation of refractive index (photothermal spectroscopy) as well as from changes in pressure (PAS), although a number of other phenomena (*e.g.* photoconductivity, photocurrent, optogalvanic effect) are exploited as well. In the following chapters, the photoacoustic effect will be discussed in some detail in section 3.1. The experimental instrumentation for PAS as well as a specific kind of PAS used in chapter 6, quartz-enhanced PAS (QEPAS), will be introduced in sections 3.2 and 3.3. The properties of PAS and QEPAS relevant for trace gas sensing will be reviewed in section 3.4, with a focus on distinct differences to direct absorption spectroscopy (TLAS, 2*f*-WMS, compare section 1.3). Chapter 3 is concluded by a brief introduction to the state of the art in cavity enhanced PAS.

3.1. The Photoacoustic Effect – Formation of Photoacoustic Signals

In this chapter, the formation of photoacoustic signals will be discussed in three steps: A) absorption of a photon, B) relaxation of the excited molecule and release of kinetic energy (heat) and C) formation of pressure waves due to heating. This "photoacoustic signal chain" is summarized in Figure 3.1.

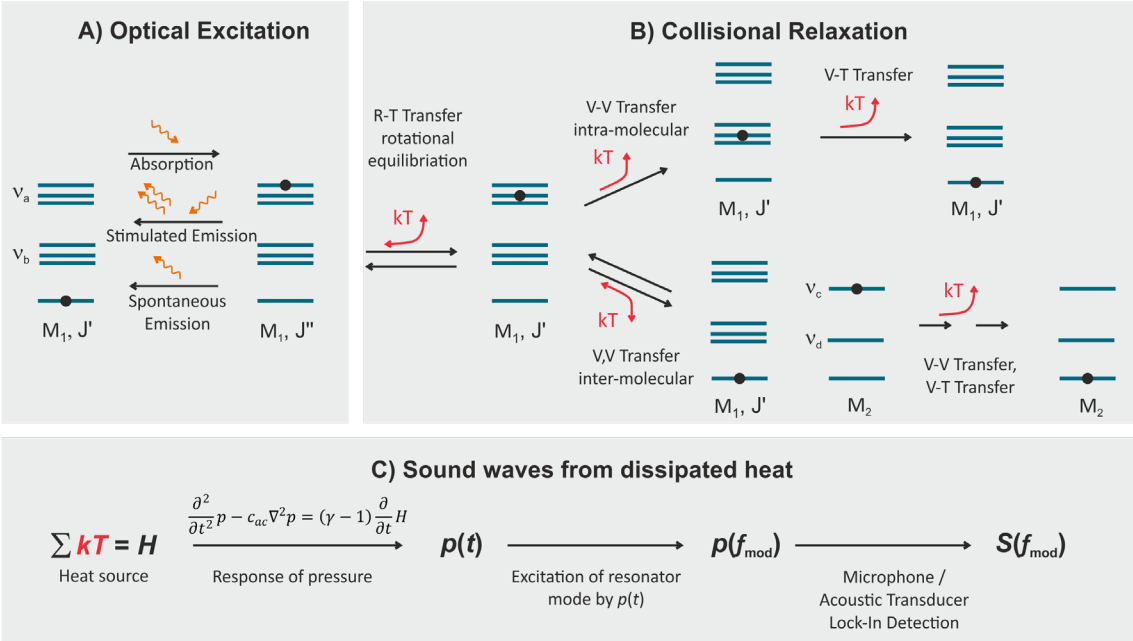

Figure 3.1. Summary of photoacoustic signal formation. M_i: molecule; ν_a, ν_b, ν_c, ν_d: vibrational quantum numbers; J: rotational quantum number; kT: kinetic energy

3.1.1. Absorption and Excitation Rates

Assuming excitation by a monochromatic laser of wavenumber $\tilde{\nu}$, the rate at which a single molecule is excited from state 1 to 2 via a dipole transition is given from the Einstein B coefficient B_{12} and the intensity I (optical power per unit area) as [86]

$$\gamma^{\uparrow}(\tilde{\nu}) = B_{12}\Gamma(\tilde{\nu})\frac{I}{c^2} = \frac{A_{21}}{8\pi h\tilde{\nu}^3}\frac{g_2}{g_1}\Gamma(\tilde{\nu})\frac{I}{c^2} \tag{3.1}$$

Herein, $\Gamma(\tilde{\nu})$ is the area normalized line-shape function (in m), h is Planck's constant, A_{21} is the Einstein A coefficient of the transition, g_i are the statistical weights (also called degeneracy) of the states (compare [87]) and c is the speed of light. The rate for the reverse process of a stimulated transition from 2 to 1 is also given by (3.1), except that $B_{21} = B_{12}\frac{g_1}{g_2}$ (stimulated emission). Since stimulated emission leads to relaxation of a molecule by releasing photons, rather than heat, it can be considered a competing pathway to the generation of photoacoustic signals. The same is true for the spontaneous emission of photons. For transitions in the infrared spectral region, spontaneous emission of light is a relatively slow process. The mean rate of spontaneous emission from state 2 to 1 is given by A_{21} and scales with the third power of the energy gap between the states [88]. For fundamental ro-vibrational transitions, typical values for A_{21} are ~ 1 s^{-1} to 200 s^{-1} [89]. The overall rate of relaxation via spontaneous emission is given by the sum $\sum_j A_{ij}$ over all final states j accessible from state i, *i.e.* all states for which transitions $i \rightarrow j$ are dipole-allowed [88]. The number of allowed transitions depends in a fairly complex way on the symmetry of the molecule as well as the vibration, but is generally below ~10 [13]. Therefore, the relaxation rate via spontaneous emission is typically below 1 kHz, which is much slower

than collision induced relaxation rates at (near-) ambient conditions (compare sections 3.1.2 and 5.2.1).

3.1.2. Release of Thermal Energy, Relaxation of Ro-Vibrationally Excited Gas-Phase Molecules

To excite photoacoustic signals, the absorbed photon-energy $hc\tilde{\nu}$ must be converted into heat H. Rather than releasing all their energy into heat in a single collision, most gas phase molecules undergo a series of energy transfers during which their internal energy (electronic, vibrational, rotational) is reduced, with the missing energy being converted into heat. Examples of such transfers are summarized in Figure 3.1. In the following, the different means of relaxation are discussed in the context of gas-phase infrared spectroscopy [90].

If a ro-vibrational transition is used for excitation, the absorbed photon-energy is stored in vibrational as well as rotational degrees of freedom of the molecule. The increased (R-branch transition) or decreased rotational energy (P-branch transition) is rapidly exchanged between molecules upon collisions. This results in the molecule quickly returning to its rotational thermal equilibrium by releasing (R-branch) or taking up (P-branch) kinetic energy (rotational-translational (R-T) transfer). Rotational relaxation is hence the first (small) source of heat and hence photoacoustic signals (compare Figure 3.1). From vibrational degrees of freedom (ν_i" in Figure 3.1), energy can be transferred to vibrational (V-V) and/or translational degrees of freedom (V-T) of the same molecule and/or the collision partner. These processes are typically much slower than R-T transfer. Rates $\gamma_{A-B}^{\parallel}$ for collisional energy transfer are calculated from collisional frequencies $Z_{A\text{-}B}$ per molecule A with molecules B derived from kinetic gas theory and the average number of collisions necessary for an inelastic collision, $\hat{Z}_{A\text{-}B}$.

$$\gamma_{A-B}^{\parallel} = \frac{Z_{A-B}}{\hat{Z}_{A-B}} \tag{3.2}$$

$Z_{A\text{-}B}$ is given by [91]

$$Z_{A-B} = 2N_B D_{A-B}\sqrt{\frac{2kT}{\pi\mu}} = \frac{2p_B}{kT} D_{A-B}\sqrt{\frac{2RT}{\pi\frac{M_A M_B}{M_A + M_B}}} \tag{3.3}$$

Herein, $N_B = p_B/kT$ is the number density of molecules B, $D_{A\text{-}B} = \pi(r_A + r_B)^2$ is the collision cross section, r_i is the kinetic radius of molecule i, k is the Boltzmann constant, T temperature, $\mu = \frac{k}{R} \cdot \frac{M_A M_B}{M_A + M_B}$ the reduced mass, p_B the partial pressure of B, R the gas constant and M the molar mass. As an example, for collisions of a CO molecule with N_2 and CO at 300 K, $D_{CO\text{-}N2} \sim 0.43$ nm^2 [92], yielding $Z_{CO\text{-}N2} = 7$ GHz atm^{-1}. Note that $Z_{CO\text{-}N2}$ is very similar to the full-width at half maximum of the pressure broadened CO absorption line of 0.117 cm^{-1} atm^{-1} = 3.5 GHz atm^{-1} [93], which nicely illustrates that the linewidth of ro-

vibrational transitions in gas molecules at near ambient pressure is limited by molecular collisions [94,95].

To estimate $\hat{Z}_{A\text{-}B}$, two theories and one hypothesis are most noteworthy: Ehrenfest's adiabatic hypothesis, Landau-Teller theory and Schwartz, Slawsky, Herzfeld – (SSH) theory. The interested reader is referred to [90,96] for an introduction to SSH theory. Ehrenfest's adiabatic hypothesis can be expressed as follows [97]: "*If a changing force acts on a quantized periodic motion, the process will be adiabatic if the change of force is small* [comment: compared to the forces that act in the periodic motion] *during a period of the motion, and non-adiabatic if the change is large during this time.*" This simple principle gives a rough qualitative feeling for the transition probability from the collision time and the period of a vibration. For CO at room temperature, the mean speed is 475 m s^{-1}. Assuming a "collisional corridor" of $3 \cdot 10^{-10}$ m, the collision time is $6.3 \cdot 10^{-13}$ s. The vibrational period corresponding to the vibration of CO at 2143 cm^{-1} is $1.6 \cdot 10^{-14}$ s. Hence, the collision time is 40 times longer than the vibrational period. In contrast, the period of a rotation of CO in the 8th excited state is approximately 10^{-12} s, slightly above the collision time. One finds experimentally that, for CO and all other molecules except simple hydrides, almost every collision leads to R-T transfer ($\hat{Z}_{CO\text{-}CO} = 2.8$ [98]), while $\hat{Z}_{CO\text{-}CO} = 3 \cdot 10^{9}$ for V-T transfer in pure CO [99].

Landau and Teller [100] derived a quantitative theory by treating the collision as a time dependent repulsive perturbation of the potential energy of the oscillator scaling exponential with the distance between the collision partners. The probability of energy transfer is assumed proportional to the square of the Fourier component of the perturbation at the resonance frequency of the oscillator or rotator. The resulting expression for $\hat{Z}_{A\text{-}B}$ is

$$\hat{Z}_{A\text{-}B} = \exp\left(3\sqrt[3]{\frac{2\pi^4 \mu c^2 \tilde{\nu}^2}{\zeta^2 kT}}\right). \tag{3.4}$$

Herein, $\tilde{\nu}$ is the oscillatory frequency (wavenumbers) corresponding to the energy $hc\tilde{\nu}$ to be transferred in the collision, c the vacuum speed of light, h the Planck's constant and ζ the decay constant of the exponential perturbation with intermolecular distance. The collision number increases exponentially with the energy $hc\tilde{\nu}$ to be transferred and $T^{-1/3}$. Landau – Teller theory strongly overestimates collision rates of very slowly relaxing gases ($\hat{Z}_{A\text{-}B} > 10^{7}$) as well as polar gases due to the importance of attractive forces between these molecules. Since, at room temperature, (3.4) yields $\hat{Z}_{A\text{-}B} > 10^{7}$ for the vibrational frequencies of most molecules, Landau-Teller theory works best at elevated temperatures. The influence of intermolecular attractive forces is illustrated by water. The bending (ν_2) mode of water relaxes to the ground-state in one out of four collisions at room temperature [101], while equation (3.4) would predict $\hat{Z}_{AB} = 1.8 \cdot 10^{11}$ for $\zeta = 5 \cdot 10^{10}$ m^{-1} [90]. Dispite this overestimation, Landau-Teller theory correctly predicts the scaling of $\hat{Z}_{A\text{-}B}$ with T and $\tilde{\nu}$ for apolar molecules.

The exponential scaling of $\hat{Z}_{A\text{-}B}$ with transferred energy favors relaxation along pathways of small energy gaps. For polyatomic molecules that possess more than one vibrational mode, the fastest relaxation pathway is realized by collision facilitated intramolecular V-V transfer to lower lying vibrational modes (ν_a'' to ν_b'' in Figure 3.1) accompanied by the release of kinetic energy. In these molecules, V-T transfer from the lowest lying vibrational mode determines the overall relaxation rate. V-V transfer can also occur intermolecularly. For example, V-V transfer from the excited vibrational mode of CO to the vibration of N_2 is the predominant relaxation pathway for CO in N_2 due to the small energy mismatch $hc\tilde{\nu}$ = 188 cm^{-1} of the vibrational modes of N_2 and CO (compare section 5.2). Note that, if the energy mismatch is on the order of kT, V-V transfer (inter- and intramolecular) can also occur from the lower-lying to higher-lying vibrational level (endothermic direction), as is the case for CO in N_2. Since endothermic V-V transfer requires uptake of thermal energy, it leads to cooling of the gas ("kinetic cooling effect" [102]). The ro-vibrational relaxation of CO in N_2 and H_2O is studied in detail in section 5.2.1.

3.1.3. Generation of Acoustic Waves

The release (and uptake) of kinetic energy upon vibrational and rotational relaxation is the source of thermal as well as acoustic waves. Thermal waves, as probed by various techniques of photothermal spectroscopy [103], such as Fabry-Pérot photothermal interferometry (ICAPS) [104,105], are strongly damped and have wavelengths one to two orders of magnitude smaller than acoustic waves [106]. The deposited heat $H(t,\boldsymbol{x})$, whose dimension is power per volume, also leads to an increase in pressure and consequently the formation of acoustic waves (here, $\boldsymbol{x}$ denotes spatial distribution). The change in pressure resulting from $H(t,\boldsymbol{x})$ can be described theoretically using the laws of energy conservation, momentum conservation and mass conservation, together with a thermodynamic equation of state [107]. A detailed theoretical discussion can be found in [108]. An excellent overview of the formation of photoacoustic signals in simple resonators, especially cylindrical resonators, was given by Miklós *et al.* [109]. Note that the pair of resonator tubes used in this work (compare section 5.3.2) can be considered as a single tube in the context of the following discussion due to the small spacing between the tubes. A discussion of photoacoustic signals as detected by a quartz tuning fork without resonator tubes was given by Wojcik *et al.* [110]. Here, the most important results of [109,110] for QEPAS experiments presented below will be summarized.

The wave equation for the formation of pressure waves in a response to $H(t,\boldsymbol{x})$ is [110,111]

$$\frac{\partial^2}{\partial t^2}p - c_{ac}\nabla^2 p = (\gamma - 1)\frac{\partial}{\partial t}H \tag{3.5}$$

Herein, c_{AC} is the speed of sound and $\gamma = \frac{c_p}{c_V}$ is the ratio of the specific heat capacities at constant pressure and constant volume. The factor γ - 1 represents the maximum possible efficiency for the conversion of heat H to acoustic power. For dry air as well as nitrogen at

ambient temperature, $\gamma = 1.4$. Note that γ is related to the adiabatic heat expansion coefficient ε as $\gamma = c_{ac}^2 \frac{\varepsilon}{c_p}$, which gives a more intuitive picture of the source term (right-hand side) of (3.5) in terms of a heat source and the resulting thermal expansion [112].

For the further discussion we assume sinusoidal excitation of the sample with angular frequency ω. As discussed above, kinetic energy is released in multiple steps of differing rates. Therefore, the temporal evolution of $H(t)$ does not resemble the sinusoidal modulation of excitation and the molecular relaxation process must be modeled in detail for a quantitative description (compare Figure 3.1 and section 5.2.1). In a simplified picture, relaxation is assumed fast such that $H(t)$ follows the sinusoidal excitation. In this case, the amplitude of H at the modulation frequency can be expressed as

$$\hat{H} = \alpha \cdot I_L. \tag{3.6}$$

Herein, I_L is the amplitude of modulated light intensity and α is the absorption coefficient of the gas. The spatial distribution of $\hat{H}(\boldsymbol{x})$ resembles that of I_L if heat diffusion can be neglected. In resonator tubes of diameter much smaller than the acoustic wavelength, as were employed in this work, the spatial distribution is irrelevant for the formation of photoacoustic signals [109]. Independent from the radial distribution of $\hat{H}$, the induced pressure amplitude inside the resonator tube is homogeneous over the cross section of the tube since the modulation frequency is much smaller than the inverse time c_{ac}/r_{res} the pressure wave takes to travel across the resonator tube's cross section. Assuming weak absorption, the intensity of the excitation beam does not change along the resonator length and the induced pressure amplitude is hence also homogeneous along the resonator length. In this case, the pressure amplitude induced by $\hat{H}$ is given by

$$p_0 = \frac{(\gamma-1)}{i\omega}\hat{H} = \frac{(\gamma-1)\alpha P}{i\omega D_{cr}}. \tag{3.7}$$

Herein, P is laser power and D_{cr} the cross section area of the resonator. Note that the imaginary unit i in the denominator of (3.7) represents a 90° phase shift between H and the acoustic wave.

While the pressure of amplitude p_0 induced by H is uniformly distributed inside the resonator, the acoustic modes have a non-uniform spatial distribution. For example, the fundamental longitudinal mode, which is typically used, has its antinode in the center of the resonator tube and nodes at the open ends of the tube. To analyze the coupling of the uniformly distributed p_0 to various acoustic modes of the resonator, the spatial overlap as well as the frequency matching between the resonator mode and the excitation p_0 must be considered. Assuming the modulation frequency coincides with the resonance frequency ω_N of an acoustic mode N of the resonator, the amplitude p_N of the acoustic mode that builds up in the resonator is given by

$$p_N = \frac{Q_N}{\omega_N} \cdot \frac{(\gamma-1)\alpha P}{D_{cr}} \cdot F_N = k_{cell} \cdot \alpha \cdot P. \tag{3.8}$$

Herein, Q_N is the quality factor of the mode and F_N is the normalized spatial overlap integral, which takes into account the imperfect spatial overlap between p_0 and the resonator mode. For the fundamental longitudinal mode of an open resonator tube of diameter much smaller than the acoustic wavelength and uniformly distributed p_0, $F_N \approx \frac{2}{\pi}$. Q_1 is typically in the range of 10 – 100 [113,114] for open cylindrical resonators. Since Q scales with the tube diameter and p_N scales inversely with the cross section D_{cr}, p_N effectively scales inversely with diameter [109]. The factors relating α and P_L with p_N are often summarized as "cell constant" k_{cell}. For example, inserting $Q_N = 20$, $\omega_N = 2\pi \cdot 15820\ \mathrm{s}^{-1}$, $\gamma = 1.4$ and $D_{cr} = 0.018\ \mathrm{cm}^2$ in (3.8) yields $k_{cell} = 2.8$ kPa cm W^{-1}, which is in fair agreement with experimentally found cell constants [115].

3.2. Instrumentation for Photoacoustic Gas Sensing

An excellent overview of photoacoustic gas sensing can be found, amongst others, in [116]. Here, a brief introduction to the practical implementation of PAS shall be given.

A general layout for photoacoustic gas sensing is shown in Figure 3.2. The sample gas flows through a gas cell that may also act as an acoustic resonator. The light used to excite photoacoustic signals can be provided by various sources, such as thermal emitters, LEDs and lasers emitting in the UV to THz spectral range. If broadband sources are used, the excitation wavelength must be selected via a filter or spectrometer to achieve selectivity for the target molecule. Photoacoustic signals can be excited using intensity- or wavelength modulation. In Figure 3.2, the intensity of the light source is modulated at a resonance frequency of the acoustic resonator using a chopper. The modulated light enters and exits the gas cell via transparent windows. A microphone is used to detect the sound waves excited via absorption of the modulated beam and the electronic signal from the microphone is demodulated at the excitation frequency or a higher harmonic of that frequency using a lock-in amplifier. The demodulated signal of the microphone scales linearly with the concentration of the absorbing molecules and can be used to retrieve the latter based on a beforehand performed calibration.

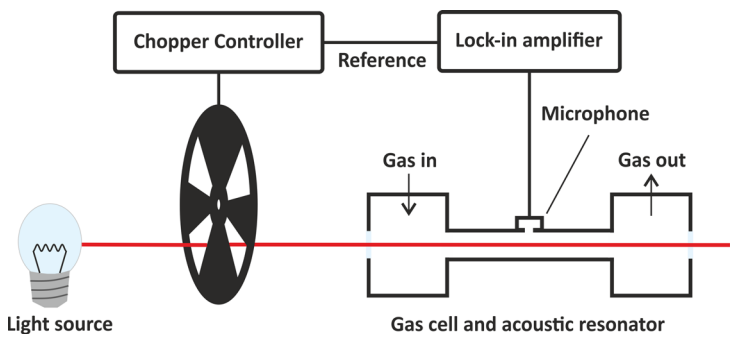

Figure 3.2. General experimental layout for photoacoustic spectroscopy

In principal, no photodetector is needed to perform photoacoustic gas sensing. However, photodetectors or power-meters can be used to reference photoacoustic signals to fluctuating power levels of the light source.

3.3. Quartz-Enhanced Photoacoustic Spectroscopy (QEPAS)

In 2002, Kosterev *et al.* established "Quartz-enhanced photoacoustic spectroscopy" (QEPAS) by replacing the microphone by a conventional quartz tuning fork (QTF), as used as the oscillator in commercial watches, to detect photoacoustic signals [117]. To this end, a laser beam was focused in between the prongs of a tuning fork (compare Figure 3.3). The photoacoustic pressure wave pushes and pulls the prongs and the resulting stress can be detected as a piezoelectric current analogous to the signal from a conventional microphone.

To improve the coupling of the photoacoustic pressure wave to the prongs of the tuning fork, two resonator tubes are positioned close (typically within ~ 100 µm) to the tuning fork. The tubes act as a single cylindrical resonator, as discussed in section 3.1.3 [113]. The length of the resonator tubes L must be chosen such that their resonance frequency coincides with that of the QTF. The combined tubes' resonance frequency is approximately given by

$$f_{res} \approx \frac{c_{ac}}{2L + 4\Delta L} \tag{3.9}$$

with $\Delta L = 8r_{res}/3\pi$ representing a correction of the tube length accounting for the effect of the open ends of the resonator [118]. For the standard QTF of $f_{res} = 32.78$ kHz, this yields an optimum length $L \approx 4.3$ mm for each tube. The diameter of the resonator tubes is usually chosen a little larger than the prong spacing and was experimentally found to be less critical for the overall sensing performance than L [113,119]. With optimized geometry of the resonator tubes, the signal to noise ratio of the QEPAS signal is typically improved by a factor of ~ 20 as compared to measurements without resonator tubes.

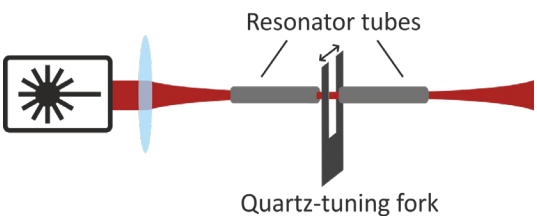

Figure 3.3. Left: Schematic of a QEPAS experiment.

The most significant differences between a conventional microphone and the QTF are [120]:

A) the well-defined electro-mechanical resonance of the tuning fork: The resonant bending vibration of the prongs of the QTF in the direction indicated in Figure 3.3 is very weakly damped, resulting in the high quality factor $Q = \frac{f_{mod}}{\Delta f_{\mathrm{FWHM}}}$ on the order of ~ 8000 at

atmospheric pressure. Therefore, the QTF is sensitive specifically to signals at the resonance frequency f_{mod}. Note that the quality factor of the mechanical vibration of the QTF is not to be confused with the quality factor of the acoustic resonator introduced in section 3.1.3. For standard QTFs used in watches, $f_{mod} = 2^{15}$ Hz = 32768 Hz. This is about an order of magnitude higher than the frequencies typically employed in standard PAS with microphones. While the acoustic noise floor typically decreases with frequency ($1/f$-characteristic), the higher frequency is larger than the relaxation rate of many molecules. Incomplete conversion of vibrational energy to kinetic energy during a period of modulation leads to smaller signals and hence reduced sensitivity. Also, incomplete relaxation at high modulation frequencies yields a larger influence of the gas matrix on photoacoustic signals due to the very different efficiencies for inelastic collisions with different molecules (compare section 5.2).

B) the reduced sensitivity to acoustic signals from distant sources: Since the wavelength of acoustic waves in the kHz range (~ 1 cm at 32.8 kHz) is much larger than the prong spacing (0.3 mm for the standard QTF), waves from sources far away from the tuning fork act on both prongs in the same way, pushing both of them left or right rather than apart from each other. This mode of vibration is piezoelectrically ineffective, yielding the increased robustness of QEPAS to external acoustic noise.

C) the very low cost of standard QTFs: As a mass product, standard QTFs are sold for a few cents. However, other components of a photoacoustic sensor, such as the excitation source (usually a laser), are often more expensive than a microphone and drive the overall cost.

In recent years, new QTFs with geometries optimized for QEPAS were designed and tested [121,122]. Amongst others, these tuning forks have lower resonance frequencies and larger prong spacings. The latter is important if light sources of poor beam quality are used or if the excitation wavelength is very large (THz). In both cases, the beam cannot be focused to the small gap between the prongs of 300 µm without partially hitting the prongs, which generates a large undesired background signal. Also, as will be discussed in section 5.3.1, an increased prong spacing allows placing the QTF inside high finesse cavities without causing additional cavity round-trip losses.

3.4. Advantages of PAS and QEPAS for Trace Gas Sensing

While PAS and QEPAS share the characteristics of spectroscopic gas sensing discussed in section 1 (fast response, non-destructive, no/minimal sample preparation, high specificity), they follow quite different trading rules than direct spectroscopic techniques such as TLAS (compare section 1.3) [116].

3.4.1. Advantages and Challenges

First, PAS signals do not scale with optical pathlength, but power. For the design of gas sensors this has the important consequence that, in order to achieve high sensitivity, it is not necessary or even useful to increase the pathlength and hence the sample volume. Therefore, the gas volume for PAS and other indirect spectroscopic techniques, such as photothermal spectroscopy, can be reduced below 2 cm^3 [105]. Large sample volumes on the order of a few liters, as found in most multi-pass cells, are an appropriate choice for many applications, such as environmental monitoring, where temporal resolution is not critical and the available amount of sample is not restricted. However, if gas concentrations change on second timescales, the exchange of large gas volumes by fresh sample limits the practical temporal resolution. This is particularly true if the available gas flux is limited. Also, the size and weight of multi-pass cells is undesirable or even excluding for some applications, such as measurements on drones. It should be noted, however, that the gas cell only accounts for less than half of the overall footprint of most setups.

Second, PAS signals have zero or very small background, *i.e.* no signal is detected in the absence of absorption. This is in strong contrast to direct techniques that are based on measuring small absorption induced changes of large intensities. The background has important consequences on the noise floor in direct and indirect spectroscopy. In an idealized picture where a direct absorption measurement is shot-noise limited, the noise floor $\Delta P \sim \sqrt{P}$ increases with the square root of the overall power P. The change in P due to absorption, αLP, scales directly with P, yielding an overall increase in $SNR \sim \sqrt{P}$. In practice, however, the shot-noise limit is hardly ever reached due to excess noise from the laser or drifting optical fringes. Since excess noise, *e.g.* from fringes, is often proportional to P, no overall increase in SNR with P is observed beyond the point where detector noise is negligible. For PAS, contributions to the noise floor were discussed, amongst others, in [123]. The main contributions are acceleration noise (mechanical vibrations coupling to the transducer), external acoustic noise, Brownian noise and electrical noise. All of these are independent from optical power P. Since the signal increases linearly with optical power, the SNR is directly proportional to P. A smaller increase with P is found only if the noise floor is dominated by small background signals arising from absorption in the windows of the PA cell or at the prongs of the tuning fork in QEPAS. The different scaling with P puts very different constraints on the used light sources. While TLAS mostly requires low noise sources, PAS and QEPAS can tolerate higher levels of laser power noise and mostly require high optical power.

A common disadvantage of indirect spectroscopic techniques such as PAS is that the absorption coefficient and hence molecular concentration is not measured directly and hence requires calibration. Since the “photoacoustic signal chain” involves a significant number of steps (compare sections 3.1 and 5.2.1), the slope of the calibration is further

influenced by various parameters, such as matrix composition including humidity, pressure and temperature. Hence, care must be taken to either keep the measurement conditions constant or to measure the relevant parameters and correct for their influences based on measurements and/or models established beforehand.

3.4.2. Sensitivity

Although ppm and ppb level sensitivities are routinely achieved, the detection limits of PAS are generally still higher than those of direct absorption spectroscopy, such as TLAS. Reported sensitivities of PAS, typically given as noise equivalent absorption coefficient (NNEA), normalized by the bandwidth of the measurement and inverse laser power, vary between different molecules and typically range from 10^{-8} cm^{-1} W $Hz^{-1/2}$ (CO, [124,125]) to 10^{-9} cm^{-1} W $Hz^{-1/2}$ (H_2O, C_2H_2, [120]). For laser powers of 20 mW to 100 mW, representing typical values for quantum cascade lasers (QCL) commonly employed in the mid-IR range, this corresponds to noise equivalent absorption coefficients (NEA) of 10^{-8} $cm^{-1}Hz^{-1/2}$ and above. Remarkably, since this NEA is achieved for optical pathlengths of only a few centimeters, the NEA corresponds to detectable fractional changes of laser power below 10^{-7} at one second integration time. On the contrary, the noise floor for direct absorption spectroscopic sensing is now $\sim 5 \cdot 10^{-6}$ fractional absorption in the mid-IR [20]. However, with the use of multipass absorption cells with optical pathlengths routinely exceeding 50 m, NEAs are below 10^{-9} $cm^{-1}Hz^{-1/2}$ [20,126]. Using different techniques of cavity enhanced spectroscopy, optical pathlengths exceeding 1000 m can be achieved, resulting in NEAs even below 10^{-10} cm^{-1} $Hz^{-1/2}$ [69,127,128]. To reach or exceed the sensitivity of TLAS with PAS while exploiting the advantages of PAS, various efforts are made to improve on existing setups or develop novel concepts of PAS, QEPAS and other indirect techniques [129]. To name a few examples, quartz tuning forks were optimized for QEPAS [121] and the design of PA cells was thoroughly investigated and optimized [115]. Excitation of PA signals with optical gratings moving at the speed of sound was investigated [112] and photothermal spectroscopy with balanced detection was studied as an alternative to PAS [105].

Due to the direct proportionality between the photoacoustic signal Y and optical power P, a straight forward way of increasing sensitivity is by enhancing P. Lasers of high average power are hence highly desirable for PAS, while the footprint of the optical setup should remain compact. High power QCLs are ideal sources with this respect and QEPAS with up to 1 W of CW optical power from a QCL was demonstrated [125]. Further power enhancement can be achieved by performing PAS inside laser resonators. Early demonstrations using high power, but bulky CO_2 gas lasers demonstrated LODs in the low ppt range and an NEA of $1.8 \cdot 10^{-10}$ cm^{-1} (integration time not given) at an intracavity power exceeding 100 W [130]. Due to their large size and limited wavelength tuning, gas lasers are, however, incompatible with most practical applications of PAS. Therefore,

photoacoustic measurements inside the cavity of external cavity (EC-) diode lasers or EC-QCLs appear more attractive and have shown an increase in sensitivity > 100 as compared to measurements outside the laser cavity [131,132].

3.5. Cavity Enhanced PAS

To achieve power enhancement and hence increased sensitivity, PAS has also been combined with high finesse optical cavities (compare section 2.2). With available mirrors exceeding a reflectivity of 0.999, power enhancements beyond 1000 appear feasible, given the mirror transmission is high and light can be coupled efficiently into the cavity (compare section 2.3). At near-IR wavelengths, PAS with a power enhancement of 630 was demonstrated [133]. In the mid-IR spectral range, QCLs were combined with PAS [134] as well as QEPAS [135] to achieve power enhancements of ~250, yielding a NEA < 10^{-9} cm^{-1} $Hz^{-1/2}$ [134]. Combining these sensitivity levels with the advantages of PAS, in particular the unique possibility to perform spectroscopy in volumes of a few cm^3 and below, holds promise to open up new applications for sensing with intracavity PAS. Along this line, sections 5.3 and 7 demonstrate novel developments of mid-IR intracavity QEPAS using a Brewster window cavity.

4. Faraday Rotation Spectroscopy

Faraday rotation refers to the rotation of the polarization of light in the presence of a magnetic field oriented parallel to the direction of propagation. Faraday rotation spectroscopy (FRS) can be used to measure the rotation of polarization caused by gaseous paramagnetic species in the vicinity of an optically active molecular transition and thereby retrieve the concentration of that species in the gas.

In the first section of this chapter, the physical principles of FRS will be briefly introduced. The instrumental realization of FRS will be discussed in section 4.2. Demonstrations of exploiting the pathlength enhancement of high finesse cavities for FRS are reviewed in section 4.3, focusing on the technique of cavity ring-down FRS that was investigated in this thesis (compare chapter 6). Finally, distinct features of FRS in the context of gas sensing are discussed.

4.1. Faraday Rotation and the Zeeman Effect [136]

When linearly polarized light passes through a dielectric paramagnetic medium in the presence of a magnetic field oriented parallel to the direction of propagation, the orientation of its polarization is rotated. This effect is referred to as the Faraday effect. The Faraday effect can be understood in terms of magnetic circular birefringence (MCB), as illustrated in Figure 4.1. The sum of a right-hand circularly polarized (RHCP) and a left-hand circularly polarized (LHCP) electromagnetic wave of equal amplitudes yields linear polarization (LP). The orientation of LP depends on the phase between RHCP and LHCP light. Hence, if the phase velocities for RHCP and LHCP in a medium differ from each other, the orientation changes as light passes through the medium.

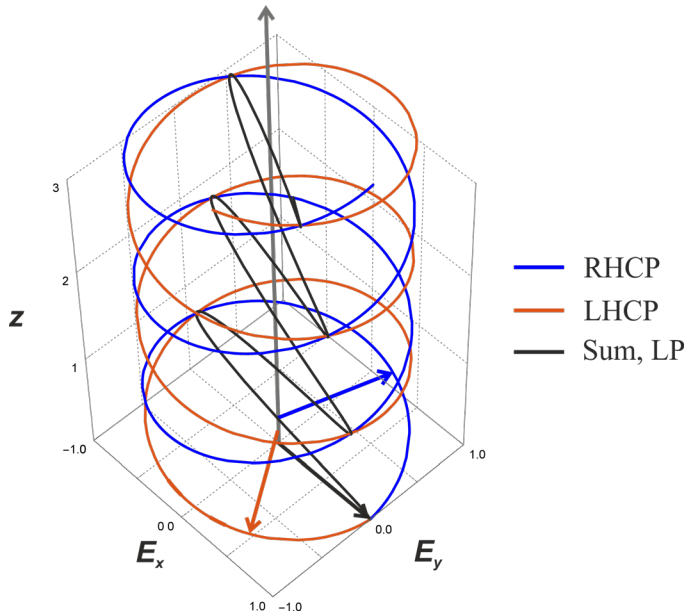

Figure 4.1. Circular birefringence leads to rotation of linearly polarized (LP) light. The electric field unity vector $\begin{pmatrix} E_x \\ E_y \end{pmatrix}$ of light is plotted along the direction of propagation z for right-hand circularly polarized (RHCP), left-hand circularly polarized (LHCP) as well as linearly polarized light. Different phase velocities of LHCP and RHCP (circular birefringence) yield a rotation of LP along z.

The physical origin of MCB in gases is the Zeeman effect. The Zeeman effect refers to the splitting of molecular states differing only in magnetic quantum number M, *i.e.* in the orientation of the total angular momentum J, in the presence of a static magnetic field (compare Figure 4.2). The additional energy $hc\tilde{\nu}_{Zeeman}$ of a state of magnetic quantum number M in the presence of a magnetic field is given by [137]

$$hc\tilde{\nu}_{Zeeman} = M \cdot g_m \cdot \mu_B \cdot B. \tag{4.1}$$

Herein, μ_B is the Bohr magneton, B is magnetic field strength and g_m is the so-called g-factor of the state, which gives the proportionality between total angular momentum and magnetic momentum of a particle. The splitting of energy levels of different M causes shifts in the resonance frequency of transitions involving changes in M. For RHCP, only transitions with ΔM = -1 are optically active, while for LHCP only $\Delta M = 1$ transitions are optically active [138]. As illustrated in Figure 4.2, this yields a shift of the resonance frequency of a transition for LHCP to lower frequencies, while RHCP is shifted to higher frequencies. Due to the dispersion profile associated with an optical transition (compare section 1.4), this yields different refractive indices for RHCP and LHCP, *i.e.* MCB. For the same reason, the Zeeman effect also causes magnetic circular dichroism (MCD), *i.e.* different absorption for LHCP and RHCP.

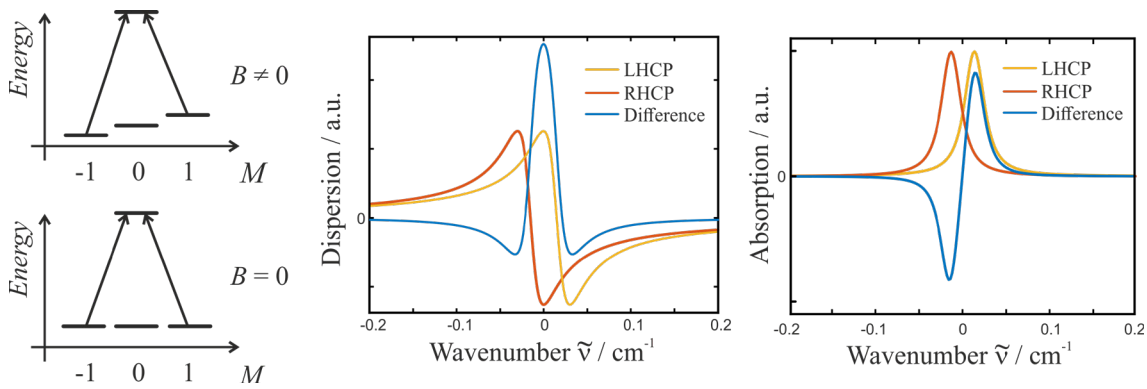

Figure 4.2. Following ref. [138]. Left: Energy levels for a transition from a state $J = 1$ to $J = 0$. In the absence of a magnetic field B, levels of different magnetic quantum number M are degenerate, while they are split if $B \neq 0$. Right: Simulated dispersion spectrum in the presence of magnetic circular birefringence. The dispersion profile is shifted towards higher and lower wavenumber, respectively, for LHCP and RHCP light. At the original resonance wavenumber, magnetic circular birefringence (difference between LHCP and RHCP) occurs.

The largest MCB from an isolated transition is found if the wavenumber shift is on the order of the half width at half maximum of the absorption line and hence strongly depends on pressure. This condition can be fulfilled by either changing the magnetic field strength B or pressure p [139]. It should be noted that the g-factor changes with angular momentum J [140]. Therefore, for ro-vibrational transitions in the P- and R-branch of a vibrational band, the optimum B changes between transitions due to the different values of J of the involved states.

The electronic ground state of most molecules is diamagnetic and shows virtually no Zeeman effect. Examples of paramagnetic molecules are O_2 (triplet), NO, NO_2 and other radicals. Due to their paramagnetic nature, these molecules exhibit a significant Zeeman effect at practically achievable magnetic field strengths of a few 100 Gauss (G), enabling their sensitive detection via FRS.

4.2. Instrumentation for FRS

A basic optical setup for FRS is illustrated in Figure 4.3. The linearly polarized beam from a laser passes through the gas and a second polarizer, called analyzer, before being detected at a photodetector. The gas cell is enclosed by a permanent magnet or solenoid to achieve a magnetic field strength of typically 100 G to 600 G.

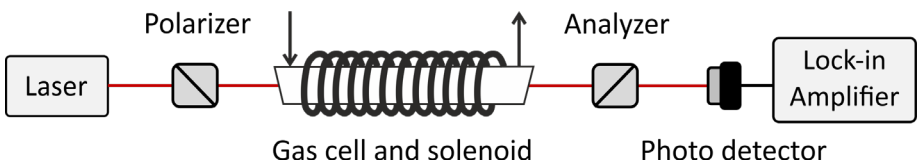

Figure 4.3. Schematic setup for Faraday rotation spectroscopy.

While permanent magnets offer the advantage of achieving large field strengths and dissipating no heat, solenoids allow modulating the magnetic field and adjusting the magnetic field strength for optimum signal to noise ratio [141,142]. The gas cell is manufactured from low permeability, non-conducting materials such as glass or polymer materials to avoid Eddy currents and to not reduce the field strength inside the gas volume. The analyzer is used to detect changes in polarization. The transmission T of the ideal analyzer for linearly polarized light is given by *Malus' law*,

$$T = \cos^2(\varphi). \tag{4.2}$$

Herein, φ is the angle between the plain of polarization and the polarizer axis. In one implementation, the analyzer transmission axis is rotated by 90° relative to the polarizer. Hence, light is only detected if polarization rotation occurs. However, the sensitivity $dT/d\varphi$ is smallest in this configuration and measurements are limited by detector noise. In a second implementation, the analyzer is oriented at 45°, yielding maximum sensitivity $dT/d\varphi$, but also significant background intensity at the detector. The high background intensity makes this configuration susceptible to laser power noise. Laser power noise can be efficiently suppressed by detecting light reflected and transmitted at the analyzer and subtracting the two signals (balanced detection) [141,143,144]. If balanced detection is performed, a Wollaston prism is preferentially used as an analyzer. In contrast to wire-grid or nanoparticle polarizers, Wollaston prisms deflect both orthogonal polarization states in a symmetric way, giving access to both polarization states with high extinction ratio. For optimum SNR without balanced detection, an optimum angle close to 90° is chosen where the laser power noise matches the detector noise [145].

As in direct absorption spectroscopy (compare section 1.3), wavelength modulation is often used to sensitively detect the magnetic rotation spectrum of the targeted transition. In addition to wavelength modulation, the magnetic field can be modulated via the driving current of a solenoid. Lock-in detection at the magnetic field modulation frequency efficiently eliminates any residual background signals that are not proportional to magnetic field [146]. However, electromagnetic interference from the modulated solenoid can give rise to significant background signals and noise [142]. Multi-pass cells can be used to increase the measurement sensitivity. However, since the beam pattern in multi-pass cells yields an increased volume, it is difficult to maintain the necessary field strength across the large diameter of the gas cell [147]. A drastic increase in optical pathlength without increased volume can be achieved by high finesse optical cavities (compare section 2.2). Cavity enhanced FRS will be discussed in the next section.

4.3. Cavity Ring-Down Faraday Rotation Spectroscopy [9]

High finesse optical cavities increase the effective optical pathlength by factors close to their finesse F, as compared to their physical length (compare section 2.2). With state-of-

the-art dielectric mirror coatings, F takes values of 10^3 to 10^5, yielding effective pathlengths of several kilometers. Cavity enhanced FRS can be realized by replacing the single pass gas cell in Figure 4.3 with an optical cavity (compare Figure 4.4). In principle, Faraday rotation can be detected in this configuration as described in section 4.2. However, due to the discrete resonances of the cavity, wavelength cannot be tuned continuously and wavelength modulation is hence not feasible (see also section 5.3.1). Therefore, magnetic field modulation was employed in previous publications [139,148]. Also, frequency locking techniques and/or balanced detection were employed to achieve a low-noise transmission signal through the cavity [144].

As discussed in section 2.6, the difficulty of achieving low-noise transmission signals in cavity enhanced absorption spectroscopy can be circumvented by means of cavity ring-down spectroscopy (CRDS). CRDS has also been combined with FRS [149] and the principles of cavity ring-down FRS (CRD-FRS) were introduced in detail in [150]. The key elements of a CRD-FR spectrometer are outlined in Figure 4.4 a. Linearly polarized light is transmitted through a high finesse optical cavity containing the sample gas subjected to a homogeneous magnetic field along the beam axis, here produced by a solenoid. A Wollaston prism oriented at 45° relative to the incoming polarization is used as the analyzer. Light of orthogonal linear polarization states is detected by two photodetectors (PD). An acousto-optic modulator (AOM) initiates ring-down events that are recorded separately for the two polarizations (Figure 4.4 b). As will be discussed below, Faraday rotation is detected from the different ring-down times of the two polarizations.

On every roundtrip during the ring-down event, a rotation of polarization by an angle Θ occurs. Hence, the polarization angle φ evolves during the ring-down as

$$\varphi(t) = \varphi_0 + \Theta \frac{ct}{2L_{cav}}. \tag{4.3}$$

where φ_0 is the initial polarization angle given by the angle between the polarizer and the analyzer, c is the speed of light and L_{cav} the cavity length.

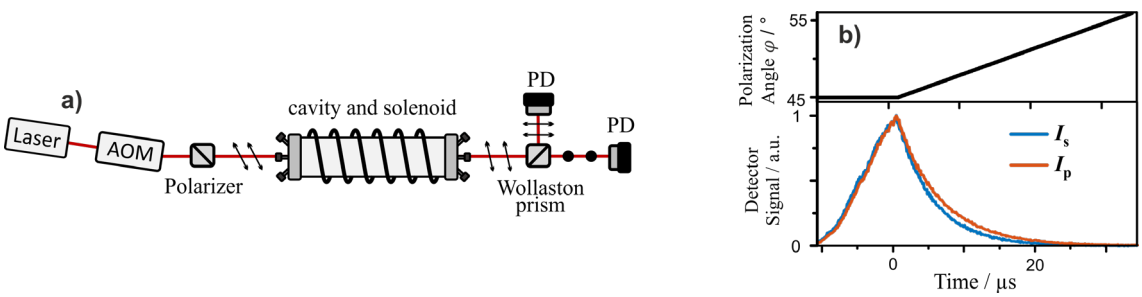

Figure 4.4. Principles of CRD-FRS, see text. a) experimental layout. AOM: acousto-optic modulator, PD: photodetector b) Intracavity polarization angle φ (Eq. (4.3)), calculated for $\Theta = 11$ µrad) and detector signals (measured for 1 $\%_V$ O_2 in N_2) during a ring-down event.

In general, MCD will additionally induce ellipticity on every round-trip, but at the resonance wavenumber of a transition, no MCD is observed (compare Figure 4.2). While the discussion is limited to this particular case in this work due to the frequency locked operation (compare section 6), it is shown in [150] that MCD contributes equally to the signals at the two detectors and hence cancels in the differential measurements.

The transmission of the Wollaston prism for the orthogonal polarizations, denoted *p*- and *s*-polarized in the following, is given by

$$T_p = \cos^2(\varphi)$$
$$T_s = \sin^2(\varphi) \tag{4.4}$$

It follows that the intensities I_p and I_s at the two detectors during a ring-down event can be written as

$$I_p = I_0 \exp\left(-\frac{t}{\tau}\right)\cos^2\left(\varphi_0 + \Theta\frac{\mathrm{ct}}{2L_{cav}}\right)$$
$$I_s = I_0 \exp\left(-\frac{t}{\tau}\right)\sin^2\left(\varphi_0 + \Theta\frac{\mathrm{ct}}{2L_{cav}}\right) \tag{4.5}$$

where I_0 is the initial power and τ is the ring-down time including all losses in the cavity. With $\varphi_0 = 45°$ and $\Theta\frac{ct}{2L_{cav}} \ll 1$, Equation (4.5) can be rewritten in a single exponential form

$$I_p = \frac{I_0}{2}\exp\left(-\frac{t}{\tau} - \Theta\frac{ct}{L_{cav}}\right)$$
$$I_s = \frac{I_0}{2}\exp\left(-\frac{t}{\tau} + \Theta\frac{ct}{L_{cav}}\right) \tag{4.6}$$

From the decay rates $\tau_p^{-1} = \tau^{-1} + \Theta\frac{c}{L_{cav}}$ and $\tau_s^{-1} = \tau^{-1} - \Theta\frac{c}{L_{cav}}$ obtained via least square fitting of the ring-down events, the absolute round trip polarization rotation, Θ, can be retrieved without knowledge of the empty cavity ring down time τ:

$$\Theta = \frac{L_{cav}}{2c}\left(\tau_p^{-1} - \tau_s^{-1}\right) \tag{4.7}$$

Hence, CRD-FRS allows retrieving the Faraday rotation angle Θ directly from the measurement of a single ring-down event for s- and p- polarized light, independent from laser power and buildup noise, and without a separate measurement of the empty cavity losses. Here, empty cavity losses include absorption from spectrally interfering diamagnetic species.

4.4. Advantages of FRS and CRD-FRS for Trace Gas Sensing

Due to the limited number of naturally occurring paramagnetic molecular species, experimental demonstrations of FRS are so far limited to O_2, NO, the OH and HO_2 radical and NO_2. For these molecules, however, FRS has several advantages over TLAS and other sensing methods.

4.4.1. General Advantages and Challenges

While the insensitivity to diamagnetic species prevents the application of FRS to sensing of diamagnetic molecules, it offers a considerable advantage for sensing of paramagnetic species. Spectrally interfering species, such as water, that may otherwise limit the sensitivity of a TLAS measurement, can be conveniently eliminated from FRS signals via differential measurements in a 45° configuration or magnetic field modulation [147]. In the same way, optical fringes that commonly limit the sensitivity in TLAS experiments can be suppressed [145,147]. The measurement of polarization using balanced detection also strongly suppresses laser power noise.

The challenges encountered in FRS spectroscopy vary between different experimental implementations. If solenoids are used, the significant power consumption and heat dissipation of the solenoid are clear disadvantages. However, solenoids allow magnetic field modulation and free adjustment of magnetic field strength. On the contrary, permanent magnets dissipate no power and achieve strong magnetic fields, but do not allow for field modulation. For both, solenoids and permanent magnets, using multi-pass cells commonly employed in TLAS for increasing pathlength and detection sensitivity is challenging due to the difficulty of maintaining a strong magnetic field over the cross section of a multi-pass cell. Further, the high number of reflections at non-zero angle of incidence leads to significant depolarization of the transmitted beam [151].

Cavity enhanced FRS overcomes this problem, but is instrumentally more complex. Intracavity Faraday modulation spectroscopy requires efficient frequency locking of the laser to the cavity to avoid excess buildup noise (compare section 2) [139] and relies on magnetic field modulation. On the contrary, CRD-FRS does not require stable transmission through the cavity. Also, no magnetic field modulation is required [150]. A particular strength of CRD-FRS arises from the measurement of polarization rotation via differential ring-down times. As shown in section 4.3, this results in the independence of measurements from the cavity losses (empty cavity ring-down time). As was shown in [150], this suppresses shot to shot fluctuation that can arise, *e.g.*, from mechanical vibrations. Also, long-term drifts of the cavity losses that often limit the useful averaging time in conventional CRDS have a smaller impact on CRD-FRS [150].

4.4.2. Sensitivity

The sensitivity reported for FRS compares favorably with TLAS. Generally, the sensitivity of FRS scales with pathlength, but also depends on magnetic field strength, pressure and the targeted transition [139]. Finding the optimum transition, field strength and pressure is hence critical. For NO measured in its fundamental vibrational band, a limit of detection (1 σ) of NEC = 0.53 ppb $Hz^{-1/2}$ was reported for a pathlength of only 45 cm [152]. This concentration corresponds to an absorption coefficient for the targeted transition of

NEA = $7 \cdot 10^{-8}$ $cm^{-1}Hz^{-1/2}$ and a fractional absorption of $3.1 \cdot 10^{-6}$ $Hz^{-1/2}$, comparing well with state-of-the-art TLAS instruments with multi-pass cells [20]. For O_2 measured in its weak A-band at 762 nm, an NEC of 0.6 ppm $Hz^{-1/2}$ was reported with a pathlength of 6.8 m, corresponding to NEA = $2.2 \cdot 10^{-10}$ cm^{-1} $Hz^{-1/2}$ and an outstandingly small fractional absorption of $1.5 \cdot 10^{-7}$ $Hz^{-1/2}$ [141]. FRS was also applied to detect extremely small concentrations of the OH radical in an atmospheric simulation chamber using a superconducting magnet [147]. Here, an NEC of 0.13 ppt $Hz^{-1/2}$ ($3.2 \cdot 10^{6}$ molecules cm^{-3} $Hz^{-1/2}$) was reported using a pathlength of 108 m in a multi-pass cell, corresponding to an NEA of $2.4 \cdot 10^{-11}$ cm^{-1} $Hz^{-1/2}$. For measurements of NO_2 and HO_2, the interested reader is referred to [142,153]. With cavity enhanced FRS, detection limits of 3.5 ppm $Hz^{-1/2}$ for O_2 [143] and 0.21 ppb $Hz^{-1/2}$ for NO [139] were reported.

5. Advances in QEPAS for Gas Sensing

Photoacoustic spectroscopy (PAS) and quartz-enhanced PAS (QEPAS) were intensely investigated for trace gas sensing, amongst others due to the small gas volume and footprint of instruments based on these techniques (compare section 3.4). To exploit the advantages of QEPAS in measurements of equal sensitivity as those achievable in long pathlength transmission measurements (compare section 3.4.2), possibilities of increasing the sensitivity of QEPAS using high optical excitation power were investigated. As was outlined in section 3.5, the excitation power can be strongly increased by exploiting the resonant power buildup in high finesse cavities. In recent years, efforts towards enhanced sensitivity hence lead to demonstrations of QEPAS performed inside a high finesse optical cavity (intracavity QEPAS, I-QEPAS) [135,154]. I-QEPAS, as compared to conventional PAS in high finesse cavities (compare section 3.5), however, comes with some additional difficulties, in particular due to the small prong spacing of only 300 µm that requires a very small beam waist of the cavity mode.

In this chapter, mid-IR QEPAS measurements with a prototype of a now commercially available QEPAS module based on a tuning fork with increased prong spacing of 1.5 mm are presented. Before demonstrating I-QEPAS with this module, measurements on CO without cavity enhancement using 2*f*-wavelength modulation are presented in section 5.1. The proportionality between the QEPAS signal and optical power as well as molecular concentration of CO are confirmed as predicted from theory (compare chapter 3). A peculiar trend of QEPAS signals with humidity is found, showing a decrease of signal amplitude with increasing humidity, which seems to directly contradict the established picture of water as a promotor for V-T relaxation. The finding is explained quantitatively in section 5.2 by kinetic cooling based on a detailed kinetic model of the processes involved in relaxation of CO in N_2 and H_2O. The following section 5.3 is concerned with cavity enhanced I-QEPAS in a Brewster window cavity exploiting optical feedback locking for

efficient intracavity buildup of optical power. Section 5.3.1 gives a discussion on design aspects that ultimately lead to the experimentally realized I-QEPAS setup presented in section 5.3.2. The following sections 5.3.3 to 5.3.5 present a series of measurements of ambient air as well as synthetic samples containing CO. Throughout these measurements, the high intracavity intensity of up to 73 Wmm^{-2} lead to strong optical saturation of CO. Saturation in QEPAS signals is discussed theoretically and saturation intensities for the R9 transition of CO at varying pressure are retrieved from QEPAS – as well as CRD experiments and compared to calculated saturation intensities. The effect of optical saturation on an I-QEPAS calibration of CO is compensated for, yielding a linear calibration. The performance of the I-QEPAS setup for CO sensing is quantified in section 5.3.6 and some concluding remarks on the presented I-QEPAS measurements are given in section 5.3.7.
Parts of the work presented in this chapter were published in [10,11].

5.1. *2f* - Wavelength Modulation QEPAS

To verify the correct operation of the QEPAS detection module prior to its use inside a high finesse cavity (compare section 5.3), 2*f*-wavelength modulation (2*f*-WM) QEPAS measurements of CO in N_2 were performed. Since the same QEPAS detection module was used and experimental conditions were chosen as similar as possible, the results and limits of detection can be directly compared with those of intracavity QEPAS (I-QEPAS) to retrieve the gain in sensitivity of I-QEPAS.

5.1.1. Setup

The experimental setup for 2*f*-WM-QEPAS is illustrated in Figure 5.1. A distributed feedback quantum cascade laser (DFB-QCL, *Adtech Optics*) emitted 45 mW of optical power in continuous wave operation at a wavenumber of 2179.77 cm^{-1}. The laser wavenumber was sinusoidally modulated at half the QTF resonance frequency f_{QTF} via a small amplitude current modulation. The laser current was modulated by applying a sinusoidal voltage signal to the analog control input of the laser current driver (QCL OEM300, *Wavelength electronics*). The modulation amplitude was adjusted for maximum QEPAS signal for every measurement.
The beam was focused to a spot size ($1/e^2$ radius) of 0.23 mm and directed through the resonator tubes and QTF. The optical power at the tuning fork was 25 mW due to losses at additional optical elements used for I-QEPAS experiments (not shown, compare Figure 5.10). Although these optical elements were necessary only for I-QEPAS (compare section 5.3), they were left in place for convenience. After the QEPAS detection module, the beam passed a reference gas cell filled with CO diluted in N_2 at 100 mbar and was finally detected on a mercury-cadmium-telluride (MCT) photodetector (PCI-2TE-12, *Vigo Systems S.A.*).

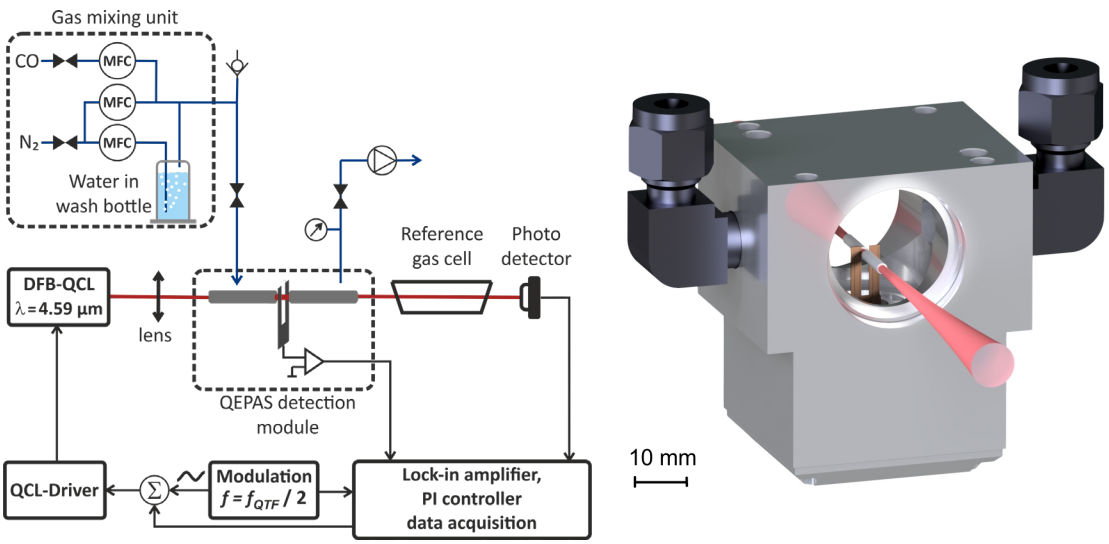

Figure 5.1. Left: Setup for 2*f*-WM-QEPAS of CO in N_2. MFC: mass flow controller; f_{QTF}: resonance frequency of the quartz tuning fork, ⊹: check valve, ⊘: pressure gauge, ⧗: needle valve, ▷: membrane vacuum pump. Right: Rendered image of the QEPAS detection module provided by *Thorlabs*.

The reference gas cell was used to lock the laser wavelength to the resonance wavelength of CO using wavelength modulation locking. To this end, the detector signal was demodulated at the third harmonic of the laser modulation frequency using a lock-in amplifier (ZI-MFLI, *Zurich Instruments*). The so obtained error signal was used as the input of a digital PI-controller (Digilock 110, *Toptica Photonics*) whose output was applied to the control input of the laser current driver. By adjusting the laser current, the laser wavelength was locked to the absorption peak.

All measurements presented hereafter were performed in a steady gas flow. A custom built gas mixing unit [14] was used to prepare samples of defined CO concentration and humidity. Defined flow rates of N_2 and CO test gas (100 ppm in N_2, *Air Liquide*) were set using mass flow controllers (MFC, compare Figure 5.1). One stream of nitrogen was humidified using a wash bottle filled with water. To keep the humidity constant, the temperature of the wash bottle was stabilized at 22 °C in a water bath thermostat [155]. Using three MFCs, the humidity and CO concentration could be set independently. The streams of humid and dry N_2 as well as CO test gas were combined. The humidity of the mixed gas was measured using a thermo-hygrometer (*Testo,* 635). A fraction of the mixed gas stream was pumped through the gas cell of the acoustic detection module via a membrane vacuum pump down-stream the gas cell. A pressure gauge and needle valves before and after the gas cell were used to manually adjust the pressure to the desired value. Since only a part of the gas stream was pumped through the gas cell, a check valve was inserted between the MFCs and the gas cell to provide a drain for the remaining gas stream. The overall flow rate was set to 1500 sccm at the MFCs, of which approximately 300 sccm were pumped through the gas cell.

The QTF was a custom design for QEPAS with a resonance frequency of 15.82 kHz and a prong spacing of 1.5 mm (see [122], design S15). It was kindly provided by *Thorlabs GmbH* in a ready-to-use module including electronic trans-impedance amplification and excitation circuitry that was a prototype of a now commercially available QEPAS module (*Thorlabs* ADM01, compare Figure 5.1). The amplified signal from the QTF was demodulated at the second harmonic of the modulation frequency using the lock-in amplifier, yielding the 2*f*-WM-QEPAS signal. The resonance frequency f_{QTF} and quality factor Q of the tuning fork were determined by exciting the tuning fork via application of a sinusoidal voltage signal of varying frequency to the electrodes of the QTF. The sweeping tool of the lock-in amplifier was used to generate the excitation signal and to ramp the frequency of the signal stepwise with a holding time of a few seconds per step while recording the 2*f*-WM-QEPAS signal. An example of the response of the QTF to swept frequency excitation is shown in Figure 5.2 (left). The quality factor of the QTF was recorded at varying pressure and the results are also shown in Figure 5.2 (right).

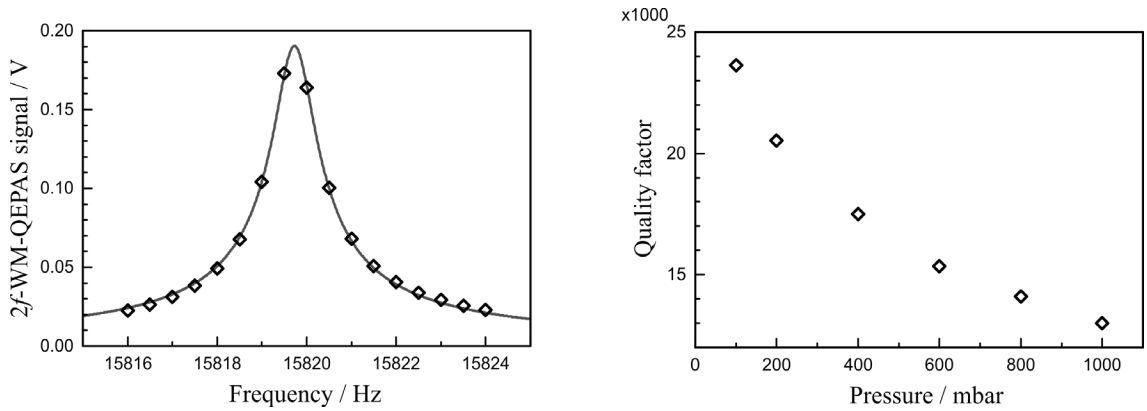

Figure 5.2. Left: Exemplary excitation sweep of the QTF at 500 mbar (data-points) and Lorentzian fit. Right: Quality factor measured at varying gas pressure.

Two 12.45 mm long stainless steel resonator tubes of 1.5 mm inner diameter were used as an acoustic resonator as received with the acoustic detection module. These resonator tubes yielded a QEPAS signal-to-noise (SNR) enhancement by a factor of six as compared to the bare tuning fork (compare Figure 5.3). This gain is significantly smaller than the values of ~ 25 typically reported in literature [113,124]. Unfortunately, this circumstance was realized in the course of this work only after the I-QEPAS measurements presented in section 5.3 had been finished. Measurements with resonator tubes of optimized length $L = 9.5$ mm showed an SNR 30 times higher than that of a measurement without resonator tubes.

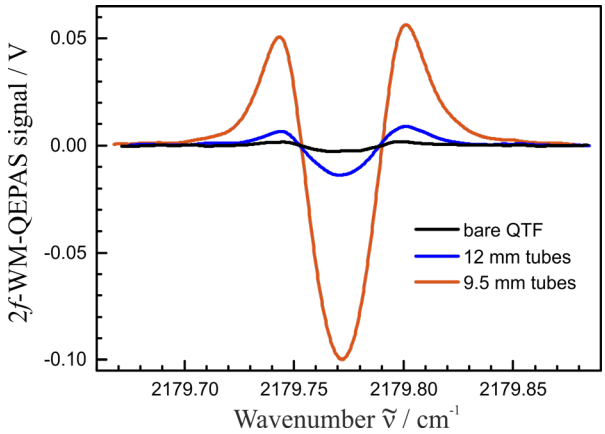

Figure 5.3. 2*f*-WM-QEPAS spectrum of 20 ppm CO in N_2 and 1.7 $\%_V$ H_2O recorded without resonator tubes and with resonator tubes of equal inner diameter (1.5 mm), but different length.

5.1.2. Scaling of QEPAS Signals with Optical Power, Concentration and Relative Humidity

To confirm the expected scaling of QEPAS signals with optical power (compare Equation (3.8)), measurements of 20 ppm CO in N_2 and 1.7 $\%_V$ H_2O at 500 mbar were performed. Measurements were performed with the laser wavelength locked to the peak of the R9 transition of CO. The optical power was adjusted via an iris aperture in the beam path and measured using a laser power meter. The recorded 2*f*-WM-QEPAS amplitude is shown in Figure 5.4 (left), together with a linear fit.

Figure 5.4 (right) shows the result of a calibration of CO in N_2 and 1.7 $\%_V$ H_2O at 500 mbar in the range from 2 ppm to 20 ppm. Measurements were again performed with the laser wavelength locked to the absorption line and the QEPAS signal recorded over 30 s was averaged for each concentration.

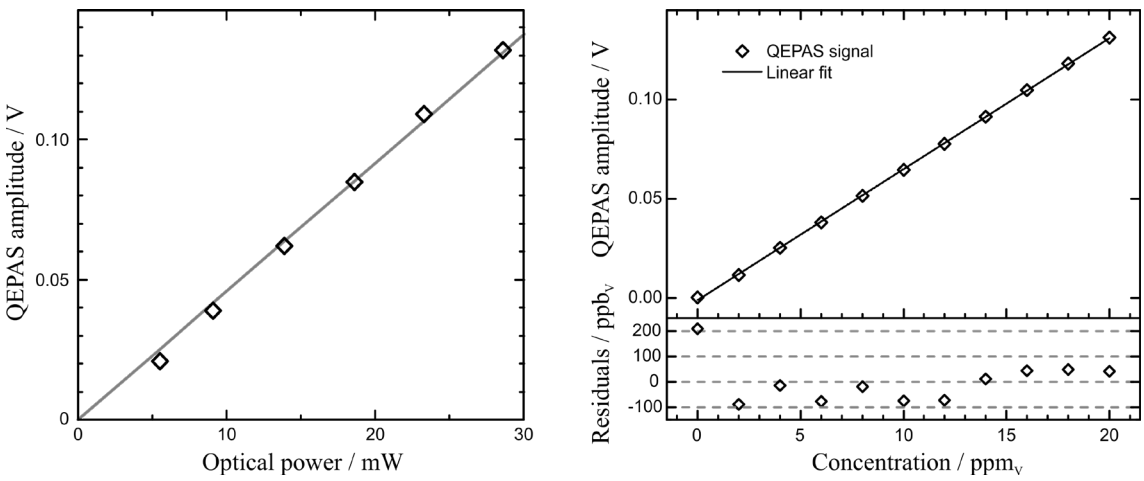

Figure 5.4. Left: 2*f*-WM-QEPAS amplitude measured for 20 ppm CO in N_2 and 1.7 $\%_V$ H_2O at 500 mbar recorded at varying laser power (data-points) and linear fit. Right: Calibration of CO in N_2 and 1.7 $\%_V$ H_2O at 500 mbar.

Except for the data point at 0 ppm, the residuals of the linear fit are all below 0.1 ppm, demonstrating excellent linearity of 2*f*-WM-QEPAS signal with CO concentration. The larger residual at 0 ppm may originate from residual CO in the gas cell due to insufficient purging.

Finally, the influence of humidity on the recorded 2*f*-WM-QEPAS signals was investigated. The amplitude and phase of the QEPAS signal from 23 ppm CO in N_2 at 500 mbar recorded for 0.04 $\%_V$ to 2 $\%_V$ H_2O is shown in Figure 5.5. To understand the peculiar decrease of the amplitude with increasing humidity observed at low water concentrations, a detailed kinetic model for the relaxation mechanisms of CO in N_2 and H_2O is introduced in section 5.2 that gives a quantitative explanation of the trend observed in Figure 5.5.

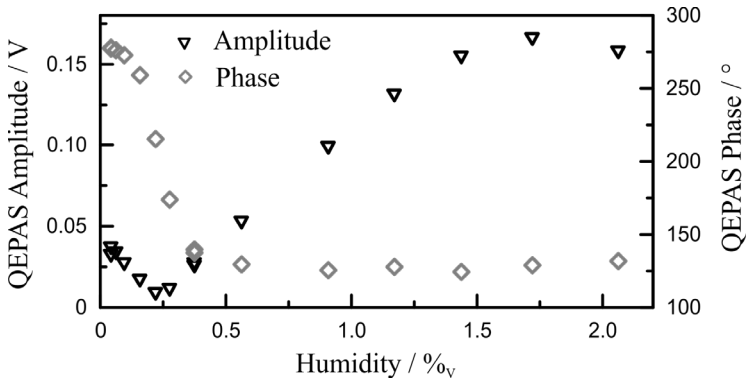

Figure 5.5. Influence of humidity on the QEPAS signal from CO.

5.2. Humidity Dependence of Photoacoustic Spectroscopy of CO in N_2 Explained via Kinetic Cooling

Water is well known to play a key role in photoacoustic sensing of many molecules. Water is an efficient quencher, converting vibrational energy of a molecule into heat much more efficiently and rapidly than other molecules, such as N_2 or O_2, typically making up the matrix of the target molecule [156]. Besides the lower energy of the lowest lying vibrational mode (compare section 3.1.2), this is mostly due to the high polarity of water and the resulting attractive forces that take effect in molecular collisions [90]. Therefore, signals usually increase with water concentration, especially in QEPAS where modulation frequencies are approximately one order of magnitude higher than in conventional PAS and fast relaxation is accordingly more important. For mid-IR QEPAS of CO, this trend was confirmed, however only for water concentrations above ~ 0.3 $\%_V$ [125,157]. For smaller concentrations, the QEPAS signal decreases with increasing humidity and shows a pronounced minimum at ~ 0.25 $\%_V$. Figure 5.5 shows the amplitude and phase of the QEPAS signal of 23 ppm CO in N_2 at 500 mbar for varying humidity. Despite the lower resonance frequency of 15.82 kHz, the QEPAS signal shows the same trend as in QEPAS measurements reported in [125,157] with a resonance frequency of 32.77 kHz. The

pronounced minimum at a water concentration of 0.25 $\%_V$ is accompanied by a change in phase from 278° to 125°.

While this trend was observed previously, a quantitative explanation is yet pending. Truong *et al.* observed that the photoacoustic signals from CO in N_2 were in anti-phase with those from H_2O in N_2 and explained this by kinetic cooling during V-V transfer from CO to N_2 [158]. Here, the kinetic model underlying this effect will be reviewed and applied to explain the observed trend of QEPAS signals from CO in N_2 and H_2O.

5.2.1. Kinetic Model for Relaxation of CO in N_2 and H_2O

To describe the observed trend of the photoacoustic signal with H_2O concentration, the heat $H(t)$ (in W m^{-3}) released upon relaxation of CO is modeled (compare section 3.1). To this end, the rates for all energy transfer steps from one molecular species to another will be derived based on collision frequencies and collision numbers obtained from literature. Multiplying the rate for a single molecule by the number density N of that species and the energy transferred in the process yields the contribution of this energy transfer step to $H(t)$. The processes involved in excitation and relaxation of CO in N_2 and H_2O are summarized in Figure 5.6. The number density N_{CO^*} of CO molecules in the excited vibrational state changes along a coherent pathway (absorption and stimulated emission), described by $\dot{N}^{\uparrow}_{CO^*}$, and a non-coherent pathway (inelastic collisions), described by $\dot{N}^{\parallel}_{CO^*}$. Spontaneous emission is neglected (compare section 3.1.1).

The net rate of optical excitation, including stimulated emission, is

$$\dot{N}^{\uparrow}_{CO^*} = \gamma^{\uparrow} \cdot \left(N^1_{CO} - \frac{g_2}{g_1} N^2_{CO^*} \right) \tag{5.1}$$

Herein, $\gamma^{\uparrow}$ is given by equation (3.1) and g_2 and g_1 are the statistical weights of the upper and lower state, respectively, of the ro-vibrational transition targeted by the laser. N^1_{CO} denotes a subset of the CO population that is in the lower state of the targeted transition and can hence be excited by the laser. For the R9 transition targeted here, the lower state has a total angular momentum J = 9 [87]. Accordingly, $N^2_{CO^*}$ is a subset of the vibrationally excited population of J = 10 (here, upper-case 2 denotes the excited state 2). Assuming the pressure is in the range between ~ 1 mbar and 1 bar and temperature T is around ambient, collision induced repopulation of the targeted rotational level (here $J = 9$) is fast and N^1_{CO} is not selectively depleted by laser excitation but in rotational thermal equilibrium at any time (compare section 3.1.2). For the same reason, $N^2_{CO^*}$ is not selectively populated.

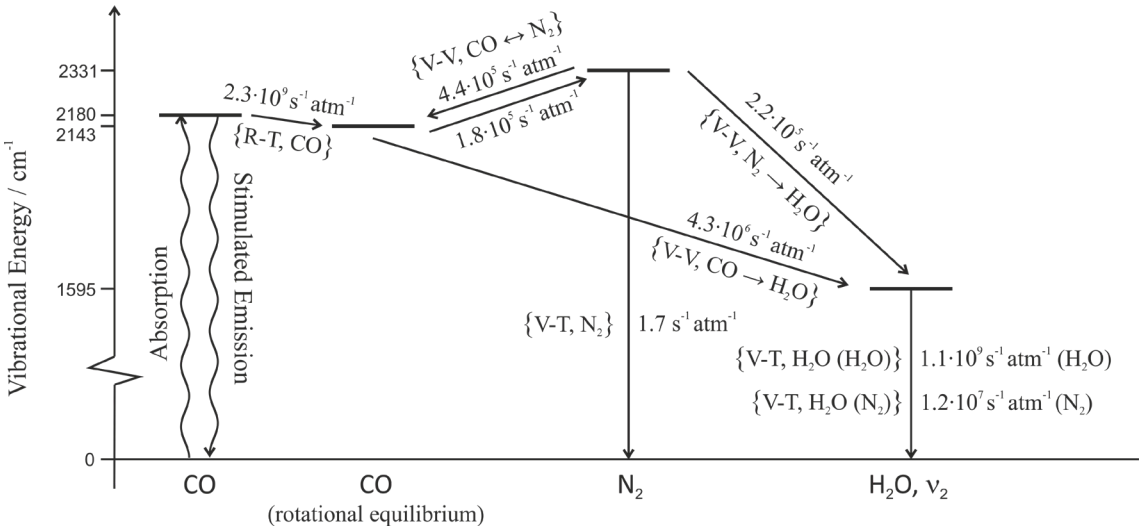

Figure 5.6. Collisional energy transfer between laser excited CO and N_2 and H_2O. Staight arrows indicate energy transfer in collisions and the kind of transfer is given in braces. The rates $Z_{A-B}/\hat{Z}_{A-B}$ for each energy transfer, normalized to the partial pressure of the collision partner, is also given for $T = 298$ K. For H_2O, rates are given for collisions with H_2O and N_2. See also Table 1.

At thermal equilibrium and without significant population of the excited vibrational state, N_{CO}^1 is given by

$$N_{CO}^1 = N_{CO}\frac{g_1}{G}\exp\left(-\frac{\mathcal{E}_1}{kT}\right) = \frac{p_{CO}}{kT}\frac{g_1}{G}\exp\left(-\frac{hc\mathcal{B}J^2}{kT}\right) \tag{5.2}$$

Herein, G is the total internal partition sum of CO at temperature T ($G_{CO,296\,\mathrm{K}} = 107.2$ [159]), $\mathcal{B} = \frac{h}{8\pi^2 c\mu r_{C-O}^2}$ is the rotational constant ($\mathcal{B} = 1.9$ cm^{-1} for $^{12}C^{16}O$) and $r_{C\text{-}O}$ is the distance between C and O in CO. The relevant constants of the R9 transition of CO for calculating $\gamma^{\uparrow}$ in equation (5.1) using equation (3.1) are $A_{21} = 17.91$ s^{-1}, $g_2 = 21$ and $g_1 = 19$ (values taken from the HITRAN2016 database [15]). At resonance ($\tilde{\nu}_0 = 2179.77$ cm^{-1}) and within the pressure broadened regime, $\Gamma_0 = 0.0549\ \mathrm{m^{-1}atm^{-1}}$ [93].

The non-coherent processes involved in the relaxation of CO are R-T, V-V and V-T transfer (compare Table 1). The collision numbers $\hat{Z}_{A-B}$ for the involved collisional energy transfers are defined as the average number of collisions necessary for a single transfer to occur (compare section 3.1.2). The fastest transfer involved is R-T transfer from the rotational level J = 10 that leads to the rapid establishment of rotational thermal equilibrium within the excited vibrational state. The same is true for the vibrational ground state for which the rotational energy level J = 9 is rapidly repopulated. The net kinetic energy released in R-T transfer is just the difference between the excitation wavenumber (2179.77 cm^{-1}) and the wavenumber of the vibrational mode (2143 cm^{-1}).

Table 1. Summary of processes involved in relaxation of CO. Collision frequencies $Z_{A\text{-}B}$ are given per molecule A and normalized to the partial pressure of the collision partner B. R-T, A (B) and V-T, A (B) denotes R-T and V-T relaxation of A in collisions with B. V-V, A → B denotes V-V transfer from A to B. $\Delta\mathcal{E}$ denotes the energy released in the process (negative for energy uptake) and the collision number $\hat{Z}$ denotes the average number of collisions necessary for one inelastic collision to occur (obtained from Ref. [90,101,160–162]). All values given for T = 298 K.

Process	$Z_{A\text{-}B}$ [10^9 $s^{-1}atm^{-1}$]	$\hat{Z}$	$Z_{A\text{-}B}/\hat{Z}$ [$s^{-1}atm^{-1}$]	$\Delta\mathcal{E}$ [cm^{-1}]
R-T, CO (N_2)	7.0	3	$2.3 \cdot 10^9$	37
V-V, CO → N_2	7.0	$4.0 \cdot 10^4$	$1.8 \cdot 10^5$	-188
V-V, N_2 → CO	7.0	$1.6 \cdot 10^4$	$4.4 \cdot 10^5$	188
V-V, CO → H_2O	6.0	$1.4 \cdot 10^3$	$4.3 \cdot 10^6$	548
V-V, N_2 → H_2O	5.7	$2.6 \cdot 10^4$	$2.2 \cdot 10^5$	736
V-T, N_2 (N_2)	6.8	$4 \cdot 10^9$	1.7	2331
V-T, H_2O (N_2)	5.7	$4.7 \cdot 10^2$	$1.2 \cdot 10^7$	1595
V-T, H_2O (H_2O)	4.5	4	$1.1 \cdot 10^9$	1595

V-V transfer occurs between CO and N_2 (bidirectional), from CO to H_2O and from N_2 to H_2O. Due to the fast depopulation of ν_2 of H_2O via V-T relaxation, V-V transfer to H_2O is considered unidirectional. V-T relaxation of CO is neglected due to the much faster V-V transfer to N_2 as well as H_2O. The kinetic rates are given by

$$\begin{aligned}
\dot{N}^{\parallel}_{CO^*} &= \dot{N}^{V-V}_{CO-N_2} + \dot{N}^{V-V}_{CO-H_2O} \\
\dot{N}^{V-V}_{CO-N_2} &= -N_{CO^*}\frac{Z_{CO-N_2}}{\hat{Z}_{CO-N_2}} + N_{N_2^*}\frac{Z_{N_2-CO}}{\hat{Z}_{N_2-CO}} \\
\dot{N}^{V-V}_{CO-H_2O} &= -N_{CO^*}\frac{Z_{CO-H_2O}}{\hat{Z}_{CO-H_2O}}
\end{aligned} \tag{5.3}$$

$$\begin{aligned}
\dot{N}_{N_2^*} &= \dot{N}^{V-V}_{N_2-H_2O} - \dot{N}^{V-V}_{CO-N_2} + \dot{N}^{V-T}_{N_2^*} \\
\dot{N}^{V-V}_{N_2-H_2O} &= -N_{N_2^*}\frac{Z_{N_2-H_2O}}{\hat{Z}_{N_2-H_2O}} \\
\dot{N}^{V-T}_{N_2^*} &= -N_{N_2^*}\frac{Z_{N_2-N_2}}{\hat{Z}_{N_2-N_2}}
\end{aligned} \tag{5.4}$$

$$\begin{aligned}
\dot{N}_{H_2O^*} &= -\dot{N}^{V-V}_{CO-H_2O} - \dot{N}^{V-V}_{N_2-H_2O} + \dot{N}^{V-T}_{H_2O^*} \\
\dot{N}^{V-T}_{H_2O^*} &= -N_{H_2O^*}\left(\frac{Z_{H_2O-N_2}}{\hat{Z}_{H_2O-N_2}} + \frac{Z_{H_2O-H_2O}}{\hat{Z}_{H_2O-H_2O}}\right)
\end{aligned} \tag{5.5}$$

The collision rates $Z_{A\text{-}B}$ are given by equation (3.3) with the kinetic radii $r_{H_2O} = 132\ \mathrm{pm}$, $r_{N_2} = 182\ \mathrm{pm}$ and $r_{CO} = 188\ \mathrm{pm}$ and molar masses $M_{CO} = M_{N_2} = 0.028\ \mathrm{kg\,mol^{-1}}$ and $M_{H_2O} = 0.018\ \mathrm{kg\,mol^{-1}}$ [163].

The energy difference $\Delta\mathcal{E}$ between the levels involved in V-V and V-T transfer (compare Table 1) is released or taken up as heat. In addition, the difference in energy between the excitation wavenumber (here 2179.77 cm^{-1}) and the vibrational wavenumber (2143 cm^{-1}), which is initially stored in the rotational degree of freedom, is rapidly thermalized and hence yields a contribution proportional to $\dot{N}^{\uparrow}_{CO^*}$ without significant delay. The dissipated heat H is given by

$$H = c \cdot h \cdot \Big(\dot{N}^{V-V}_{CO-N_2} \cdot 188\, cm^{-1} - \dot{N}^{V-V}_{CO-H_2O} \cdot 548\ \mathrm{cm}^{-1} - \dot{N}^{V-V}_{N_2-H_2O} \cdot 736\ \mathrm{cm}^{-1} - \dot{N}^{V-T}_{N_2^*} \cdot 2331\ \mathrm{cm}^{-1} - \dot{N}^{V-T}_{H_2O^*} \cdot 1595\ \mathrm{cm}^{-1} + \dot{N}^{\uparrow}_{CO^*} \cdot 37\ \mathrm{cm}^{-1}\Big) \tag{5.6}$$

Besides R-T relaxation, V-V transfer from CO to N_2, *i.e.* in the endothermic direction, is the fastest process in the absence of H_2O with $\frac{Z_{CO-N_2}}{\hat{Z}_{CO-N_2}} \cdot p^{-1}_{N_2} = 1.8 \cdot 10^5\ \mathrm{s}^{-1}\mathrm{atm}^{-1}$ at $T = 300$ K (normalization to partial pressure of collisional partner, here N_2). In diluted samples of CO in N_2, transfer in the exothermic direction can be neglected. For V-T relaxation of N_2^*, $\frac{Z_{N_2-N_2}}{\hat{Z}_{N_2-N_2}} \cdot p^{-1}_{N_2} = 2\ \mathrm{s}^{-1}\mathrm{atm}^{-1}$. In focused beams, exchange of N_2^* by N_2 via diffusion is hence the dominant effective relaxation pathway for N_2^* (compare section 5.3.4 and Figure 5.18). The slowly relaxing population $N_{N_2^*}$ is an effective buffer for the energy absorbed by CO that does not contribute to the generation of photoacoustic signals due to its very slow response. Therefore, as pointed out by Truong *et al.* [158], photoacoustic signals are generated only during V-V transfer from CO^* to N_2. Since this process is endothermic ($\Delta\tilde{\nu} = 188\ \mathrm{cm}^{-1}$), it leads to cooling of the sample and photoacoustic signals of opposite sign (180° phase shift) as compared to signals arising from the release of absorbed energy. This effect of "kinetic cooling" was first described for CO_2 in ambient air [102]. Since 188 cm^{-1} is only a fraction of the absorbed energy, signals arising from V-V transfer are also much smaller than those arising from V-T relaxation.

In the presence of H_2O, CO^* can relax in an exothermic V-V transfer to H_2O (second term in equation (5.6)). For this process, $\frac{Z_{CO-H_2O}}{\hat{Z}_{CO-H_2O}} \cdot p^{-1}_{H_2O} = 4.2 \cdot 10^6\ \mathrm{s}^{-1}\mathrm{atm}^{-1}$ (normalized to partial pressure of H_2O). Similarly, N_2^* relaxes in collisions with H_2O (third term in equation (5.6)) at a rate $\frac{Z_{N_2-H_2O}}{\hat{Z}_{N_2-H_2O}} \cdot p^{-1}_{H_2O} = 2.2 \cdot 10^5\ \mathrm{s}^{-1}\mathrm{atm}^{-1}$. V-T relaxation of $\mathrm{H_2O}^*$ (fourth and fifth term in equation (5.6)) can be considered instantaneous since it is much faster than the rates of excitation of H_2O. Inelastic collisions with H_2O are exothermic and hence counteract endothermic V-V transfer from CO^* to N_2, which leads to the (partial) cancelling of photoacoustic signals at a concentration of H_2O of ~ 0.25 $\%_V$ in Figure 5.5.

5.2.2. Simulation and Comparison with Experiment

Using equations (5.1) - (5.6), the photothermal heat dissipation H was simulated in accordance with the experimental conditions corresponding to Figure 5.5. Simulations were carried out in Matlab using the finite element method to stepwise calculate the temporal evolution of H in response to wavelength modulated absorption. The initial excited state

populations of all molecular species at $t = 0$ was set zero and the simulation was carried out over several modulation periods until all populations N reached a steady (yet periodically modulated) state. From the rates $\dot{N}(t)$ of all molecular species the heat $H(t)$ was calculated using equation (5.6). The Fourier transform of the last modulation period of $H(t)$ at the second harmonic of the modulation frequency yielded the complex amplitude $\widehat{H}(2f_{mod})$ that is directly proportional to the photoacoustic signal (compare equation (3.7)). The Matlab script for the simulation is given in Appendix A). The resulting amplitude and phase of $\widehat{H}$ for H_2O concentrations from 0 $\%_V$ to 2.2 $\%_V$ are given in Figure 5.7. The simulation closely resembles the experimental data shown in Figure 5.5.

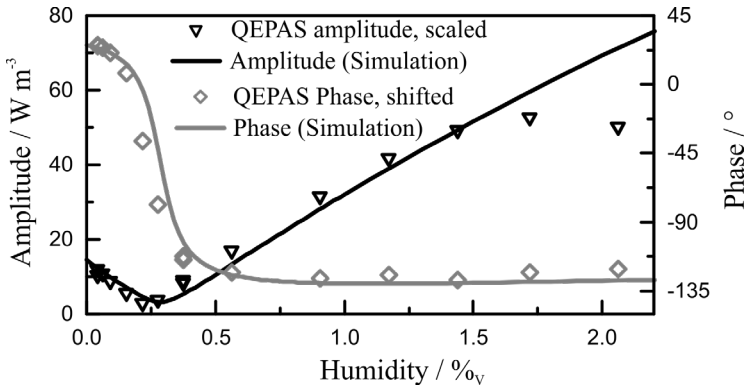

Figure 5.7. Simulation of the photothermal response H of CO in N_2 at varying humidity and conditions identical to those in Figure 5.5. Solid line: simulation of H. Data points: scaled QEPAS amplitude and shifted QEPAS phase, compare Figure 5.5.

For comparison of the simulation with QEPAS signals, the QEPAS amplitude was scaled and its phase was shifted, but no fitting of any parameter of the model described above was performed. The absolute phase differs between simulation and experiment due to additional contributions in the photoacoustic and electronic signal chain. The decrease of the experimental QEPAS amplitude at high humidity is not yet understood and is in contrast to data presented in [125,157].

In conclusion, the agreement of simulations with experiment confirms that the observed trend of the photoacoustic signal of CO with humidity originates from a competition between the kinetic cooling effect of V-V transfer between CO and N_2 and the exothermic relaxation of CO and N_2 in collisions with H_2O.

5.3. Quartz Enhanced Photoacoustic Spectroscopy in a High Finesse Cavity at Optical Saturation

As discussed in section 3.5, the sensitivity of PAS and QEPAS can be strongly increased by exploiting the resonant enhancement of optical power P inside high finesse optical cavities. Here, the design and experimental implementation of a mid-IR intracavity QEPAS (I-QEPAS) spectrometer will be presented. Considerations regarding the cavity design and

mode of operation of the I-QEPAS setup will be discussed in section 5.3.1, including aspects specific for the Brewster window cavity used in this thesis. The final experimental setup will be described in detail in section 5.3.2 and the power enhancement inside the cavity will be determined to a factor of 250. I-QEPAS spectra of ambient air featuring absorption lines of H_2O, N_2O and CO with peak absorption coefficients of ~ 10^{-6} cm^{-1} are presented in section 5.3.3. Saturation broadening of the CO line is observed and saturation in I-QEPAS is quantitatively discussed in section 5.3.4, including the prediction of saturation intensities from the molecular relaxation model derived in section 5.2.1. Saturation intensities of CO are retrieved from I-QEPAS as well as CRDS measurements. The impact of optical saturation on I-QEPAS sensing of CO is discussed in section 5.3.5. The performance of the I-QEPAS spectrometer is determined by means of Allan-variance analysis in section 5.3.6 and detection limits are compared to 2*f*-WM-QEPAS measurements without cavity enhancement.

5.3.1. Design Considerations for an Intracavity QEPAS Spectrometer

The increase of sensitivity of QEPAS based on cavity enhancement relies on increasing the optical power inside a cavity without increasing the noise. The challenges associated with achieving low-noise power buildup in high finesse cavities were discussed in sections 2.2 and 2.3. Here, practical considerations for realizing I-QEPAS with low-noise power buildup are summarized.

Laser locking. To achieve the maximum power buildup possible for a given pair of mirrors (compare equation (2.16)) in an experiment, the laser wavelength must be tightly locked to a cavity resonance. Although PDH-locking of QCLs to high finesse cavities was successfully demonstrated [69,164], it is difficult to use PDH-locking for I-QEPAS due to the necessity of modulating the intracavity power. Since the laser must necessarily be out of resonance for 50 % of the time, the laser lock is interrupted during down-time and must be re-established during every period of modulation. Re-establishing the lock takes some amount of time that may vary from one period to another, which can cause significant amplitude and phase noise of the intracavity power depending on the modulation frequency and the laser frequency noise. Nevertheless, PDH-locking was successfully used for intracavity PAS with intensity modulation using a low-noise near-IR external-cavity diode laser [133]. For I-QEPAS in the mid-IR using a DFB-QCL, however, this approach appears not feasible due to the high modulation frequency and the increased frequency noise associated with the short laser resonator (compare section 2.4.1). Furthermore, due to the poor availability of electro-optic modulators in the mid-IR spectral region, frequency modulation is typically achieved by direct current modulation, which is accompanied by amplitude modulation and gives rise to an offset of the PDH-error signal. Since this offset is missing if the laser power is interrupted, a feedback loop adjusted for a given offset will

rapidly tune the laser wavelength away from the cavity resonance if no measures are taken to compensate for the missing offset during down-time.

For these reasons, optical feedback (OF) locking appears to be a more promising alternative for I-QEPAS. OF locking was used successfully for intracavity PAS using an EC-QCL [134] as well as a diode laser [165]. In these works, to achieve modulation of intracavity power, the laser wavelength was modulated around a cavity resonance, while OF locked the wavelength during every passage of the cavity resonance wavelength (compare section 5.3.2). As discussed in section 2.5, the FP cavity is ill-suited for OF locking since the reflectivity is highest for off-resonance wavelengths. Although OF locking can be achieved from a two-mirror FP cavity [166], it requires an intentional mismatch of the laser- and cavity mode, which conflicts with the power buildup in the cavity. Hence, three mirror V-shaped cavities were used in previous works. While this is a viable solution, other cavity designs compatible with OF locking are worth being investigated.

Noteworthy properties of the Brewster window cavity. In particular, the Brewster window (BW) cavity introduced in section 2.2.2 features some interesting properties for intracavity PAS, as compared to all-mirror cavities. First, the volume of the gas cell can be decreased drastically by using the Brewster window as a window of the gas cell. Hence, a small sample volume can be enclosed by a cavity mirror and the Brewster window, and the cavity length can be chosen freely without increasing the sample volume (compare section 7.2). Since small gas volumes are a particular strength of PAS as compared to direct absorption spectroscopic techniques (compare section 3.4.1), this is a highly desirable feature. For all-mirror cavities, miniaturization can only be achieved by reducing the cavity length, which increases the free spectral range. A second interesting property of the BW cavity is that, in a single cavity, the finesse and power buildup can be varied by orders of magnitude by adjusting the angle of the window (compare section 5.3.2) [167] or by changing the polarization to *s*, *e.g.* via a half-wave plate. This holds promise to drastically increase the dynamic range of intracavity measurements. Third, using a Brewster window for coupling light into a cavity allows using cavity mirrors designed for maximum reflectivity without taking care of their transmission. Whether or not the Brewster window yields a stronger buildup than a third mirror depends on the non-reflective losses at the Brewster window as compared to those of the mirror. Non-reflective losses at the Brewster window originate from scattering and absorption as well as reflection of *s*-polarized components of the cavity mode. In the mid-IR, scattering is negligible if polished substrates are used. Absorption is strongly wavelength dependent and can be reduced by using thin windows. At $\lambda = 4.5$ µm, the absorption coefficient of CaF_2 is $\sim 3{\cdot}10^{-4}$ cm^{-1}. Reflection of *s*-polarized light is included here as a non-reflective loss since is represents a loss channel for the *p*-polarized mode. Losses due to *s*-polarized reflection may occur due to polarization rotation caused by mirror birefringence. Polarization rotation can

be minimized by rotating the mirrors against each other[150]. Even without polarization rotation, a small fraction of *s*-polarized reflection occurs when a perfectly *p*-polarized Gaussian beam impinges on a dielectric surface at Brewster's angle [168]. This is a consequence of the curved phase front of the beam, which results in the wave-vector having a small component in the s-direction that is zero at the beam axis and increases with distance from the beam axis. Since the radius of the phase front curvature ρ_{pf} varies along the cavity axis (compare equation (2.1)), these losses can be minimized by positioning the window close to the beam waist where ρ_{pf} is large. Another significant loss at the BW is the reflection of *p*-polarized light at the rear surface of the BW that is ineffective in coupling light into the cavity (compare section 2.2.2). Reflection at the rear surface can, however, be eliminated using an appropriately wedged window that puts the rear surface to the exact Brewster's angle.

Choice of mirrors and cavity length. As for all techniques of CES, mirrors of high reflectivity are desired. However, high transmission of the cavity mirrors is important as well since intracavity power enhancement scales with transmission (compare section 2.2). For the BW cavity, mirror transmission is irrelevant and optimum power enhancement can be achieved by tilting the BW (compare sections 2.2.2 and 5.3.2). As discussed in section 2.1.1, the mirrors' radius of curvature ρ_m and the cavity length L_{cav} determine the beam waist radius w_0 and divergence of the fundamental Gaussian mode. For on-beam I-QEPAS, the prong spacing of the QTF puts a constraint on w_0 since the QTF represents a slit aperture. Diffraction losses at circular and rectangular apertures were investigated, amongst others, in [169]. For a rough estimation, the losses at the slit aperture can be estimated as the fraction of the Gaussian intensity profile extending beyond the aperture. For example, this fraction is 100 ppm and 10 ppm if the prong spacing is 5.5 times and 6.25 times larger than w_0, respectively. Even if the losses do not significantly reduce the cavity finesse and power buildup, absorption of this fraction of the intracavity power at the prongs of the QTF can give rise to a significant background signal and increase the noise floor, in particular if intensity modulation is employed. Therefore, a small beam waist must be achieved by using mirrors of small radius of curvature ρ_m and a cavity length L_{cav} close to $2 \cdot \rho_m$ (concentric cavity, compare Figure 2.2). Since many manufacturers do not offer mirrors with $\rho_m < 50$ cm, the prong spacing of conventional QTFs of only 300 µm requires custom mirrors that are hard to come by [135]. Therefore, QTFs specifically designed for QEPAS with increased prong-spacing up to 1.5 mm are ideal for I-QEPAS [122].

Intensity and wavelength modulation in cavities with optical feedback. To excite photoacoustic signals inside the cavity, the power or wavelength inside the cavity must be modulated. If possible, 2*f*-wavelength modulation (WM) is usually preferred in PAS and QEPAS since background signals, *e.g.* from absorption in windows or at the

prongs of the QTF as well as from spectrally broad interfering molecular species, are efficiently suppressed. In a cavity, the wavelength can be modulated continuously via the cavity length or in increments of the FSR by modulating the laser wavelength across multiple consecutive resonances. For the former approach, the laser wavelength must precisely follow the cavity length modulation [170]. Modulation via cavity length is limited to low modulation frequencies due to the inertia of the moving cavity mirror, but also due to the finite response time of light inside the cavity. In order for the intracavity field to be in resonance with the modulated resonator at any time, the scan speed $d\tilde{\nu}/dt$ must be much smaller than the ratio $FWHM/\tau$ of the cavity mode. For example, for an FP cavity with mirrors of $R = 0.999$ and $L_{cav} = 20$ cm, $FWHM/\tau = 240\,\mathrm{kHz}/670\,\mathrm{ns} = 360\,\mathrm{Hz}\ \ \mathrm{s}^{-1} = 12\,\mathrm{cm}^{-1}\mathrm{s}^{-1}$. At kHz modulation frequencies and modulation amplitudes on the order of a few 10^{-2} cm^{-1}, $d\tilde{\nu}/dt$ approaches or exceeds this limit.

This limitation is more relaxed when modulating the wavelength in increments of the cavity's FSR. The idea of intracavity $2f$ – WM QEPAS with optical feedback is illustrated in Figure 5.8. The laser wavelength is modulated (here, a symmetric triangular waveform is used) at a frequency f_{mod} across several free spectral ranges (FSRs) of the cavity. During every modulation period, OF locks the wavelength repeatedly to consecutive cavity resonances (top left panel in Figure 5.8). The wavelength inside the cavity is hence effectively modulated in increments of the FSR. The heat $H(t)$ resulting from absorption of the intracavity power, here assumed to follow the absorbed power without delay, is shown in the bottom left panel of Figure 5.8.

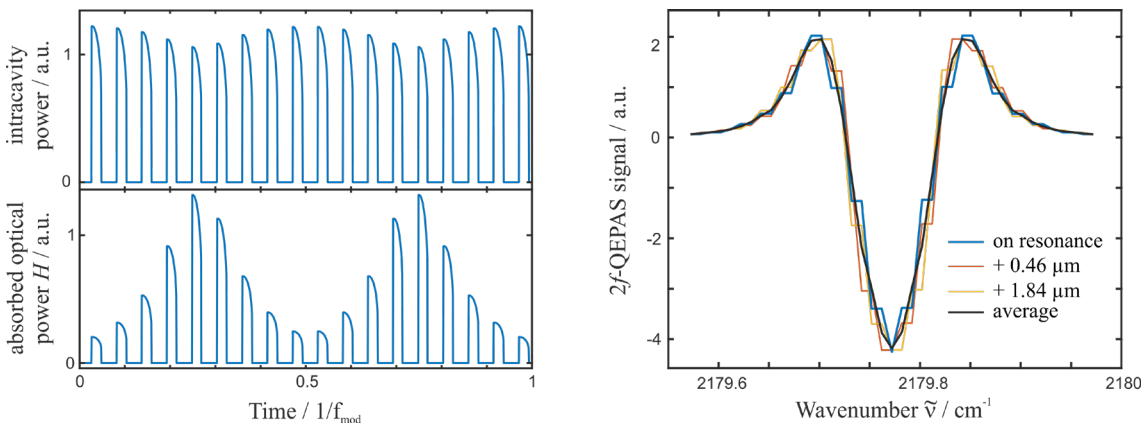

Figure 5.8. Principles of intracavity $2f$ - wavelength modulation QEPAS, see text. Simulation parameters: $L_{cav} = 28$ cm, modulation amplitude: 4 FSRs (8 FSRs peak to peak), absorption line width: 0.05 cm^{-1} FWHM. Left, top panel: Intracavity power while the laser wavelength is modulated across eight FSRs of the cavity around the molecular resonance. Left, bottom panel: absorbed optical power H during that modulation. Right: $2f$-WM-QEPAS spectrum obtained by tuning the laser center wavelength across the absorption line, calculated for varying cavity length. For the blue line, a cavity resonance coincides with the center of the absorption line. Changing the cavity length by the indicated amounts detunes the cavity resonance with respect to the absorption line. Averaging over varying cavity lengths yields the familiar $2f$-WM-spectrum.

The photoacoustic signal is obtained by demodulation of $H(t)$ at $2f_{mod}$. The stepwise wavelength tuning gives rise to distortions in the spectra obtained by scanning the laser center wavelength across the absorption line. Changing the cavity length influences the obtained spectrum because the frequencies at which the spectrum is sampled change in accordance with the cavity length. Hence, the cavity length should be locked to the molecular resonance. Alternatively, the undistorted $2f$-WM spectrum can be recovered by scanning the cavity length across one FSR and averaging the recorded signals over the cavity length. To achieve OF locking to consecutive cavity resonances, the laser-cavity distance must be set to a multiple of the cavity length to ensure the same OF phase for each resonance (compare section 2.5). A disadvantage of the proposed intracavity $2f-$ WM QEPAS technique is that it is only applicable if the FSR of the cavity is smaller than the FWHM of the absorption line. It is therefore restricted to long cavities, which implies a larger gas volume and large beam waist radius, and/or to high gas pressure. Also, scanning over multiple FSRs reduces the time the laser is locked to each resonance, which can cause a significant distortion of the observed buildups as compared to those shown in Figure 2.10 and Figure 5.8 since the intracavity field cannot follow changes that are faster than the photon lifetime in the cavity. Hence, the cavity acts as a low-pass filter on the sharp edges of the buildups. This is illustrated in Figure 5.9. The cavity buildup was observed by measuring the back-reflected light from the cavity on a photodetector (compare Figure 5.10) while scanning the laser wavelength across a cavity resonance at different modulation frequencies. The ring-down time of the used cavity was ~ 520 ns.

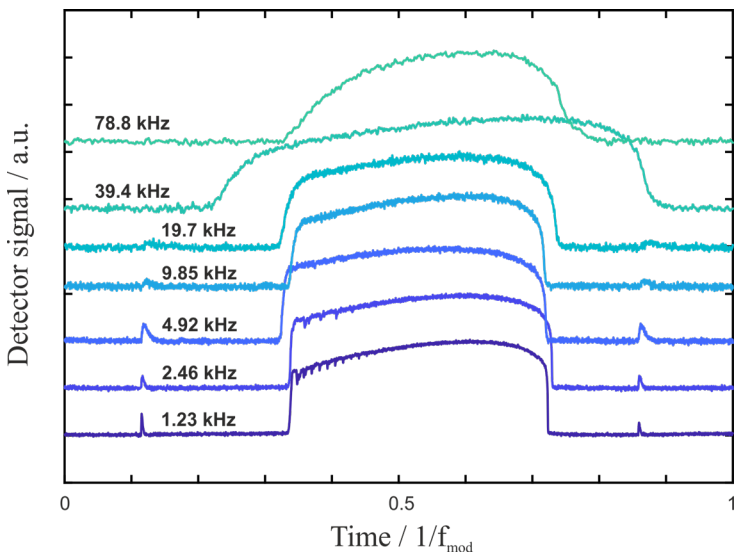

Figure 5.9. Buildups observed when ramping the laser wavelength across a cavity resonance at different modulation frequencies f_{mod}. An offset between the lines was introduced for better visibility. Note that the modulation amplitude changes between consecutive scans, which is why the width of the buildups varies.

Even for modulation frequencies well below the inverse ring-down time, the buildups are significantly affected by the finite response time of the intracavity field.
Due to the limitations of the intracavity 2*f*-WM QEPAS approach regarding the sample pressure, cavity length and modulation frequency, intensity modulation was preferred. The experimental realization of I-QEPAS with intracavity intensity modulation will be presented in detail in the next section.

5.3.2. Experimental Setup for I-QEPAS and Experimental Procedures

Optical Setup. The I-QEPAS spectrometer set up during this thesis is depicted schematically in Figure 5.10. A thermo-electrically cooled DFB-QCL (*AdTech Optics*) emitted 45 mW of optical power in continuous wave operation at a wavelength of 4.59 µm. A half-wave plate and polarizer set the polarization to parallel with respect to the CaF_2 window in the cavity. Three plano-spherical lenses of focal lengths 200 mm, -200 mm and 150 mm were used for mode-matching to the fundamental Gaussian mode of the cavity. The cavity mirrors (*Layertec*) were deposited on a one inch fused silica substrate with a radius of curvature of 150 mm and a measured reflectivity of 0.9992 (compare section 2.3). The cavity length was 0.28 m and could be fine-tuned using a piezo-electrically actuated cavity mirror mount (*Thorlabs*, KC1-PZ/M) to vary the resonance frequency over a full free spectral range (FSR). A CaF_2 window of 2 mm thickness was positioned in the cavity close to Brewster's angle ($\beta_B = 54.5°$ at 4.59 µm, compare section "optical impedance matching" below) using a compact rotation mount (*Thorlabs,* FBTP). Light was coupled into the cavity via reflection at the front surface of the Brewster window [171]. A thermo-electrically cooled mercury-cadmium-telluride photodetector (PCI-2TE-12, *Vigo Systems S.A.*) detected a small fraction (~ 1%) of the light reflected back from the cavity to the laser picked up via a beam splitter.

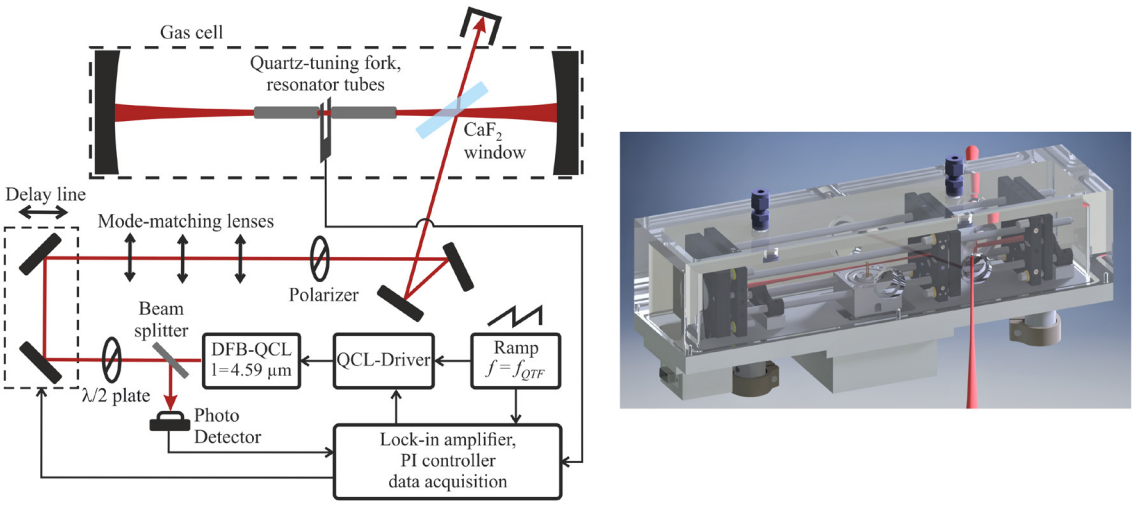

Figure 5.10. Left: Schematic of experimental setup, detailed description see text. Right: Rendered image of the cavity and the quartz tuning fork inside the gas cell.

Two mirrors on a piezo-actuated stage were used as a delay line to fine-tune the phase of light back-reflected into the laser (compare section 2.2). A quartz tuning fork (QTF) and resonator tubes (L = 12.45 mm, inner diameter = 1.5 mm) were positioned in the center of the cavity using a compact five-axis stage (*Thorlabs,* PY005/M). The QTF was a custom design for QEPAS with a resonance frequency of 15.82 kHz and a prong spacing of 1.5 mm (see [122], design S15). It was provided in a ready to use module (prototype of *Thorlabs*, ADM01) including electronic amplification and excitation circuitry by *Thorlabs GmbH*. The use of the resonator tubes yielded a QEPAS signal-to-noise enhancement by a factor of six as compared to the bare tuning fork. The amplified signal from the tuning fork was demodulated using a lock-in amplifier (*Zurich Instruments*, MFLI) and normalized by the photodetector signal, which was demodulated at the same frequency using the same lock-in amplifier. The detector signal recording the back reflection from the cavity is proportional to intracavity power and was used to normalize the recorded QEPAS signal to optical power. The optical cavity as well as QEPAS module and Brewster window were enclosed in an aluminum gas cell (volume = 1.7 L) with CaF_2 windows for in- and out coupling of the laser beam. The full optical setup was enclosed in a simple housing to reduce the impact of turbulent airflow on the optical feedback phase.

Mode of operation. To generate photoacoustic signals inside the cavity, the optical power inside the cavity was modulated at the resonance frequency f_{QTF} of the tuning fork. Efficient and low-noise modulation of intracavity power was achieved by exploiting optical feedback locking (compare section 2.5). The detector signal, which is proportional to the intracavity power, during a period of laser modulation is shown in Figure 5.11.

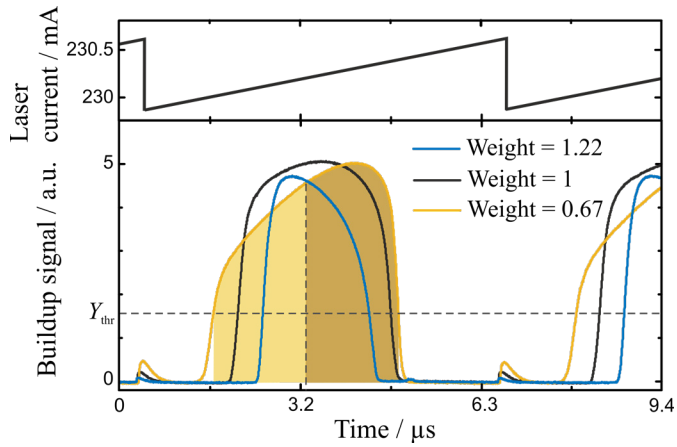

Figure 5.11. Cavity buildups recorded during ramped current modulation of the QCL. The three lines represent different optical feedback phases, corresponding to different "weights" of the buildups. The feedback phase is detected and corrected based on weighting of the first and second half of the buildups (shaded areas, see text). Incomplete buildups observed during the falling edge of current modulation do not interfere with I-QEPAS measurements.

The wavelength was modulated via the driving current of the QCL using a small amplitude ramping signal applied to the analog control input of the QCL-driver (*Wavelength electronics,* QCL-OEM 300). Starting at $t = 0$ in Figure 5.11, the free running laser wavelength λ_{free} is initially detuned from the cavity resonance wavelength λ_{res}. As λ_{free} approaches λ_{res}, some fraction of the incident light resonates in the cavity and is reflected back into the laser, *i.e.* optical feedback occurs. The response of the QCL to optical feedback depends, amongst others, on the phase of the back-reflected light, which was adjusted via the physical length between the laser and the cavity using a delay line (compare Figure 5.10). If the back-reflection is in phase with the emitted light, optical feedback causes a dramatic stabilization of the emitted wavelength to a wavelength closely matching λ_{res}. This process leads to highly efficient coupling of light into the cavity and accordingly large buildup of optical power. As λ_{free} is detuned from λ_{res} far enough during the modulation, the laser wavelength returns to λ_{free} and no buildup occurs. A cycle of modulation is completed by swiftly shifting λ_{free} to the opposite side of λ_{res}.

Experimentally, ramped modulation was preferred over sinusoidal or triangular modulation at $f_{QTF}/2$ [134] since, generally, the observed buildup was not symmetric with respect to scan direction. Buildups recorded during triangular wavelength modulation are shown in Figure 5.12 for varying OF phase. The buildups resemble the expected shapes when the current and wavelength are increased (compare Figure 2.10). However, the buildups of the opposite scan direction appear distorted and the OF lock seems to be interrupted early during the buildups.

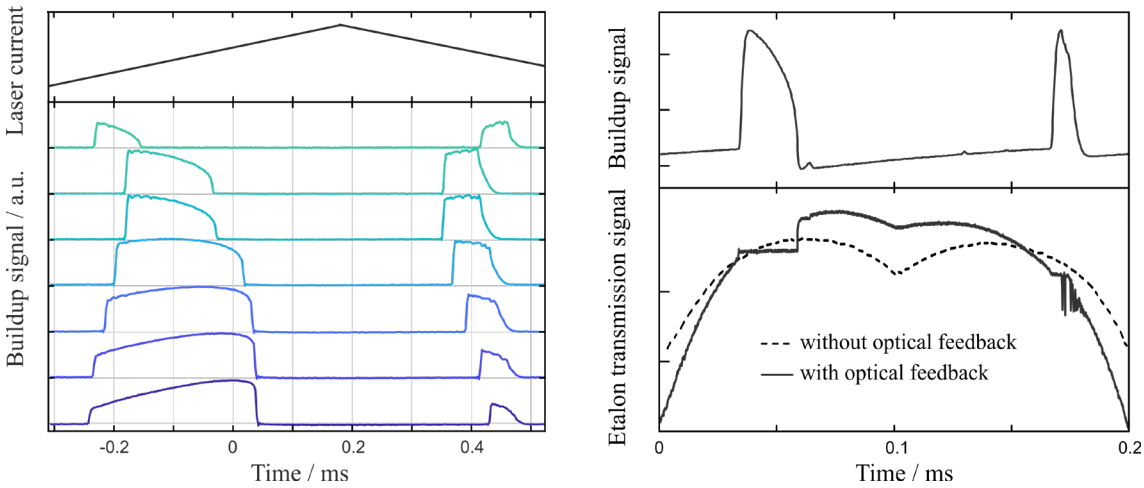

Figure 5.12. Cavity buildups with optical feedback observed during triangular modulation of the laser wavelength around a cavity resonance. Left: Buildup signal for varying feedback phase. Right: Buildup signal (top) and etalon transmission signal (bottom) during a triangular wavelength scan. The slope in the off-resonance buildup signal is a measurement artifact from the AC-coupled photodetector. While the buildups resemble the expected shapes while the current and wavelength are increased (compare Figure 2.10), the buildups of the opposite scan direction appear distorted.

In another experiment, the laser frequency during this modulation was monitored by recording the transmission through a germanium etalon (FSR = 0.022 cm^{-1}). To this end, a beam splitter was used to direct a fraction of the laser output through the etalon onto a photodetector. The etalon transmission signal is also shown in Figure 5.12, together with the buildup signal recorded in back-reflection from the cavity using a second photodetector. The etalon transmission clearly shows that the wavelength hardly changes during OF locking in the first half of the modulation (increasing wavelength). The fast fluctuations of the transmission signal observed when the wavelength is scanned in the opposite direction indicate that the wavelength rapidly fluctuates between locked and free-running wavelength.

The source of this asymmetry could not be identified or overcome experimentally, and a similar behavior was, to the best of my knowledge, not reported previously. Asymmetry with respect to scan direction may arise from interference with higher order cavity modes, as their resonance frequencies are shifted to one side of the fundamental mode [48] (here, to smaller frequencies/larger wavelengths). Also, OF from reflections off the rear surface of the Brewster window may compete with OF from the front surface. Higher order modes were investigated as the source of the asymmetry by placing a 1 mm pinhole in the center of the cavity and varying its position to selectively attenuate higher order modes. No significant effect on the symmetry of the buildups was observed. Also, no changes were observed when decreasing the feedback ratio, *i.e.* the intensity of light back-reflected into the laser. Also, a spatial filter was installed between the laser and the cavity to selectively block the resonant light reflected back towards the laser at the rear surface of the Brewster window (compare Figure 2.6), but no notable impact on the buildups was observed. Future experiments with wedged Brewster windows will eliminate reflections at the rear surface of the Brewster window as a possible source of the observed asymmetry.

Locking loops for OF-phase and laser wavelength. To record QEPAS spectra at increments of the cavity's FSR, the same feedback phase must be achieved for all consecutive resonances of the cavity. To this end, the distance between laser and cavity was adjusted to a multiple of the cavity length [78]. To stabilize the feedback phase in wavelength locked operation, a number of methods based on the shape of the buildup signal were demonstrated previously [172–174]. Here, the detector signal was digitized and analyzed in a real-time application programmed in Matlab on a personal computer. Each buildup was isolated based on a signal threshold level (Y_{thr} in Figure 5.11) and the first and second half (by number of samples) of the buildup were integrated (shaded areas in Figure 5.11). The error signal for the proportional-integral (PI) algorithm was obtained by division of the areas under the first half and the second half of the buildups. The set point of the so obtained "weight" of the buildups was chosen as 0.82. The feedback phase was

adjusted via the delay line using the analog control input of the piezo controller (*Physik Instrumente*, E-536.30).

The detector signal shown in Figure 5.11 also served for locking the laser center wavelength to a cavity resonance based on a standard wavelength modulation approach [175]. To this end, the signal was demodulated at the first harmonic of the modulation frequency using the lock-in amplifier. A digital laser locking module (*Toptica Photonics*, Digilock 110) hosted a PI controller that regulated the in-phase component of the demodulated signal to zero by acting on the laser current via the analog control input of the QCL driver.

CRDS measurements. The setup also allowed performing cavity ring-down spectroscopy (CRDS). For CRDS, the laser was operated under ramped current modulation as discussed above. Ring-downs were initiated by swiftly reducing the laser current below the threshold current for 25 µs using the analog control input of the QCL driver. The detector signal was digitized with a vertical resolution of 8 bit using an oscilloscope (*LeCroy*, Waverunner 64 Xi). Each ring-down was fitted in post processing using a three parameter single exponential model and the fitted ring-down times were averaged.

The initiation of ring-downs was synchronized to the ramped current modulation at 500 Hz independent from a threshold detector signal commonly used in CRDS [171]. The detector signal recorded during a CRDS experiment is shown in Figure 5.13. The repetition rate of ring-downs (500 Hz) was kept low compared to the inverse down time of ring-down events of 25 µs (1.3 % duty cycle) to limit the impact of the reduced heat load on the laser wavelength. Also, as will be discussed in section 5.3.4, the low modulation frequency ensures that the population inversion (saturation) of CO reaches its steady-state value before the ring-down is initiated.

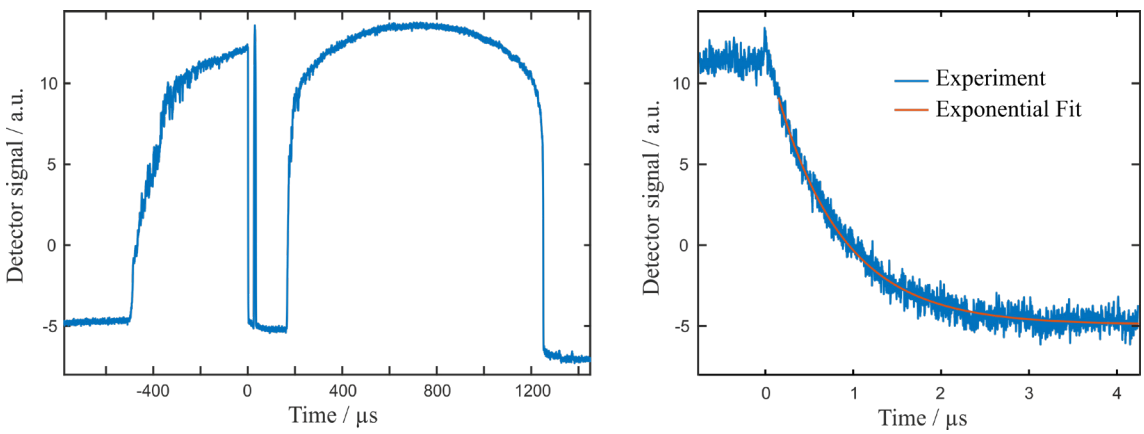

Figure 5.13. Typical detector signals during a CRDS experiment. Left: signal during a period of ramped current modulation. The laser is switched off at t = 0 µs for 25 µs. A short buildup is observed at t ≈ 25 µs when the laser is switched back on and its wavelength quickly sweeps across the cavity resonance. After ~ 150 µs, the wavelength stabilizes again to the cavity resonance via optical feedback. Right: ring-down signal and exponential fit.

2*f*-WM QEPAS measurements. To evaluate the gain in sensitivity achieved through the optical cavity, measurements of CO and H_2O were referenced against 2*f*-WM QEPAS. To this end, the QEPAS module was removed from the optical cavity and 2*f*-WM QEPAS measurements were performed as discussed in section 5.1.1 in line-locked operation.

Optical impedance matching. To maximize the gain in sensitivity of I-QEPAS, the intracavity power buildup was maximized. As was discussed in section 2.2, the optical power that builds up inside a FP-cavity on resonance depends not only on the cavity losses, but also on the transmission of the mirror through which light is coupled into the cavity. For the Brewster window cavity, rather than the transmission of the in-coupling mirror, the reflectivity R_{BW} of the Brewster window determines how much light is coupled into the cavity. R_{BW} and hence the power buildup can be adjusted by changing the angle at which the window is placed in the cavity (compare equation (2.18)). The bidirectional power P_{intra} circulating inside the cavity was derived in section 2.2.2 and is given by equation (2.20). The largest buildup $\frac{P_{intra}}{P_0} = \frac{1}{4}\frac{R_M}{(1-R_M+\alpha L)}$ is found for $R_{BW} = \frac{1}{2}(1 - R_M + \alpha L)$, *i.e.* for R_{BW} matching half the combined half round-trip losses ℓ of all other elements in the cavity. The losses $\ell = 1 - R_M + \alpha L_{cav}$ were unknown when the mirrors were received and could not be measured using CRDS without the Brewster window since the mirrors were deposited on non-transparent substrates, preventing coupling into the cavity through the mirrors. Therefore, the losses were retrieved from measurements of P_{intra} and ring-down time τ at different angles of the Brewster window. P_{intra} was monitored by recording the I-QEPAS signal from a water line at 2178.9 cm^{-1} from ambient air at atmospheric pressure and normalization of signals to humidity recorded separately. τ is related to the cavity losses as (compare section 2.6)

$$\frac{1}{\tau} = \frac{c}{2L_{cav}}(1 - R_M + \alpha L + 2R_{BW}) \tag{5.7}$$

Solving equation (5.7) for R_{BW} and inserting in equation (2.20) allows fitting of the I-QEPAS signal recorded for different τ using the combined losses $\ell = 1 - R_M + \alpha L_{cav}$ and P_0 as fitting parameters. The recorded I-QEPAS signal as well as the fit of equation (2.20) and corresponding power buildup P_{intra}/P_0 are shown in Figure 5.14. Two outliers indicated in Figure 5.14 were excluded for the fitting. The retrieved combined losses (half round-trip) are $\ell = 8{\cdot}10^{-4}$. At the optimized angle of the Brewster window of $\beta = 52.2°$ ($\beta_B = 54.54°$), $P_{intra}/P_0 = 312$. Since perfect mode-matching as assumed in equation (2.20) was not achieved, the actual power buildup is lower than given in Figure 5.14 [52]. To measure the mode-matching efficiency and effective intracavity power at maximum buildup, the cavity transmission $T_{cav,eq}$ on resonance was measured using a power meter placed behind the Brewster window (position of beam dump in Figure 5.10).

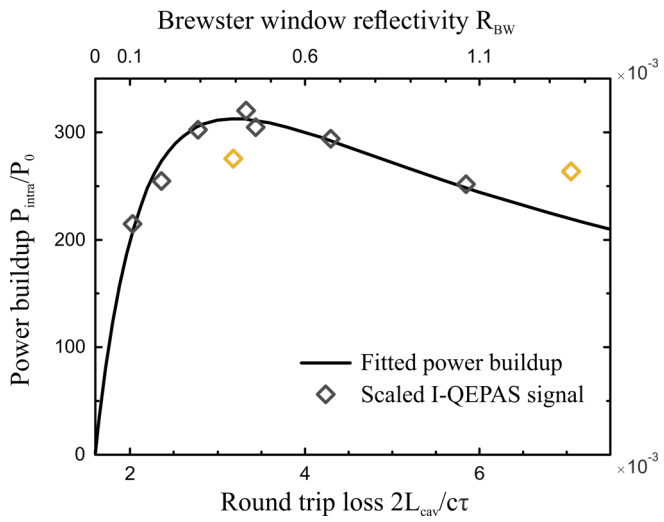

Figure 5.14. Intracavity power buildup (calculated assuming perfect mode-matching, see equation (2.20)) and scaled I-QEPAS signal from water (measured, outliers marked yellow) versus Brewster window reflectivity. Adjusting the reflectivity of the Brewster window via its angle allows maximizing the intracavity power buildup.

The measurement was compared to the theoretically expected transmission given by equation (2.21), which equals $T_{cav,eq} = 9/16$ for the impedance matched cavity. The ratio $\frac{1-T_{measured}}{1-T_{cav,eq}}$ gives a coupling efficiency of 81% and, with an incident laser power of 25 mW on the Brewster window, an intracavity power of $P_{intra} = 0.025\,\mathrm{W} \cdot 312 \cdot 0.81 = 6.3\,\mathrm{W}$. All measurements presented below, except for the I-QEPAS spectrum shown in Figure 5.16, were recorded with optimized angle and $P_{intra} = 6.3$ W, corresponding to a peak intensity $I_0 = 73$ W mm^{-2} at the center of the cavity (compare equation (5.15)). For the data in Figure 5.16, $P_{intra} = 2.2$ W, corresponding to $I_0 = 26$ W mm^{-2}.

Measurements and sample preparation. I-QEPAS spectra were recorded by stepping the laser wavelength via temperature in increments of the cavity's FSR. The laser wavelength and optical feedback phase were locked for each cavity resonance and signals were recorded for a given time (see below). For all other measurements, the laser wavelength was locked to a cavity resonance and the resonance wavelength of the cavity was tuned to the absorption peak via the piezo-driven cavity mirror mount.

All measurements presented herein were performed in a steady flow of sample gas at flow rates below 500 sccm at ambient temperature. Samples of defined concentration and humidity were prepared as discussed in section 5.1.1.

5.3.3. Spectra of Ambient Air

An I-QEPAS spectrum of ambient air was recorded by stepping the laser wavenumber in increments of the cavity's FSR and averaging 25 s of data for each frequency step. The amplitude of the I-QEPAS signal was normalized by the amplitude of the demodulated detector signal to normalize to intracavity power.

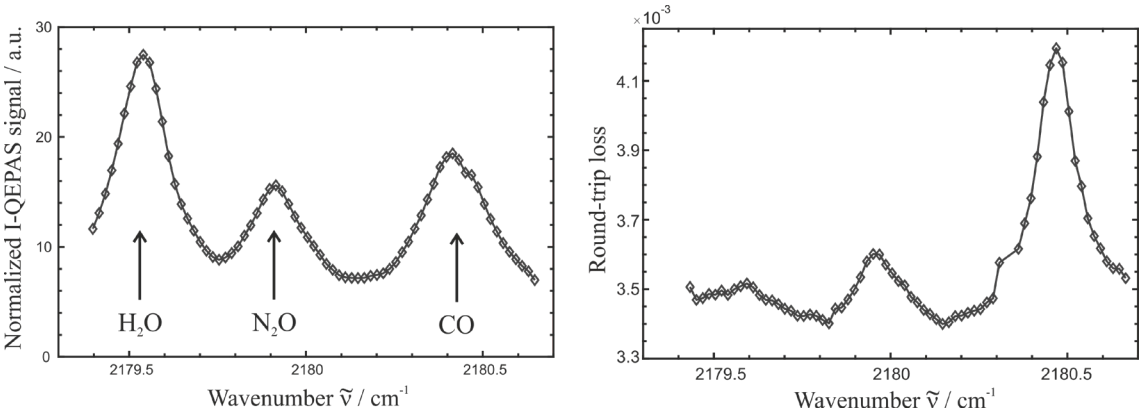

Figure 5.15. Spectra of ambient air ($p = 1$ atm, 0.6 $\%_V$ humidity). Left: I-QEPAS spectrum, normalized by detector signal (~ intracavity power). Right: CRD spectrum, round-trip loss $2L_{cav}/c\tau$.

During the same scan, a CRD spectrum was recorded as well. 300 ring-down events were recorded for every frequency step following the acquisition of I-QEPAS signal. The I-QEPAS and CRD spectrum are shown in Figure 5.15.

Within the tuning range of the QCL, absorption lines of three species can be identified: H_2O (2178.90 cm^{-1}), N_2O (combination of three lines at 2179.28 cm^{-1}, 2179.28 cm^{-1} and 2179.34 cm^{-1}) and CO (2179.77 cm^{-1}) [89]. The QEPAS signal of both, N_2O and CO are much weaker relative to H_2O than in the CRDS experiment. Based on an empty cavity round-trip loss of $3.3 \cdot 10^{-3}$ and the cavity length $L_{cav} = 28$ cm, the peak absorption coefficients of the three lines in Figure 5.15 can be calculated from the ring-down measurements as $\alpha = \frac{1}{2L_{cav}}\left(\frac{2L_{cav}}{c\tau} - 3.3 \cdot 10^{-3}\right)$. The I-QEPAS signal normalized to the peak absorption coefficients of the three lines, corresponding to the cell constant k_{cell} in equation (3.8), are approximately $1.2 \cdot 10^6$ a.u. cm (CO), $2.9 \cdot 10^6$ a.u. cm (N_2O) and $7.1 \cdot 10^6$ a.u. cm (H_2O). The significant differences between the three species originate mostly from the relaxation rates of CO and N_2O (compare sections 3.1.2 and 5.2.1) being slow compared to the modulation frequency of 15.82 kHz. In contrast, V-T transfer in H_2O is fast, yielding complete relaxation and strong photoacoustic signals.

An I-QEPAS spectrum of ambient air at a reduced pressure of 250 mbar is shown in Figure 5.16. The I-QEPAS spectrum matches scaled simulated reference spectra [18] of H_2O and N_2O. On the contrary, the CO band at 2179.77 cm^{-1} is much broader than the simulated absorption profile. As will be discussed in the following, the line broadening can be attributed to optical saturation (saturation broadening).

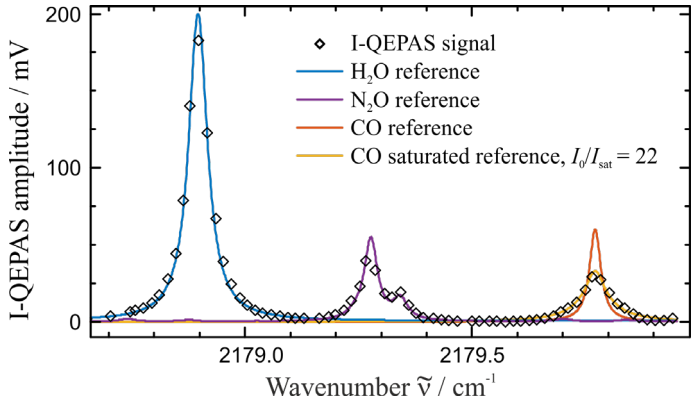

Figure 5.16. I-QEPAS spectrum of ambient air at $p = 250$ mbar. Scaled simulated absorption spectra of H_2O and N_2O nicely resemble the measured I-QEPAS spectrum. The CO absorption line at 2179.77 cm^{-1} is significantly broadened as compared to the reference absorption spectrum due to saturation broadening. Observed peak absorption coefficients of H_2O and CO estimated from ambient concentration levels are ~ $3 \cdot 10^{-6}$ cm^{-1} and $7 \cdot 10^{-6}$ cm^{-1}.

5.3.4. Saturation of CO in I-QEPAS and CRDS

While the large majority of previous studies confirmed the direct proportionality between photoacoustic signals Y and P, very high P eventually leads to saturated absorption and a non-linear scaling of Y with P [176–178]. Saturated absorption can be described as a decrease of absorption coefficient α with increasing intensity I [179].

$$\alpha(\tilde{\nu}, I) = \alpha_0 \frac{\bar{\Gamma}(\tilde{\nu})}{1 + \frac{I}{I_{sat}} \bar{\Gamma}(\tilde{\nu})} \tag{5.8}$$

Herein, $\bar{\Gamma}(\tilde{\nu})$ is the peak normalized line-shape function, α_0 is the absorption coefficient on resonance without saturation and I_{sat} is the saturation intensity. In a laser beam of Gaussian shape, the intensity and hence the degree of saturation I/I_{sat} vary over the cross section of the beam according to equation (2.5). The average absorption coefficient in a collimated Gaussian beam observed when the beam is focused onto a detector is given by [179]

$$\alpha = \alpha_0 \frac{I_{sat}}{I_0} \ln\left(1 + \frac{I_0}{I_{sat}} \bar{\Gamma}(\tilde{\nu})\right) \tag{5.9}$$

Herein, I_0 is the intensity at the center of the beam. The saturation intensity I_{sat} reflects how easily a molecular transition can be saturated, which depends on the transition dipole moment of the transition and the relaxation rate. Very generally, saturation is observed when the rate of excitation $\gamma^{\uparrow}$ (compare Equation (3.1)) approaches or is bigger than the rate of relaxation $\gamma^{\parallel}$ (compare section 5.2.1), hence less molecules are available for excitation. Giusfredi *et al.* derived the saturation intensity for a ro-vibrational transition of CO_2 [179]. Their model assumptions for describing excitation and relaxation in CO_2 is also applicable to CO, with the small difference that, here, an R-branch transition is targeted. Hence, I_{sat} for a homogeneously broadened absorption line is given as

$$I_{sat} = \frac{\gamma_{\parallel}}{A_{ba}} \frac{8\pi^2 \tilde{\nu}_0^3 c^2 h}{\Gamma_0} \frac{g_1}{g_2} \tag{5.10}$$

Herein, Γ_0 is the peak value of the area normalized line-shape function, given by $\Gamma_0 = \frac{2}{\pi} FWHM^{-1}$ for a Lorentzian profile of given FWHM (Γ_0 in meter). For inhomogeneously broadened absorption lines (Doppler broadening), the reader is referred to [179]. Using equation (5.10) and the model for relaxation of CO in N_2 and H_2O derived in section 5.2.1, the saturation intensity of CO can be calculated at varying pressure and humidity using $A_{ba} = 17.91\ s^{-1}$ and FWHM = 0.116 $cm^{-1}\ atm^{-1}$ [93]. Equation (5.3) gives the number of relaxing CO molecules $\dot{N}^{\parallel}_{CO^*}$ per unit volume and time, from which the relaxation rate for a single molecule $\gamma^{\parallel}$ is derived by division by the number density of excited state CO molecules.

$$\gamma^{\parallel} = -\frac{\dot{N}^{\parallel}_{CO^*}}{N_{CO^*}} = \frac{Z_{CO-N_2}}{\hat{Z}_{CO-N_2}} + \frac{Z_{CO-H_2O}}{\hat{Z}_{CO-H_2O}} = p_{N_2} \cdot 0.178\ \text{MHz atm}^{-1} + p_{H_2O} \cdot 4.3\ \text{MHz atm}^{-1} \tag{5.11}$$

Herein, the vibrational energy transfer between CO and N_2 as well as CO and H_2O was assumed unidirectional from CO to the collision partner, which is the case for fast relaxing collision partners (H_2O) and low concentrations of CO. Also, collisional energy transfer was assumed to be the only relaxation pathway for CO. Alternative pathways exist, in particular diffusion of excited molecules out of and ground-state molecules into the volume of the laser beam, and must be taken into account, especially at lower pressures [180]. Hence, equation (5.11) gives a lower limit for $\gamma^{\parallel}$ and I_{sat}.

At high pressure, with the collision rates $Z_{A\text{-}B}$ and collision numbers $\hat{Z}_{A-B}$ given in section 5.2.1, I_{sat} can be approximated as

$$I_{sat} = p^2 \cdot \left[8.1\ \text{Wmm}^{-2}\text{atm}^{-2} \cdot \left(1 - x_{H_2O}\right) + 195\ \text{Wmm}^{-2}\text{atm}^{-2} \cdot x_{H_2O}\right] \tag{5.12}$$

Herein, x_{H2O} is the volumetric concentration of water. I_{sat} is plotted for a range of pressures and humidity in Figure 5.17. As expected for pressure broadened absorption lines, I_{sat} scales quadratic with pressure p since $\gamma^{\parallel}$ and Γ_0^{-1} are both directly proportional to p.

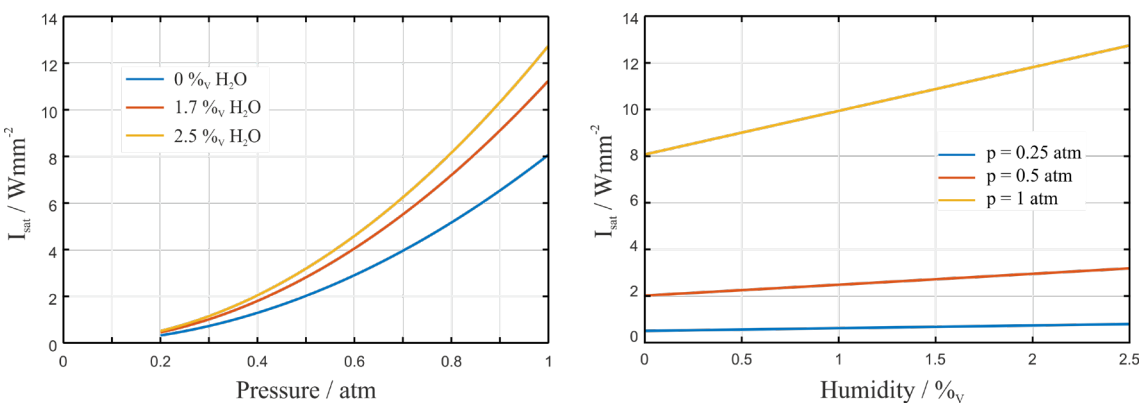

Figure 5.17. Saturation intensity calculated for varying pressure and humidity.

By fitting the absorption profile of CO shown in Figure 5.16 using equation (5.9) with $I_0 = 26$ Wmm^{-2} yields $I_{sat} = 1.2$ Wmm^{-2}. Inserting these values in equation (5.9) shows that the peak absorption coefficient is reduced to 0.14 α_0. Comparison with $I_{sat} = 0.72$ Wmm^{-2} obtained by inserting $p = 0.25$ atm and $x_{H2O} \approx 0.017$ in equation (5.12) shows fair agreement with the experiment, considering the simple assumptions of the used model and the potential errors of collision numbers taken from literature. In particular, diffusion is expected to be a significant effective relaxation pathway since the 1/e^2 – beam radius of 0.23 mm is relatively small. For a qualitative assessment of the influence of diffusion, one can calculate the probability distribution $\rho(r)$ for finding a molecule at a distance r from its initial position (*e.g.* the center of the beam) after $t = 1/\gamma^{\parallel}$ (the inverse collisional relaxation rate) and compare it to the beam profile. This is shown in Figure 5.18 for pressures from $p = 0.1$ atm to $p = 0.5$ atm. The probability distribution is given by (compare Einstein's theory of Brownian motion)

$$\rho(r,t) = \frac{1}{\sqrt{4\pi D t}} \exp\left(-\frac{r^2}{4D_{diff}t}\right) \tag{5.13}$$

Herein, $D_{diff} \approx p^{-1} \cdot 0.21\,\mathrm{cm^2 s^{-1} atm}$ is the diffusion coefficient of CO in air at 300 K. At pressures below ~ 300 mbar, the FWHM of ρ is comparable to the beam width, indicating that diffusion is a significant contribution to the overall relaxation rate. A detailed discussion of optical saturation in the presence of diffusion can be found in [180,181].

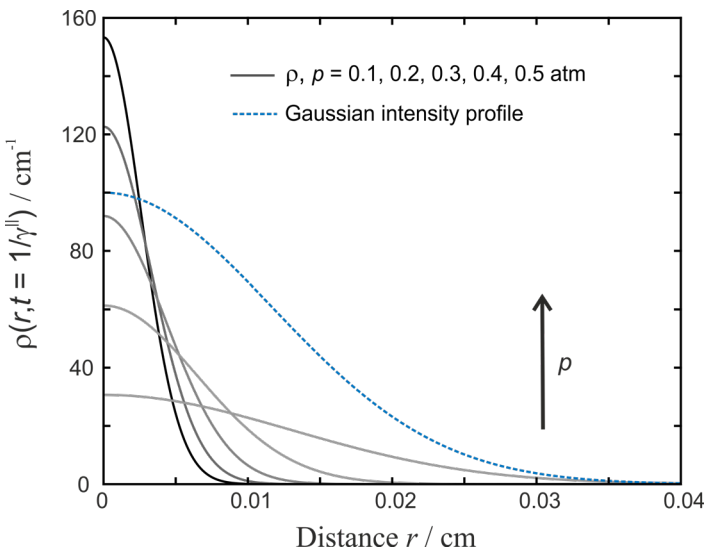

Figure 5.18. Diffusion of CO. Probability distribution $\rho(r,t)$ of finding a molecule at distance r after some time $t = 1/\gamma^{\parallel}$, plotted for varying pressure as indicated. The Gaussian beam profile of 0.23 mm 1/e^2 – radius is shown as a reference.

To confirm that saturated absorption is the source of the line-broadening observed in Figure 5.16, the saturation intensity I_{sat} was determined using the I-QEPAS signal recorded at varying laser power. The scaling of the I-QEPAS signal with power was investigated for 190 ppb CO in N_2 and 1.7 %$_V$ H_2O at 200 mbar and 500 mbar, respectively.

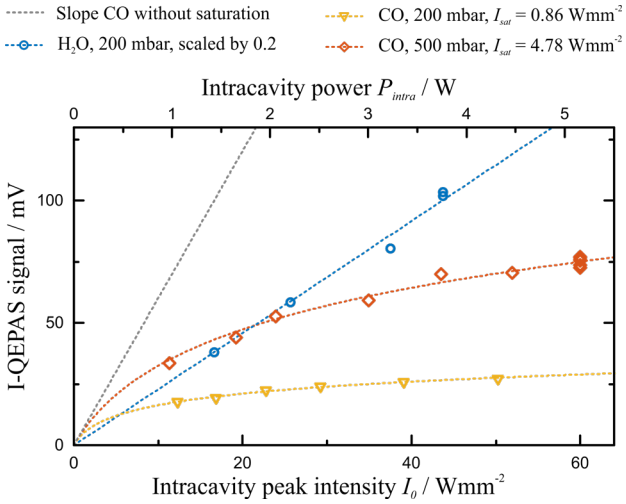

Figure 5.19. Scaling of I-QEPAS signals from CO (190 ppb) and H_2O (1.7 $\%_V$) with optical power. While H_2O shows the expected linear behavior, strong saturation is observed for CO.

To this end, the laser wavenumber was tuned to the absorption peaks of CO and H_2O, respectively. The beam was attenuated before entering the cavity via an iris and the optical power P_0 was measured using a power meter. The intracavity power was obtained by multiplying P_0 by the buildup factor and coupling efficiency retrieved in section 5.3.2. Figure 5.19 shows the recorded I-QEPAS amplitude as a function of intracavity power and intensity. The background signal from water vapor was subtracted for each CO - data point.

As in 2*f*-WM-QEPAS of CO without cavity enhancement (compare Figure 5.4), the signal from H_2O is directly proportional to optical power. In contrast, the recorded signals from CO show a strong influence of optical saturation. The observed trend of I-QEPAS signal Y with power P can be described using equations (3.8) and (5.9).

$$Y(I_0) = k_1 P \alpha(I_0) = k_1 \alpha_0 \frac{\pi}{2} w^2 I_{sat} \ln\left(1 + \frac{I_0}{I_{sat}} \bar{\Gamma}(\tilde{\nu})\right) \tag{5.14}$$

Herein, the peak intensity I_0 of the Gaussian mode of $1/e^2$ beam radius w is related to the measured power P via [51]

$$I_0 = \frac{2}{\pi w^2} P \tag{5.15}$$

In the center of the cavity, $w_0 = 0.234$ mm. For measurements taken at the absorption peak, the peak normalized line-shape function $\bar{\Gamma} = 1$.

To fit the experimental data using equation (5.14) and retrieve I_{sat}, the factor k_1 had to be determined separately rather than including it as a fitting parameter together with I_{sat}. Fitting of both parameters together yielded unsatisfyingly large confidence intervals due to the large collinearity of I_{sat} and k_1. The factor k_1 was determined using 2*f*-WM QEPAS

measurements with known optical power P_0 and absorption coefficient α_0 and the same beam radius $w_0 = 0.234$ mm. The 2*f*-WM QEPAS signal is given by

$$Y_{2fQEPAS} = \frac{0.342}{0.5} k_1 P_0 \alpha_0 \tag{5.16}$$

The pre-factor accounts for the different amplitudes observed in 2*f*-wavelength modulation and intensity modulation. The factor 0.342 corresponds to the Fourier component of a peak normalized Lorentzian profile at the second harmonic and optimum modulation amplitude at resonance [182]. The factor 1/0.5 corresponds to the fraction of intracavity optical power in the first harmonic as determined from experiment (compare Figure 5.11). With $k_{1,500mbar} = 2.7 \cdot 10^9$ V cm W^{-1} and $k_{1,200mbar} = 3.5 \cdot 10^9$ V cm W^{-1} determined from 2*f*-WM QEPAS measurements of 20 ppm of CO (compare section 5.1.2), fitting of the data in Figure 5 yielded saturation intensities of 4.78 [4.57; 4.98] W mm^{-2} and 0.86 [0.84; 0.88] W mm^{-2} for $p = 500$ mbar and $p = 200$ mbar, respectively (90 % confidence interval in angled brackets). Comparison with $I_{sat} = 2.8$ W mm^{-2} and $I_{sat} = 0.44$ W mm^{-2} calculated for $p = 0.5$ atm and $p = 0.2$ atm, respectively, using equation (5.12) again yields underestimated values as compared to the experiment.

From the fit of experimental data, the expected signal in absence of saturation ($I_{sat} \rightarrow \infty$) can be calculated (compare Figure 5.19, slope without saturation). The photoacoustic signals measured for maximum optical power and $p = 200$ mbar and $p = 500$ mbar are strongly influenced by saturation and correspond to 5.2 % and 18 %, respectively, of the calculated non-saturated signal. Assuming an effective two-level model for CO analogous to [179], the population of the vibrational ground state can be estimated (compare equation (32) in [179]). For I_{sat}(500 mbar) = 4.78 W mm^{-2} and $I_0 = 73$ W mm^{-2}, the ground state population in the center of the beam ($r = 0$) and at $r = w_0$ is depleted to 53 % and 66 %, respectively, of its equilibrium value, close to the fully depleted value of 50 %.

To validate the saturation intensities retrieved from I-QEPAS measurements, CRD measurements were performed for 95 ppb CO in N_2 and 1.7 %$_V$ H_2O at 200 mbar and 500 mbar, respectively, at the CO resonance wavelength. To retrieve I_{sat} from the CRD measurements, the absorption coefficient α was determined and compared to the expected linear absorption coefficient $\alpha_0 = 5.23 \cdot 10^{-6}$ cm^{-1} simulated based on the HITRAN2012 database [18,89]. The background absorption from H_2O and the empty cavity losses were measured and subtracted for both pressure levels to obtain α of CO. For a collimated Gaussian beam, I_{sat} can be retrieved directly by inserting α, α_0 and $I_0 = 73$ Wmm^{-2} in equation (5.9) and solving numerically for I_{sat}. Here, however, due to the close to concentric cavity design, the width w of the Gaussian mode changes significantly along the cavity axis z. Hence, $\alpha(z)$ must be integrated over the cavity length to obtain the effective value of α as measured by CRDS.

$$\alpha = \frac{\alpha_0}{L_{cav}} \int_{-L_{cav}/2}^{L_{cav/2}} \frac{I_{sat}}{I_0(z)} \ln\left(1 + \frac{I_0(z)}{I_{sat}} \bar{\Gamma}(\tilde{\nu})\right) \mathrm{d}z \tag{5.17}$$

Herein, $I_0(z)$ is given by equation (5.15) and (2.6). Note that equation (5.17) is valid for describing a single exponential decay from a CRDS experiment only if the population of the excited- and ground state (the "saturation") remain constant during a ring-down. For fast relaxing molecules, the populations follow the exponentially decaying intensity in the cavity at any time ("adiabatic regime"), yielding a variation of α with t and a more complex, non-exponential decay function [183]. In CO, the molecular relaxation rate $\gamma^{\parallel}$ is ~ 130 kHz and 52 kHz at 500 mbar and 200 mbar, respectively (compare equation (5.11)), which is an order of magnitude smaller than the inverse ring-down time of ~1.9 MHz. Hence, the populations can be considered constant during the ring-down and the decay can be described by a single exponential function. The molecular absorption coefficient α during the ring-down corresponds to the saturated value for the intensity present at the initiation of the ring-down, given the intensity was constant for long enough (>> $1/\gamma^{\parallel}$) for the populations to reach their steady state values. As can be seen from Figure 5.13, this was the case for the discussed experiments due to the low ramping frequency and the stability of intracavity power enabled by OF locking. Without stable laser locking, the saturation varies between consecutive ring-downs depending on the "history" of intracavity intensity before the ring-down (compare Figure 6.6), causing significant noise and errors.

To retrieve the saturation intensity I_{sat} given implicitly in (5.17) from the CRD measurements of α, Newton's method was used to solve numerically for I_{sat}. With $P = 6.3$ W, $w_0 = 0.234$ mm, $\bar{\Gamma}(\tilde{\nu}) = 1$ and the measured absorption coefficients of $\alpha = 2.52 \cdot 10^{-6}$ cm^{-1} and $\alpha = 1.13 \cdot 10^{-6}$ cm^{-1} for 500 mbar and 200 mbar, respectively, the found saturation intensities are $I_{sat} = 5.8$ Wmm^{-2} and $I_{sat} = 1.3$ Wmm^{-2}. Both values are significantly larger than those obtained via I-QEPAS as well as calculated values for I_{sat}. In the current experimental setup, the low vertical resolution of 8 bit and low data-transfer rate of the oscilloscope used to record ring-downs limit the quality of CRD measurements and the number of ring-downs that can be acquired and averaged. Furthermore, only a small fraction of the back-reflected light from the cavity impinges on the detector. Therefore, further measurements and improvements on the experimental setup are necessary to decrease the uncertainty of the retrieved saturation intensities and provide a quantitative comparison of the values for I_{sat} obtained via I-QEPAS and CRDS.

5.3.5. Sensing of CO under Saturated Absorption

Saturated absorption was reported and discussed in PAS measurements in a number of publications and sensitive measurements were demonstrated in this regime [177,178,184]. Although operating in a saturated regime, linearity with the concentration of the target gas is still given as long as the optical power is not significantly reduced by absorption of

the gas, which usually is the case in PAS [177]. On the contrary, the power inside high finesse cavities decreases with increasing absorption (compare section 2.2) [78,185], causing a non-linear scaling of signals with concentration.

To investigate the influence of saturation on the retrieval of CO concentrations in I-QEPAS and to characterize the performance of the setup, a series of calibration measurements was performed. For these measurements, the laser wavelength was locked to a cavity resonance and the cavity resonance wavelength was tuned to the peak of the absorption line of CO at 2179.77 cm^{-1}. Measurements were performed at 500 mbar and the concentration x of CO in N_2 and 1.7 $\%_V$ H_2O was varied from 0 ppb to 1500 ppb (x between 300 ppb and 700 ppb could not be prepared from the available gas standards). The integration time per data point was 120 s. The results are shown in Figure 5.20. For $x > 300$ ppb, the sensitivity dY/dx of the I-QEPAS signal decreases (circles in Figure 5.20). This is due to a decrease in intracavity power P_{intra} caused by absorption by CO [167] (increasing losses αL in equation (2.20)). To correct for this, P_{intra} was measured for each concentration using the demodulated detector signal and the known value $P_{intra} = 6.3$ W for $x = 0$ and the results are shown in Figure 5.20. Normalization by the demodulated detector signal, which corresponds to P_{intra}, yields an increase in sensitivity of the normalized I-QEPAS signal at high concentrations (diamonds in Figure 5.20). This is due to the decrease of the degree of optical saturation I_0/I_{sat} and corresponding increase of α (compare equations (5.8), (5.9)) with decreasing intracavity intensity I_0.

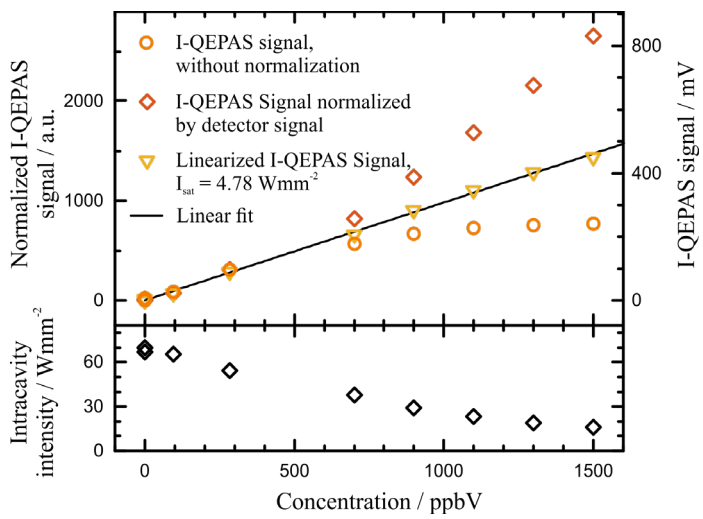

Figure 5.20. Calibration of CO in humidified N_2 at 500 mbar and 1.7 $\%_V$ H_2O. For high concentrations x, strong absorption leads to a decrease in power buildup and reduced I-QEPAS signal (orange circles). On the contrary, the slope dY/dx of power normalized I-QEPAS signal (red diamonds) increases at high concentrations due to the absorption related decrease of intensity (lower panel) and hence decreased optical saturation. By correcting for both, intracavity power and saturation using equation (5.18), a linear calibration is obtained (yellow triangles).

Based on equation (5.9), the recorded normalized I-QEPAS amplitude $Y_{norm}(x)$ can be linearized using

$$Y_{norm,lin}(x) = Y_{norm}(x)\frac{I_0(x)}{\ln\left(1+\frac{I_0(x)}{I_{sat}}\right)} \tag{5.18}$$

Figure 5.20 shows the scaled linearized I-QEPAS amplitude $Y_{norm,lin}$ calculated for I_{sat} = 4.78 W mm^{-2} as retrieved in section 5.3.4.

To demonstrate the capability of the setup for high sensitivity measurements of CO in a strongly saturated regime (I_0 = 73 W mm^{-2} = 15 I_{sat}), calibration curves were recorded from 0 to 95 ppb and 0 to 19 ppb (compare Figure 5.21, experimental conditions identical to Figure 5.20). For these small concentrations, no linearization of normalized I-QEPAS signals was necessary since I_0 does not change sufficiently to influence α. The background signal at 0 ppb originates from the tail of the absorption line of water at 2178.90 cm^{-1}.

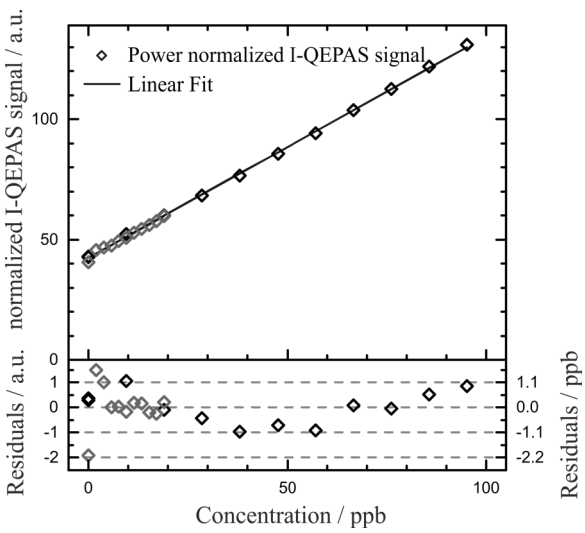

Figure 5.21. Calibration of CO in humidified N_2. Gray and black data points correspond to measurements performed on different days.

5.3.6. Performance of I-QEPAS for CO Sensing

To characterize the sensing performance of the setup under saturated absorption as well as under linear absorption conditions we use the absorption lines of CO and H_2O and compare the results obtained for I-QEPAS with those of 2*f*-WM QEPAS. The noise floor of both QEPAS measurements is determined from Allan variance analysis. An Allan–Werle plot [41] for the I-QEPAS signal recorded at conditions identical to the calibrations presented above, *i.e.* 1.7 ‰$_V$ water in N_2 at 500 mbar, in the absence of CO is shown in Figure 5.22. The noise floor up to ~ 80 s integration of 0.76 mV Hz$^{-1/2}$ was dominated by noise of the tuning fork (thermal noise) and was identical for I-QEPAS and 2*f*-WM QEPAS of both, H_2O and CO.

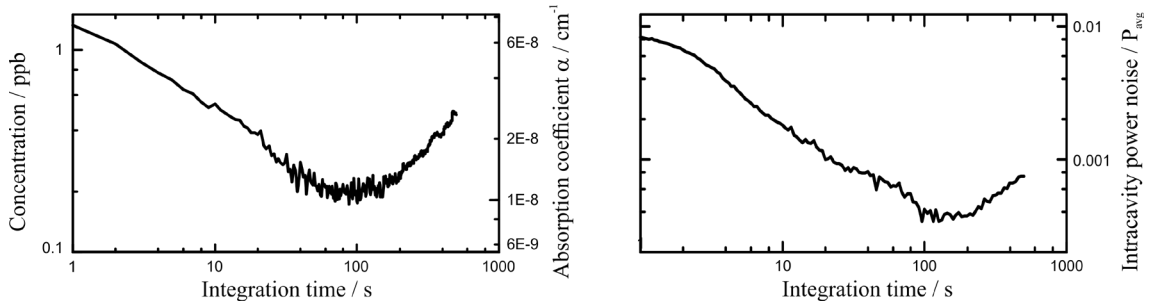

Figure 5.22. Allan-Werle plot recorded for humidified N_2. Left: Allan deviation of normalized I-QEPAS signal, expressed as concentration of CO, and corresponding peak linear absorption coefficient α of CO at 2179.77 cm^{-1}. Right: Allan deviation of demodulated detector signal, representing intracavity power.

Additional potential drifts, limiting the Allan deviation at integration times larger than 100 s, may arise from small changes in water concentration, and hence background signal, and from temperature changes affecting the resonance frequency of the tuning fork. From the calibration shown in Figure 5.21, the sensitivity for CO detection is 0.369 mV ppb^{-1} for I-QEPAS and $6.64 \cdot 10^{-3}$ mV ppb^{-1} for 2*f*-WM QEPAS (calibration not shown). From a one-point calibration, the sensitivity of I-QEPAS and 2*f*-WM QEPAS for H_2O at 2178.90 cm^{-1} was found to be 29.7 µV ppm^{-1} and 0.13 µV ppm^{-1}, respectively.

The corresponding noise equivalent concentrations (NEC), noise equivalent absorptions (NEA) and power normalized NEAs (NNEA) of I-QEPAS and 2*f*-WM-QEPAS are summarized in Table 2. Also, the gain in signal to noise ratio (SNR) from I-QEPAS as compared to 2*f*-WM QEPAS is given. The figures of merit for CO detection are adversely influenced by optical saturation as well as slow V-T relaxation [120,186]. However, despite strong optical saturation, the sensitivity is increased by a factor of 57 as compared to 2*f*-WM QEPAS without power enhancement. The full potential of cavity enhancement for PAS in absence of optical saturation is evident from the gain in SNR of 230 obtained for H_2O, which agrees well with the power enhancement of about 250 found above.

Table 2. Figures of merit of I-QEPAS compared with 2*f*-WM QEPAS for sensing of CO and H_2O. NEA and NNEA are calculated from NEC using NEA(CO) = NEC·$5.5 \cdot 10^{-8}$ cm^{-1} ppb^{-1}, NEA(H_2O) = NEC·$1.7 \cdot 10^{-13}$ cm^{-1} ppb^{-1}; NNEA(CO) = NEA·25 mW, NNEA(H_2O) = NEA·16 mW.

	NEC		**NEA**		**NNEA**		**SNR gain**	
Unit	[ppb $Hz^{-1/2}$]		[10^{-6} cm^{-1} $Hz^{-1/2}$]		[10^{-9} cm^{-1} W $Hz^{-1/2}$]			
	CO	H_2O	CO	H_2O	CO	H_2O	CO	H_2O
I-QEPAS	2.1	2590	0.11	0.0044	2.8	0.07	57	230
2*f*-WM QEPAS	114	$5.8 \cdot 10^6$	6.3	0.99	160	16		

From the same measurement of humidified N_2 discussed above, an Allan variance analysis of the demodulated detector signal, normalized by its mean value, was performed (see Figure 5.22, right panel). This represents the noise of the intracavity power P and translates directly to the relative uncertainty of a measurement in absence of all other noise sources. The noise floor of P/P_{avg} of $5.7 \cdot 10^{-3}$ $Hz^{-1/2}$ is large compared to the laser noise, but low compared to typical measurements with high finesse cavities and free running lasers [135]. The low intracavity power noise is a distinct feature of the optical-feedback locking technique and is commonly exploited in optical feedback cavity enhanced absorption spectroscopy (OF-CEAS) [128].

5.3.7. Conclusions

A mid-IR intracavity QEPAS spectrometer was set up. A number of considerations with regard to the design and operation of QEPAS and PAS inside high finesse cavities were discussed that lead to the Brewster window cavity design ultimately realized in the laboratory. The experimental setup and its operational principles based on optical feedback locking of a QCL to the Brewster window cavity were presented in detail. By optimizing the reflectivity of the Brewster window ("optical impedance matching"), a nominal power enhancement of 312 of the cavity was realized. The experimentally determined intracavity power enhancement was 252, which is close to the calculated value of 312 due to the highly efficient laser-cavity coupling facilitated by optical feedback. The high level of intracavity power of 6.3 W and intensity of 73 W mm^{-2}, respectively, lead to strong optical saturation of CO. Theory describing photoacoustic signals under saturated absorption in a Gaussian beam was presented. On this basis, the saturation intensity of the R9 transition of CO in humidified N_2 at 500 mbar and 200 mbar was retrieved from the power dependence of the I-QEPAS signal. The obtained saturation intensities were compared with those obtained from CRDS measurements as well as saturation intensities calculated based on the molecular relaxation model of CO introduced in section 5.2.1. The values from I-QEPAS measurements agree to within a factor of two with those obtained from CRDS and simulations. Using the retrieved saturation intensity allowed linearization of a calibration curve affected by varying degrees of optical saturation, which was caused by changes in optical power inside the high finesse cavity. This demonstrates that, with the presented quantitative description of photoacoustic signals und saturated absorption, highly sensitive and accurate trace gas sensing can be performed in this regime. To illustrate why increasing the optical power beyond the linear absorption regime is useful, it is worth considering a simple example. Assuming one would limit the intensity to a linear regime, *e.g.* to $I_0 < \frac{I_{sat}}{50}$ such that $\alpha > 0.99\ \alpha_0$ (compare equation (5.9)), the sensitivity would be ~ 140 times smaller than that obtained for $I_0 = 73$ W mm^{-2} and $I_{sat} = 4.78$ W mm^{-2}, corresponding to the measurements presented above (compare equation (5.14)). Therefore, despite the

necessity of correcting for the non-linear sensor response, operating in the non-linear regime significantly improves the sensitivity.

The sensitivity of I-QEPAS measurements of CO and H_2O was compared to 2*f*-WM QEPAS measurements without power enhancement. For the non-saturated transition of H_2O, the expected increase in SNR of 230 was found, very close to the power enhancement. Although the gain in sensitivity for CO is limited by saturation, the SNR was increased by a factor of 57, demonstrating that the sensitivity of PAS can be increased despite leaving the regime of linear absorption of the analyzed molecule.

6. Frequency-Locked Cavity Ring-Down Faraday Rotation Spectroscopy

The combination of cavity ring-down and Faraday rotation spectroscopy [150] (CRD-FRS, compare section 4.3) encodes spectroscopic information in the difference in decay times for two orthogonal polarization states [9,149]. Since these polarization states experience almost identical non-sample related losses, they cancel in the differential measurement, which allows obtaining the round-trip Faraday-rotation angle and hence the molecular concentration from a single cavity ring-down event. Off-resonance measurements, that are necessary in CRDS to determine the non-sample related losses, are redundant in CRD-FRS, which enables continuous line-locked operation without the need for spectral scanning. In addition, many of the disadvantages of line-locked operation of spectroscopic detection systems are avoided by cavity ring-down Faraday rotation spectroscopy (CRD-FRS). This is due to: 1) the insensitivity of the technique to diamagnetic species, which infers that CRD-FRS is largely immune to spectral interference from other common sample constituents, 2) its ability to directly modulate the optical properties of the sample via the magnetic field, which allows for efficient decoupling of the signal from optical fringes that often limit stable operation and long-term performance in absorption CRDS systems [187], and 3) the fact that non-sample related losses, such as particle scattering that affect cavity finesse, are largely correlated for the two polarizations, which makes CRD-FRS insusceptible to shot-to-shot fluctuations. All this makes CRD-FRS an ideal candidate for high duty cycle line-locked operation.

Here, frequency-locked CRD-FRS measurements of O_2 are presented. The experimental setup is discussed in section 6.1. To enable the recording of ring-downs at a rate of up to 9 kHz, the laser was locked to the cavity via the PDH technique. To increase the stability

of the lock as well as the optical throughput of the cavity, the diode laser was equipped with an external cavity to reduce its frequency noise. The cavity resonance frequency was locked to a molecular resonance of O_2 based on frequency modulation. Data analysis is briefly discussed in section 6.2 and measurements of O_2 are presented in section 6.3. By comparing CRD-FRS measurements with opposite orientation of the magnetic field, background signals from mirror-birefringence were removed and O_2 – concentrations could be retrieved in line-locked operation without any off-resonance measurement. The influence of Faraday rotation during cavity buildups in measurements of high concentrations of O_2 is analyzed. The performance of the frequency locked CRD-FRS setup is quantified and compared to previously published results on CRD-FRS. The chapter is closed by some concluding remarks in section 6.4.

Parts of the work presented in this chapter were published in [9].

6.1. Experimental Realization of a Frequency Locked CRD-FRS Spectrometer

The setup depicted in Figure 6.2 builds on the optical setup described in [150] (compare section 4.3) with three important expansions: a frequency modulation spectroscopy (FMS) based locking branch to lock to the absorption peak of the $^{P}P_3(3)$ transition at 13112 cm^{-1} in the oxygen A-band; a PDH locking branch to lock the laser wavelength and the cavity resonance frequency; and the new cavity enclosure and solenoid coil circuit that enables switching of the orientation of the magnetic field.

A Faraday isolator was used to suppress unwanted optical feedback to the external cavity diode laser. Emitted light was phase modulated at $f_{PDH} = 25$ MHz using an electro-optic phase modulator (EOM, EO-PM-R-25-C1, *Thorlabs*). Phase modulation was exploited for both, the FMS locking branch and the PDH locking branch. The FMS locking branch was realized by splitting 30% of the optical power and detecting the light transmitted through an astigmatic Herriot type multi-pass gas cell filled with ambient air at 100 mbar at a photodetector (PD4).

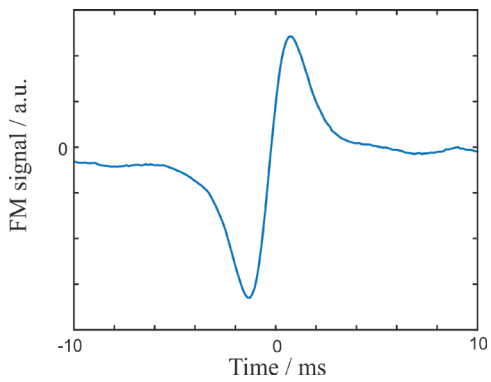

Figure 6.1. FMS error signal obtained when scanning the wavelength of the phase modulated laser across the targeted absorption line of O_2 (100 mbar in ambient air).

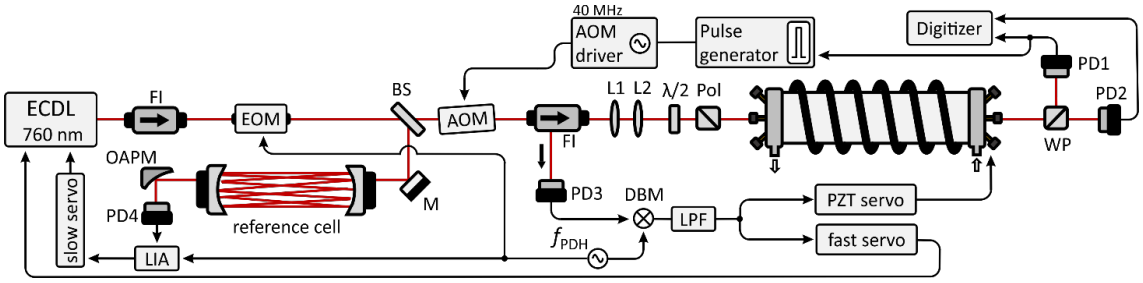

Figure 6.2. Setup, see text. ECDL: external cavity diode laser, FI: Faraday isolator, EOM: electro-optic phase modulator, BS: beam splitter, AOM: acousto-optic modulator, L: lens, λ/2: half-wave plate, Pol: polarizer, WP: Wollaston Prism, PD: photodiode, DBM: double balanced mixer, LPF: low pass filter, M: mirror, OAPM: off-axis parabolic mirror, LIA: lock-in amplifier

The signal from PD4 was demodulated at f_{PDH} by a fast lock-in amplifier (HF2LI, *Zurich Instruments*) to yield the error signal shown in Figure 6.1 [188]. The demodulated FMS signal was input to a slow PI loop (~5 Hz, 3 dB bandwidth) realized using the internal PID controller of the lock-in amplifier. The PI loop acted on the length of the external cavity of the laser via the piezo actuator and a piezo controller (MDT693B, *Thorlabs*) to keep the error signal at zero, *i.e.* the laser wavelength at the center of the absorption line. The other 70% of laser light was deflected by an AOM and coupled to the high-finesse cavity via two plano-convex mode-matching lenses. A second Faraday isolator (IO-5-780-HP, *Thorlabs*) equipped with polarizing beam splitters as in- and out-coupling polarizers was used to guide the back-reflected light from the cavity to a detector PD3 for PDH-locking. To demodulate the signal from PD3 and obtain the PDH error signal, the signal was mixed in a double balanced mixer (Mini-circuits) with a phase-adjusted replica of the local oscillator from a two-channel signal generator and low-pass filtered subsequently (3 dB at 2.5 MHz). The obtained error signal was input to two PID loops running on a digital laser locking module (DigiLock 110, *TOPTICA Photonics Inc.*) to lock the laser-wavelength and cavity resonance frequency. The first PID loop provided a fast feedback to the laser current, whereas the second PID created a slower feedback loop that acted on the cavity length through a piezo actuated mirror mount (*CRD-optics*). The bandwidth of the first PID was high-pass limited to frequencies > 400 Hz to prevent mutual accumulation of DC-offsets of the PIDs [57].

A half wave plate and a linear polarizer set the input polarization for the high finesse cavity. The cavity finesse of $F = 5{\cdot}10^4$ was determined from the cavity length $L_{cav} = 30$ cm and the empty cavity ring-down time $\tau_0 = 16.1$ µs (compare equations (2.13) and (2.32)). A 25 cm long solenoid generated a uniform magnetic field of approximately 400 Gauss inside the cavity. The solenoid was driven by a DC power supply in an H-bridge configuration to allow for switching the polarity of the supply current and hence the direction of the magnetic field. To avoid Eddy currents during switching, the cavity was custom-made from low permeability, non-conducting polymer material (Delrin, *DuPont*).

Light transmitted through the cavity was split by a Wollaston prism and detected with two avalanche photodiodes (APD, APD120A, *Thorlabs*). The signal from one of the APDs was used to trigger pulses that shut down the AOM for 60 µs as soon as a threshold level was reached. The initiated ring-down events were acquired at 10 MS/s using a 16-bit digitizer (FCIX Razor, *Gage Applied*).

The DBR - diode laser (Cheetah, *Sacher Lasertechnik*) used in the previous setup [150] could not be stabilized to the cavity using PDH locking. When the free-running phase modulated DBR – diode laser was scanned across a cavity resonance, the PDH error did not exceed the noise floor. This can be understood from the large mismatch between the linewidth of the diode laser (~ 2 MHz, 1 ms) and the FWHM of the cavity resonances (10 kHz). As was discussed in section 2.4.1, a common approach in locking diode lasers to high finesse cavities is to reduce the laser frequency noise of the diode laser using an external cavity (EC) [57,65,189]. Here, a simple EC was constructed using a plane mirror to reflect a small fraction of the emitted light back into the laser (compare Figure 6.3) [190]. The feedback ratio was adjusted to ~ $2 \cdot 10^{-3}$ using a polarizer as a variable attenuator and the length of the EC was 18 cm. The mirror was mounted on a piezo element for adjusting the phase of the back-reflected light and thereby tune the EC-DLs wavelength. For locking the laser wavelength to the peak of the O_2 absorption line as described above, the mode-hop free tuning range accessible by varying the length of the EC alone was sufficient. For scanning the laser wavelength further, the laser current and cavity length were scanned synchronously. Figure 6.3 shows the cavity transmission detected using D1 in Figure 6.2 while scanning the laser wavelength across several FSRs of the high finesse cavity. With the EC in place, the peak transmission was increased by an order of magnitude as compared to the free-running DBR-diode laser.

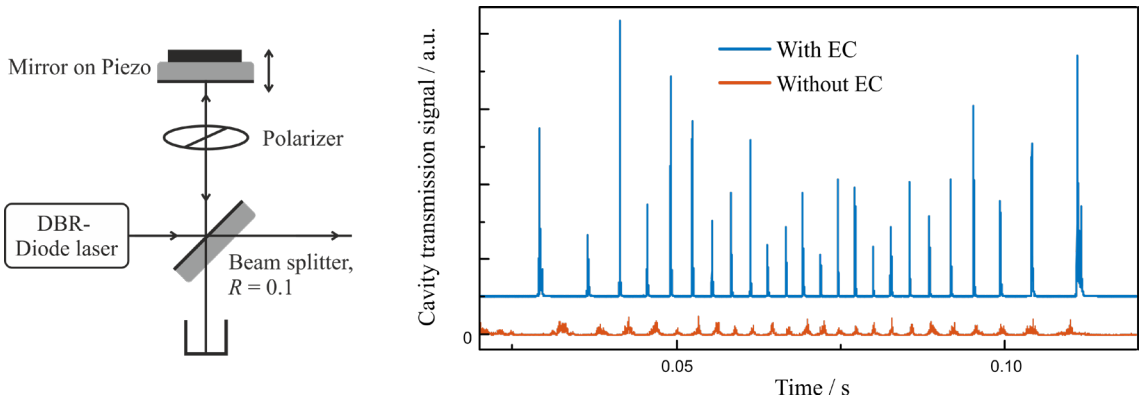

Figure 6.3. Left: External cavity (EC) modification used to decrease the frequency noise of the DBR-diode laser. Right: Transmission through the high finesse cavity recorded while sweeping the laser wavelength across several FSRs of the cavity with and without the EC. Signal "With EC" offset for better visibility.

Also, with the EC, the SNR of the PDH error signal was sufficient to achieve reliable locking of the laser. Figure 6.4 shows a series of ring-downs recorded while the laser was PDH-locked to the cavity. After each ring-down, the laser is rapidly tuned back into resonance and the next ring down is initiated. This allows recording up to 9000 ring-downs per second, which, at a down-time of 60 µs per ring-down, corresponds to a duty cycle of 9000 $s^{-1} \cdot 60$ µs = 54 %. Note that no measures were taken to pause or interrupt the operation of the PDH locking-loop during the ring-down events when no error-signal from the cavity is available.

Although the locking-loop reliably tuned the laser back into resonance after each ring-down, it was unable to retain a permanent lock to the cavity resonance when no ring-downs were initiated. Rather than being locked tightly to the cavity resonance, it was observed experimentally that the laser frequency repeatedly approached resonance, oscillated around the resonance at increasing frequency and tuned away from resonance again. A more detailed analysis of the amplitude- and phase response of the individual actuators (piezo-electric mirror mount and laser driving current) and matching of the gain curve of the feedback electronics to the actuators' response should allow establishing a permanent, tight lock [65]. For the experiments presented herein, however, this was not necessary and was not investigated further.

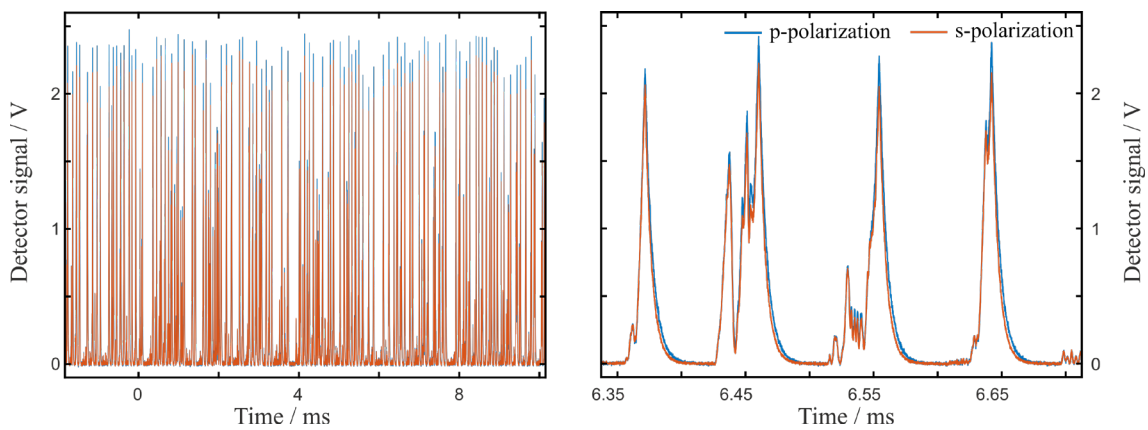

Figure 6.4. Series of ring-downs acquired during a measurement of 1 ‰$_V$ O_2 in N_2 in cavity- and line-locked operation. The two panels show sections of different length of the same measurement.

6.2. Data Analysis

A typical data set obtained for 1‰$_V$ of O_2 in N_2 at 112 mbar pressure acquired during a period of 0.8 s is shown in Figure 6.5 a) and b). Each ring-down was fitted individually by a three-parameter single exponential model and the round-trip rotation Θ is calculated from every pair of τ_s and τ_p using equation (4.7). During the acquisition, the direction of the magnetic field was flipped at 5 Hz, causing the sign of the Faraday rotation angle Θ_{FRS} to alternate accordingly while the sign of the mirror birefringence remains unchanged.

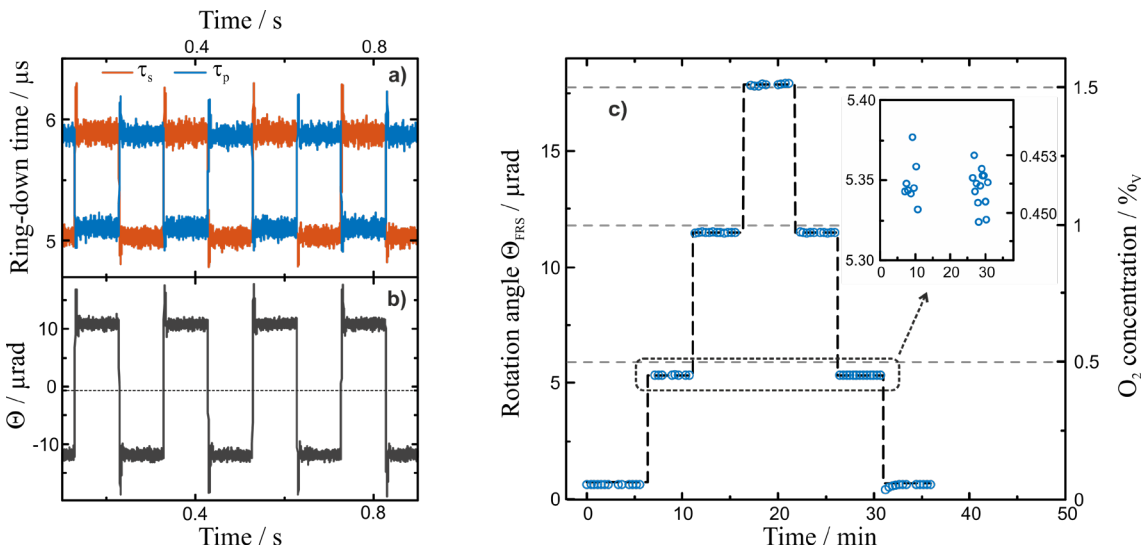

Figure 6.5. Data analysis and results. **a)** Fitted ring-down times for both polarization components and **b)** corresponding round trip rotation angle Θ for a measurement of 1 $\%_V$ O_2 in N_2 at 112 mbar pressure. Flipping of the magnetic field at 5 Hz changes the sign of Θ. The dashed line indicates mirror birefringence Θ_{MBF} = 0.76 µrad. **c)** Dilution series of O_2 in N_2. Inset: zoom around 0.5 $\%_V$. Each data point represents the average of ring-downs acquired during 0.8 s.

The round-trip rotation caused by mirror birefringence, Θ_{MBF} = -0.76 µrad, was determined by averaging the retrieved rotation angle over multiple periods of the magnetic field modulation. From the absolute mean rotations Θ^+ and Θ^- recorded for the two orientations of the magnetic field, the round-trip Faraday rotation angle $\Theta_{FRS} = (\Theta^+ + \Theta^-)/2$ was retrieved. Concentrations were calculated from Θ_{FRS} using a Faraday rotation model based on the HITRAN database [136].

6.3. Results

Figure 6.5c shows results obtained from ring-downs recorded during 35 minutes with steps in the O_2 concentrations obtained through N_2 dilution. Measurements were performed at 112 mbar and a flow rate of 0.2 L/min. Every data-point in Figure 6.5c represents the average from approximately 5700 ring-downs recorded during 0.8 s with the magnetic field flipped at 5 Hz.

The significant offset for 0 $\%_V$ originates from leakage of ambient air into the gas cell. The relative error of the retrieved concentrations (see Ref. [150]) as compared to those set by the gas mixer (Environics 4040) is on the several percent level. Besides leakage of ambient air, one potential source of error is the gas mixer unit operating outside its optimum range (attributed to uncertainty of the flow meters operating below 10 $\%_V$ of full scale flow required for dilution of the O_2 concentration of 23 $\%_V$ to a single percent level). Also, for high concentrations and correspondingly large rotation angles Θ, polarization rotation during the buildups moves the initial polarization angle at the beginning of the ring-down away from 45°.

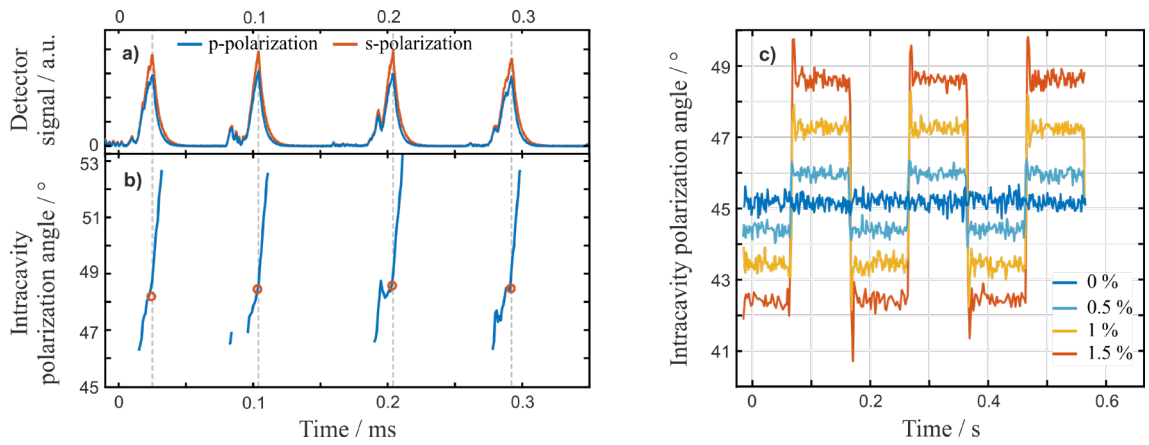

Figure 6.6. Intracavity polarization rotation during cavity buildups, measured for 1.5 $\%_V$ O_2 in N_2. a) Detector signals; b) Intracavity polarization angle (circles indicate initiation of ring-downs, only data-points for which the detector signals exceed a threshold value are shown); c) Intracavity polarization angle at the moment when ring-downs were initiated (moving average filtered, window size: 10 samples), recorded during measurements with flipped field and varying concentration of O_2 in N_2 as indicated.

Figure 6.6b shows the intracavity polarization angle during several buildups and ring-downs. To calculate the intracavity polarization angle with respect to the analyzer (Wollaston prism), the recorded detector signals I_s and I_p shown in Figure 6.6c were normalized by their mean values from several periods of field modulation to account for different amplification of the detectors.

Based on equation (4.5), the intracavity polarization angle was calculated as

$$\varphi := \arctan\left(\sqrt{I_s/I_p}\right) \tag{6.1}$$

From Figure 6.6b, a clear change of φ can be seen already before the ring-downs are initiated. This is equivalent to a deviation $\Delta\varphi_0$ of the uncrossing angle between polarizer and analyzer from 45°, that leads to an expected overestimation of the round-trip rotation angle Θ by a factor $1/\cos(2\Delta\varphi_0)$ (compare equation (23) in [150]). For the highest concentration of O_2 of 1.5 $\%_V$, $\Delta\varphi_0 = 3.6°$, which corresponds to a relative error of ~ 1 %. Since $\Delta\varphi_0$ effects Θ only to second order, the so introduced relative error rapidly decreases for smaller concentrations (0.3 % and 0.06 % for 1 $\%_V$ and 0.5 $\%_V$ of O_2, respectively). Further, the influence of the approximation of equation (4.5) by the purely exponential form (equation (4.6)) was tested by fitting the data using both equations. Despite the intracavity polarization angle deviates significantly from 45° (compare Figure 6.6b), for which the approximation is valid, no significant difference between the results from fitting of the exact and approximate equation were found.

Despite the errors between the set and retrieved concentrations, the high precision and stability of the system is evident from the reproducibility of the retrieved concentrations (inset of Figure 6.5c).

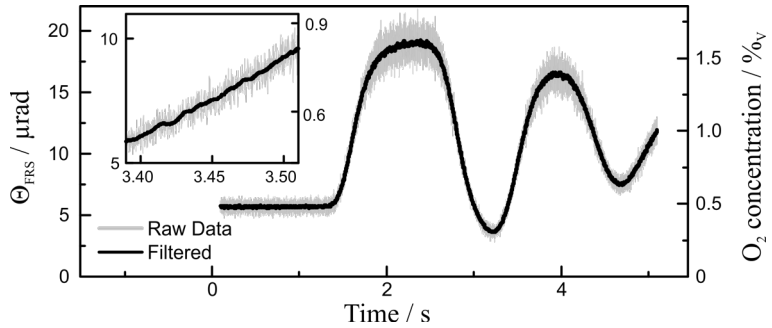

Figure 6.7. Concentration variations recorded via CRD-FRS. Concentrations are retrieved from every pair of ring-downs acquired at a rate of ~8.5 kHz. Filtering was performed using a Savitzky-Golay filter of ~ 110 Hz, 3 dB bandwidth. Note that the noise increases for high concentrations due to a reduced ring-down time associated with absorption of O_2. The zoom around 3.45 s illustrates the fast response time of the spectrometer.

Figure 6.7 shows data recorded while the concentration was randomly changed at the gas mixing unit from 0.5%v to 1%v. The magnetic field was not flipped during this experiment. With the line-lock and high ring-down rate, the response time of the spectrometer is mainly limited by the gas flow system.

Figure 6.8 shows an Allan-Werle plot calculated from 42000 pairs of ring-downs acquired during five seconds for N_2 flow. From this data, a noise equivalent angle $\Theta_{NE} = 2 \cdot 10^{-9}$ rad Hz$^{-1/2}$ is obtained. Since the line-lock allows for retrieving a value of concentration from every ring-down, this value can be directly converted to a noise equivalent O_2 concentration of NEC = 1.9 ppm Hz$^{-1/2}$. With a peak absorption coefficient of the targeted O_2 of $3.7 \cdot 10^{-10}$ cm^{-1} ppm^{-1} simulated based on the HITRAN database [18], the noise equivalent absorption coefficient is $7.0 \cdot 10^{-10}$ cm^{-1} Hz$^{-1/2}$.

The value of Θ_{NE} is similar to previously reported results, which were measured with a longer cavity, but lower effective ring-down rate a lower cavity transmission due to higher frequency noise of the DBR-diode laser [150].

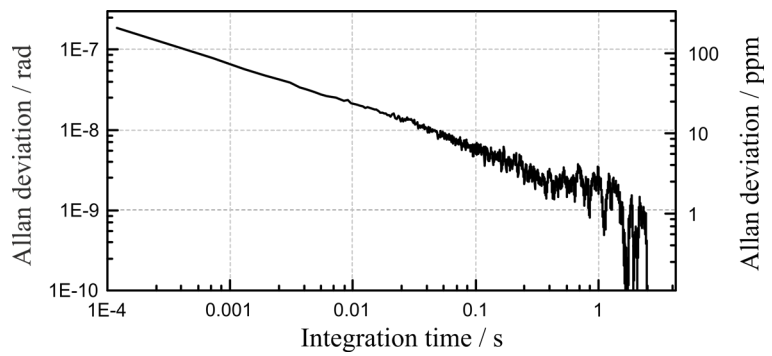

Figure 6.8. Allan-Werle plot from five seconds acquisition with N_2 as sample.

The expected reduction of Θ_{NE} can be estimated based on the experimental differences to ref. [150] and are summarized in Table 3. The effect of the increased cavity transmission associated with the reduced frequency noise of the external diode laser (compare Figure 6.3) on the signal to noise ratio depends on the origin of the noise overlying the recorded intensities (detector dark noise, SNR ~ P; shot-noise, SNR ~ $P^{1/2}$, vibrations and other cavity noise, SNR = constant). Since the noise floor was not characterized, the increase in SNR can only be roughly estimated. Together with the decreased cavity length and the increased rate of ring-down acquisitions, an SNR gain between 4 and 18 can be roughly estimated. Unfortunately, an experimental flaw that was identified only after the measurements had been finished prevented the observation of improvements on this order. The bandwidth (3 dB) of the detectors used in this work of ~ 50 MHz was much larger than the used sampling rate of 10 MHz of the digitizer, which leads to an aliasing of noise at frequencies around 5 MHz, 10 MHz, … onto the frequency range of the ring-down signals. Since the detector noise floor is flat up to 50 MHz according to the data-sheet, the detector noise in the presented measurements is expected to be approximately ten times higher than what would be obtained if the signals had been low-pass filtered to ~ 2 MHz, which most likely explains the unexpectedly high Θ_{NE}.

Table 3. Estimated expected increase of signal to noise ratio of the current setup as compared to ref. [150].

Parameter	**Change relative to** [150]	**SNR gain**
Cavity length	Decreased to 0.3 m from 0.5 m	$\sqrt{0.3/0.5} = 0.77$
Repetition rate of ring-downs	Increased to 9 kHz from 1 kHz	$\sqrt{9/1} = 3$
Transmitted intensity due to reduced laser frequency noise	Increased by factor ~ 10 (see Figure 6.3)	~ 2 – 8, see text
Under-sampled ring-down acquisition	Too high detection bandwidth	< 1

6.4. Conclusions

A line- and cavity-locked CRD-FR spectrometer was set up and employed for measuring oxygen concentrations at ring-down rates of up to 9 kHz. The combination of CRDS and FRS in line-locked operation enables retrieval of sample concentration information from every ring-down event, independent of the empty cavity ring-down time, circumventing the need for off-resonance measurements. While wavelength scanning is still necessary in CRD-FRS if the absorption line shape is unknown or varies over time (with pressure, temperature or matrix composition), line-locked CRD-FRS measurements are unaffected by fluctuations of cavity-losses, optical fringes and varying spectral backgrounds. The high repetition rate permitted by employing PDH–locking to the cavity together with active

line-locking to the resonance of the molecular transition allowed for assessing quickly changing sample concentrations on a millisecond timescale. The noise equivalent round-trip rotation angle $\Theta_{NE} \sim 2 \cdot 10^{-9}$ rad $Hz^{-1/2}$ was limited by excess detector noise originating from under-sampled ring-down digitization. The stability of the system was demonstrated by measurements repeated over 30 minutes. The insensitivity to optical fringes and other system drifts achieved through the ability to directly modulate the sample response by magnetic field manipulation holds promise for extremely precise and sensitive trace gas measurements of paramagnetic species with high temporal resolution. Furthermore, the immunity to rapidly occurring fluctuations of the empty cavity ring-down time makes the technique highly suited for open cavity applications, where particulate matter contamination introduces severe intensity noise by drastically affecting the cavity losses.

7. Future Developments in Intracavity Photoacoustic and Photothermal Spectroscopy

Based on the experimental setup and results presented in section 5.3 for I-QEPAS using a Brewster window cavity, a number of measures can be identified to improve upon the existing setup.

7.1. Optimization of the I-QEPAS Setup

An immediate improvement in the SNR can be expected from exchanging the resonator tubes of the QEPAS module (compare section 5.1). The measured signal increase of a factor of six between measurements with and without resonator tubes (bare quartz tuning fork) is significantly smaller than values of ~ 15 to 25 typically reported [122]. This can be attributed to the length of the resonator tubes of 12.45 mm that is significantly larger than the expected optimum length of ~ 9.6 mm calculated using equation (3.9). Unfortunately, this flaw was only realized after all measurements had been finished.

Besides increasing the signal using optimized resonator tubes, the noise floor of measurements should be investigated and reduced. Intracavity power noise quantified to $\Delta P/P_{avg} = 0.57$ % $Hz^{-1/2}$ represents a significant source of noise that (ΔP denotes deviations from the average value of P, *i.e.* P_{avg}). The noise in the I-QEPAS signal Y arising from intracavity power noise is directly proportional to Y and $\Delta P/P_{avg}$ (compare equation (3.8)). For example, the background absorption from water in the CO calibration shown in Figure 5.21 is equivalent to the signal from 44 ppb of CO, which yields a noise floor due to intracavity power noise of 44 ppb $\cdot 5.7 \cdot 10^{-3}$ $Hz^{-1/2}$ = 0.25 ppb $Hz^{-1/2}$. Figure 7.1 (left) shows the detector signal, corresponding to intracavity power, and I-QEPAS signal recorded during a measurement of 98 ppb of CO in humidified N_2. Both signals were normalized by their time averaged values.

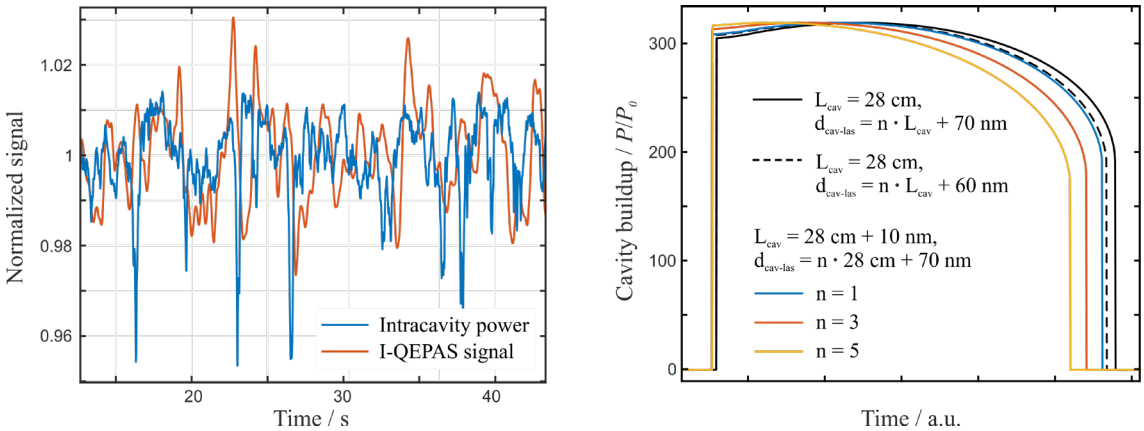

Figure 7.1. Left: Intracavity power and I-QEPAS signal, both normalized by their mean value, recorded during a measurement of 98 ppb of CO in humidified N_2. Right: Simulated cavity buildups under optical feedback with different cavity-lengths L_{cav} and laser-cavity distance $d_{cav\text{-}las}$, simulating the impact of mechanical vibrations, see text.

The intracavity power frequently drops by up to 5 %, and a correlation between these drops and the I-QEPAS signal can be observed. Likely causes for excess intracavity power noise are mechanical vibrations or turbulent air flow disturbing the optical feedback phase. Figure 7.1 (right) shows simulated buildups under the influence of varying cavity length L_{cav} (vibration of the cavity) and laser-cavity distance $d_{cav\text{-}las}$ (vibrations of optical elements between laser and cavity). The solid black line corresponds to the reference situation without vibrations. The dashed solid line refers to a fluctuation of $d_{cav\text{-}las}$. Note that the observed buildup for a given displacement of $d_{cav\text{-}las}$ is independent from the choice of $d_{cav\text{-}las}$ as a multiple n of L_{cav} (identical for $n = 1, 2, \ldots$). The colored lines simulate the effect of a small change in L_{cav} for $d_{cav\text{-}las}$ chosen as a varying multiple of L_{cav}. As can be seen from the simulations, the influence of a small variation of the cavity length increases with increasing laser-cavity distance. This is because variations of L_{cav} shift the resonance frequency of the cavity by $\Delta\tilde{\nu}_{res}$, and the resulting change of optical feedback phase $2\pi\Delta\tilde{\nu}_{res}d_{cav-las}$ scales with $d_{cav\text{-}las}$. As a consequence, to reduce the influence of vibrations and turbulent gas flow in the cavity, the laser-cavity distance should ideally be reduced from $d_{cav\text{-}las} = 4L_{cav}$ in the current setup to $d_{cav\text{-}las} = L_{cav}$. Further, to reduce turbulences inside the cavity that effectively change the refractive index of the gas and hence effective cavity length, the flow rate should generally be minimized and a buffer volume could be inserted between the vacuum pump and the cavity to minimize noise from the vacuum pump.

7.2. Further Improvements and Future Developments

As was discussed in section 5.3.1, a drastic increase of finesse and intracavity power can be achieved for the Brewster window cavity by using a wedged Brewster window (BW). Since the optimum angle of the BW depends on the mirror losses (compare equations (2.18) and (2.20)), the mirrors must be well characterized to determine the angle β and

corresponding wedge $\varepsilon = \beta_B - \beta$ of the BW that puts the second surface exactly to Brewster's angle β_B. Further, the angular displacement $\Delta\beta$ experienced by the cavity mode upon transmission through the wedged window, given by

$$\Delta\beta = \arcsin\left(n \sin\left(\epsilon + \operatorname{arccsc}\left(\frac{n}{\sin(\beta)}\right)\right)\right) - \epsilon - \beta \tag{7.1}$$

must be taken into account. Herein, n is the refractive index of the window and arccsc denotes the arcus cosecant.

The large sample volume of the currently used gas cell of ~ 1.7 L somewhat conflicts with one of the main selling points of indirect spectroscopy, *i.e.* the possibility of miniaturizing the sample volume. As outlined in section 5.3.1, the volume of the gas cell can be drastically reduced by using the Brewster window as a window of the gas cell. Although the Brewster window - confined gas cell can, in principle, be designed to allow small adjustments of the angle β, *e.g.* based on corrugated bellows, it is much easier and more robust to have β fixed by the design of the gas cell, in particular since the gas volume should be kept small. To this end, the cavity losses must be known beforehand to assess the optimum angle β. Figure 7.2 shows a rendered image of the cross-section through a Brewster window cavity, for which the Brewster window encloses a small gas volume of ~7 cm^3. The mirror mount (designed for one inch mirror mounts from *CRD-optics*) as well as the second mirror are not shown. For a reference scale, the distance between the two flanges in Figure 7.2 is 145 mm. The cavity was designed for interferometric photothermal spectroscopy. The transmission of the green laser through the Fabry-Pérot etalon is manipulated by absorption and associated heating of the sample by the infrared laser and the transmission signal is detected to measure the photothermal absorption spectra [105].

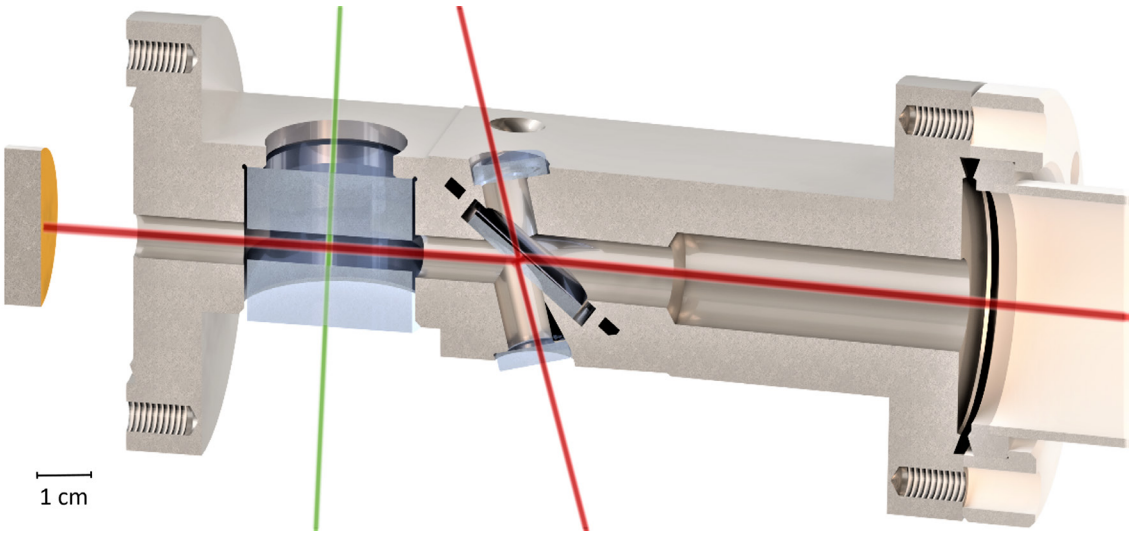

Figure 7.2. Rendered image of a cross-section view through a Brewster window cavity designed for intracavity photothermal spectroscopy in a small gas volume. The Brewster window encloses the gas volume. The second mirror as well as mirror mounts are not shown.

The design can be readily adapted for incorporating a quartz tuning fork and resonator tubes to perform I-QEPAS. A possible disadvantage of the proposed design is that the point of measurement is shifted from the center of the cavity close to one cavity mirror, away from the beam waist. However, when using a flat mirror on the left side in Figure 7.2 and only one curved mirror, the beam waist is at the surface of the flat mirror, close to the point of measurement.

Besides instrumental improvements, changing the operation of I-QEPAS from amplitude modulation to wavelength modulation is worth being investigated (compare calibration in Figure 5.21). Due to the high sensitivity of intracavity measurements, small background absorption from nearby absorption lines contributes significantly to the recorded signals. Using $2f$-wavelength modulation, the selectivity for the targeted absorption line can be drastically increased.

Appendix

A) Matlab Script "Photoacoustic Signals from CO in N_2 and H_2O"

Initialization

```
clear;
```

```
% Pressure and partial pressures in Pa
pall=0.5e5; %overall pressure
%partial pressure
pco=20e-6*pall;
ph2oar=[[0:0.2e-3:1e-2] [1.1e-2:1e-3:2.5e-2]]*pall;
pn2=pall-pco-pco;

T=298; %K

i0=0.0025/0.000234^2/pi; %Laser intensity

% constants
k=1.381e-23; %Boltzmann
R=8.314; %gas constant
c=299792458; %speed of light
h=6.63e-34; %Planck

% Parameters of involved molecules
% Molecular Masses / kg mol^-1
mn2=0.028;
mco=0.028;
mh2o=0.018;
%kinetic radii, m
rco=188e-12;
rn2=182e-12;
rh2o=132.5e-12;

%Parameters of R9 transition of CO
Aco=17.91; %Einstein A coefficient, s^-1
nueco=217977; %resonance wavenumbers, m^-1
g2=21; %degeneracy
g1=19;
FWHM=3.48e9*pall/101325; %FWHM of homogeneously broadened line
partiti=19/107*exp(-h*c*190*9^2/k/T); %fraction of CO molecules in J=9 state, from which
they can be excited
V0=2/pi/FWHM; %Value of area normalized line-shape function at resonance, s
fwhm=11.72*pall/1e5; %full width at half maximum of absorption line, m^-1

% collision numbers
zvvn2co=16100; %collision number for v-v transfer between n2 and co, exothermic
direction
zvvcon2=zvvn2co*exp(18800*299792458*6.63e-34/k/T); %endothermic direction
zvvcoh2o=1400;
zvvn2h2o=26000;
zvtn2=5e7; %Intentionally set lower than 4e9. This is to decrease the equilibration time
in the code. In practice, diffusion will lead to faster equilibration than V-T transfer
```

```
from N2

%collision cross sections
sigcon2=pi*(rco+rn2)^2;
sigcoh2o=pi*(rco+rh2o)^2;
sign2n2=pi*4*rn2^2;
sign2h2o=pi*(rn2+rh2o)^2;
sigh2oh2o=pi*4*rh2o^2;

%Energies associated with V-V and V-T transfers
deltaEvvcon2=18800*c*h; %energy gap between CO and N2 vibration (N2 has higher energy)
deltaEvtn2=233100*c*h; %energy of N2 vibration
deltaEco=214300*c*h; %energy of CO vibration

% Parameters of wavelength modulation
modamp=1.1*fwhm; %Amplitude of wavelength modulation
taumod=1/15820; %Set detection frequency here, modulation frequency is divided by 2 in
code
nper=ceil(0.05/taumod); %Number of periods for which temporal evolution is calculated
```

Calculations

```
%excitation rate constant
gammaexc0=partiti*1/8/pi/h/nueco^3*g2/g1*Aco*V0*i0/c;

% loop for every h2o concentration
for kk=1:numel(ph2oar)

    ph2o=ph2oar(kk);
    pn2=pall-ph2o-pco;

    % Collision frequencies
zcon2=2*pn2/k/T*sigcon2*sqrt(2*R*T/(pi*mn2*mco/(mn2+mn2)));
zcoh2o=2*ph2o/k/T*sigcoh2o*sqrt(2*R*T/(pi*mh2o*mco/(mh2o+mn2)));
zh2on2=2*pn2/k/T*sign2h2o*sqrt(2*R*T/(pi*mn2*mh2o/(mn2+mh2o)));
zn2co=2*pco/k/T*sigcon2*sqrt(2*R*T/(pi*mn2*mco/(mn2+mn2)));
zn2n2=2*pn2/k/T*sign2n2*sqrt(2*R*T/(pi*mn2*mn2/(mn2+mn2)));
zn2h2o=2*ph2o/k/T*sign2h2o*sqrt(2*R*T/(pi*mn2*mh2o/(mn2+mh2o)));
zh2oh2o=2*ph2o/k/T*sigh2oh2o*sqrt(2*R*T/(pi*mh2o*mh2o/(mh2o+mh2o)));

% Rate constants for transfers
gammavvcon2=zcon2/zvvcon2;
gammavvn2co=zn2co/zvvn2co;
gammavvcoh2o=zcoh2o/zvvcoh2o;
gammavvn2h2o=zn2h2o/zvvn2h2o;
gammavtn2=zn2n2/zvtn2;

% Molecular number densities
Nco0=pco/k/T;
Nn20=pn2/k/T;
Nh2o0=ph2o/k/T;

% Definition of time axis
% stepwidth chosen much smaller than fastest process involved
dt=0.001/max([gammaexc0 gammavvcon2 gammavvn2co gammavtn2 gammavvn2h2o gammavvcoh2o
1/taumod]);
tmax=nper*taumod;
```

```
t=[0:dt:tmax];

% modulated wavelength
nuelas=c*(nueco+modamp*cos(pi/taumod*t));
% Area normalized line-shape function corresponding to wavelength axis
vfun=c/pi*0.5*fwhm./((nuelas-c*nueco).^2+0.25*c^2*fwhm^2);
% Excitation rate corresponding to line-shape function
gammaexc=partiti*1/8/pi/h/nueco^3*g2/g1*Aco*vfun*i0/c;

% Initiation of Populations
%excited state populations, assumed zero for t=0
ncoex=zeros(1,numel(t));
nn2ex=ncoex;
nh2oex=ncoex;
ncog=ncoex;
% ground state populations
ncog(1)=Nco0;
nn2g=ncoex;
nn2g(1)=Nn20;
nh2og=ncoex;
nh2og(1)=Nh2o0;
% dissipated kinetic energy, dekin/dt = H
ekin=ncoex;

% Stepwise calculation of differential changes in populations and
% dissipated kinetic energy
for uu=1:numel(t)-1
    dncoexcoh=(ncog(uu)-ncoex(uu))*gammaexc(uu)*dt;
    dncovvn2=dt*(-ncoex(uu)*gammavvcon2+nn2ex(uu)*gammavvn2co);
    dncovvh2o=dt*(-ncoex(uu)*gammavvcoh2o);
    dnn2vvh2o=dt*(-nn2ex(uu)*gammavvn2h2o);
    dnn2vt=-nn2ex(uu)*gammavtn2*dt;
    dekin=dncoexcoh*(nueco*c*h-deltaEco)+deltaEvvcon2*dncovvn2-deltaEco*dncovvh2o-
deltaEvtn2*dnn2vvh2o-deltaEvtn2*dnn2vt;

    ncoex(uu+1)=ncoex(uu)+dncoexcoh+dncovvn2+dncovvh2o;
    ncog(uu+1)=ncog(uu)-(dncoexcoh+dncovvn2+dncovvh2o);
    nn2ex(uu+1)=nn2ex(uu)-dncovvn2+dnn2vvh2o+dnn2vt;
    ekin(uu+1)=ekin(uu)+dekin;
end

% Fourier Transform of last calculated modulation period (when equilibrium
% is reached)
tempind=[numel(t)-floor(taumod/dt)+1:numel(t)];
tper=linspace(dt,taumod-dt,numel(tempind)-1); %timescale of one period
% Complex amplitude of dissipated heat power H = diff(ekin)/dt
compsig(kk)=taumod^-
1*trapz(tper,diff(ekin(tempind))./dt.*(sin(2*pi*tper/taumod)+1i*cos(2*pi*tper/taumod)));
%Complex Fourier amplitude of Power dissipated as kinetic energy at modulation frequency

end

phisig=angle(compsig)*360/2/pi; %Phase of H(2*fmod)
rsig=abs(compsig); %Amplitude of H(2*fmod)
```

Plot results

```
figure(1)
% clf
subplot(2,1,1)
hold on
plot(ph2oar./pall*100,rsig)
% xlim([0 2.2])
xlabel('Water concentration / %_V')
ylabel('Amplitude of heat modulation / W m^-^3')
subplot(2,1,2)
hold on
plot(ph2oar./pall*100,phisig)
% xlim([0 2.2])
xlabel('Water concentration / %_V')
ylabel('Phase of heat modulation / °')

% figure(2)
% clf
% subplot(3,1,1)
% plot(t,ncoex./Nco0)
% title('evolution after switching on the laser')
% xlabel('time / s')
% ylabel('fraction of CO in excited state')
% subplot(3,1,2)
% plot(t,nn2ex./Nn20)
% xlabel('time / s')
% ylabel('fraction of N2 in excited state')
% subplot(3,1,3)
% plot(t,ekin)
% xlabel('time / s')
% ylabel('kinetic energy dissipated in the sample / J m^-^3')

figure(3)
clf
hold on
subplot(2,1,1)
plot(t,ncoex./Nco0)
xlim([max(t)-2*taumod max(t)])
title('evolution after switching on the laser')
xlabel('time / s')
ylabel('fraction of CO in excited state')
subplot(2,1,2)
plot(t(2:end),diff(ekin)/dt)
xlim([max(t)-2*taumod max(t)])
xlabel('time / s')
ylabel('dE_k_i_n/dt = H / W m^-^3')
```

Published with MATLAB® R2017b

B) Abstracts of Works Published in the Course of This Thesis

1) Frequency-Locked Cavity Ring-Down Faraday Rotation Spectroscopy

Citation:

Hayden, J., Westberg, J., Patrick, C. L., Lendl, B., Wysocki, G., *Opt. Lett.* **43** (2018), 20, 5046, DOI: 10.1364/OL.43.005046

Abstract:

Cavity ring-down Faraday rotation spectroscopy (CRD-FRS) is a technique for trace gas measurements of paramagnetic species that retrieves the molecular concentration from the polarization rotation measured as the difference between simultaneously recorded ring-down times of two orthogonal polarization states. The differential measurement is inherently insensitive to non-absorber related losses, which makes off-resonance measurements redundant. We exploit this unique property by actively line-locking to a molecular transition for calibration-free trace gas concentration retrieval. In addition, we enhance the effective duty-cycle of the system by implementing a Pound-Drever-Hall laser lock to the cavity resonance, which allows for ring-down rates of up to 9 kHz. The system performance is demonstrated by measurements of trace oxygen with a minimum detection limit at the ppmv/√Hz-level.

2) Mid-Infrared Sensing of CO at Saturated Absorption Conditions Using Intracavity Quartz-Enhanced Photoacoustic Spectroscopy

Citation:

Hayden, J., Baumgartner, B., Waclawek, J. P., Lendl, B., *Appl. Phys. B* **125**, (2019), 9, 159, DOI: 10.1007/s00340-019-7260-6

Abstract:

The sensitivity of quartz-enhanced photoacoustic spectroscopy (QEPAS) can be drastically increased using the power enhancement in high-finesse cavities. Here, low noise resonant power enhancement to 6.3 W was achieved in a linear Brewster window cavity by exploiting optical feedback locking of a quantum cascade laser. The high intracavity intensity of up to 73 W mm^{-2} in between the prongs of a custom tuning fork resulted in strong optical saturation of CO at 4.59 µm. Saturated absorption is discussed theoretically and experimentally for photoacoustic measurements in general and intracavity QEPAS (I-QEPAS) in particular. The saturation intensity of the R9 transition of CO was retrieved from power dependent I-QEPAS signals. This allowed for sensing CO independently from varying degrees of saturation caused by absorption induced changes of intracavity power. Figures of merit of the I-QEPAS setup for sensing of CO and H_2O are compared to standard wavelength modulation QEPAS without cavity enhancement. For H_2O, the sensitivity was increased by a factor of 230, practically identical to the power enhancement, while the sensitivity gain for CO detection was limited to 57 by optical saturation.

3) **Indirect Mid-Infrared Optical Feedback Cavity-Enhanced Spectroscopy in a Brewster Window Cavity**

Reference:

Hayden, J., Waclawek, J. P., Lendl, B., *Proc. SPIE* **10926** (2019), 96, DOI: 10.1117/12.2509588

Abstract:

An optical setup for cavity enhanced mid-infrared photoacoustic spectroscopy is introduced. Optical feedback from a Brewster window cavity was utilized for efficient coupling of optical power from a distributed feedback quantum cascade laser into an optical cavity with a finesse of 1900, which led to intracavity optical power enhancement by a factor of 300. A custom quartz tuning fork was placed into the center of the cavity for intracavity quartz enhanced photoacoustic spectroscopy of CO at a wavelength of 4.59 µm. As compared to neighboring absorption lines of water, photoacoustic signals of CO were very weak due to slow vibrational to translational energy transfer. Signals increased sharply with increasing humidity. For humidified CO in N_2 at near ambient pressure, a limit of detection (3 σ) of 8.4 ppbHz$^{-1/2}$ was estimated.

4) **A Quantum Cascade Laser-Based Mach–Zehnder Interferometer for Chemical Sensing Employing Molecular Absorption and Dispersion**

Reference:

Hayden, J., Hugger, S., Fuchs, F., Lendl, B., *Appl. Phys. B* **124** (2018), 2, 29, DOI: 10.1007/s00340-018-6899-8

Abstract:

We employ a novel spectroscopic setup based on an external cavity quantum cascade laser and a Mach-Zehnder interferometer to simultaneously record spectra of absorption and dispersion of liquid samples in the mid-infrared. We describe the theory underlying the interferometric measurement and discuss its implications for the experiment. The capability of simultaneously recording a refractive index and absorption spectrum is demonstrated for a sample of acetone in cyclohexane. The recording of absorption spectra is experimentally investigated in more detail to illustrate the method's capabilities as compared to direct absorption spectroscopy. We find that absorption signals are recorded with strongly suppressed background, but with smaller absolute sensitivity. A possibility of optimizing the setup's performance by unbalancing the interferometer is presented.

5) **A Quantitative Comparison of Dispersion- and Absorption-Spectroscopic Gas Sensing**

Citation:

Hayden, J., Martín-Mateos, P., Acedo, P., Lendl, B., *Proc. SPIE* **10110** (2017), 101100Z, DOI: 10.1117/12.2252624

Abstract:

Dispersion spectroscopic sensing of trace gases, measuring the anomalous dispersion at a molecular resonance rather than absorption, has experienced increased attention in the past few years. Their advantages over absorption based spectroscopic sensing are the independence of signals from laser power and their linearity with concentration, even for optically thick samples. In this contribution, we give a comparative discussion of performance, noise and limitations of dispersion and absorption spectroscopy. We relate dispersion spectroscopy to phase-shift rangefinding, for which figures of merit are available in literature. Based on our analysis and the current limitations discussed in the manuscript we conclude that, in terms of limits of detection, dispersion spectroscopy compares with absorption spectroscopy in most experimental situations, but is unlikely to outperform it. However, other unique features of dispersion spectroscopy, thereof especially the linearity with concentration and the independence of power reaching the detector, are highly beneficial for many applications.

6) **Heterodyne Phase-Sensitive Dispersion Spectroscopy in the Mid-Infrared with a Quantum Cascade Laser**

Citation:

Martín-Mateos, P., Hayden, J., Acedo, P., Lendl, B., *Anal. Chem.* **89** (2017), 11, 5916–5922, DOI: 10.1021/acs.analchem.7b00303

Abstract:

Molecular dispersion spectroscopy encompasses a group of spectroscopic techniques for gas analysis that retrieve the characteristics of the sample from the measurement of the profile of its refractive index in the vicinity of molecular resonances. This approach, which is in clear contrast to traditional methods based on the detection of absorption, provides inherent immunity to power fluctuations, calibration-free operation and an output that is linearly dependent on gas concentration. Heterodyne Phase Sensitive Dispersion Spectroscopy (HPSDS) is a very recently proposed technique for molecular dispersion spectroscopy based on tunable lasers that is characterized by a very simple architecture in which data processing and concentration retrieval are straightforward. Different HPSDS implementations have been experimentally validated in the Near-IR. Here, we present the first demonstration of HPSDS in the Mid-IR using a directly modulated Quantum Cascade Laser for the measurement of CO. The set-up is put under test to characterize its response to changing concentrations, pressures and levels of optical intensity on the detector and the limit of detection is estimated. Besides this, an experimental comparison with Wavelength Modulation Spectroscopy with second-harmonic detection (2f-WMS) is

performed and discussed in detail in order to offer a clear view of the benefits and drawbacks that HPSDS can provide over what we could consider the reference method for gas analysis based on tunable laser spectroscopy

7) **Surface Emitting Ring Quantum Cascade Lasers for Chemical Sensing**

Citation:

Szedlak, R., Hayden, J., Martín-Mateos, P., Holzbauer, M., Harrer, A., Schwarz, B., Hinkov, B., MacFarland, D., Zederbauer, T., *et al.*, *Opt. Eng.* **57** (2017), 1, 1–5, DOI: 10.1117/1.OE.57.1.011005

Abstract:

In this paper we review the recent advances in monolithically integrated surface emitting and detecting quantum cascade devices for gas sensing applications. These sensors utilize ring quantum cascade lasers (QCLs) as light sources and are based on conventional laser absorption spectroscopy using the Beer-Lambert law. Furthermore, we demonstrate heterodyne phase-sensitive detection spectroscopy based on such ring QCLs, which provides detailed insights into the tuning behavior of the laser and is capable of significantly enhancing the performance of surface emitting and detecting on-chip gas sensor systems.

8) **In Situ IR Spectroscopy of Mesoporous Silica Films for Monitoring Adsorption Processes and Trace Analysis**

Citation:

Baumgartner, B., Hayden, J., Schwaighofer, A., Lendl, B., *ACS Appl. Nano Mater.* **1** (2018), 12, 7083-7091, DOI: 10.1021/ACSANM.8B01876

Abstract:

Adsorption of molecules at high-surface area materials is a fundamental process involved in many fields of basic and applied chemical research and amongst the simplest and most efficient principles for separating and remediating polluted water. However, established experimental approaches for investigating this fundamental process preclude *in situ* monitoring and thus obtaining real-time information on the ongoing processes. In this work, mid-infrared attenuated total reflection (ATR) spectroscopy is introduced as a powerful technique for quantitative *in situ* monitoring of adsorption processes and thus enrichment of traces of organic pollutants from aqueous solution in ordered mesoporous silica films. The synthesis, functionalization and characterization of two silica films with 3D hexagonal and cubic pore structure on silicon ATR crystals are presented. Benzonitrile and valeronitrile as model compounds for aromatic and aliphatic water pollutants are enriched in hydrophobic films, while the matrix water is excluded from the volume probed by the evanescent field. Enrichment times of < 5 s are observed during *in situ* measurements of

benzonitrile adsorbing onto the film from aqueous solution. The sensing system is calibrated using the Freundlich adsorption equation as calibration function. Enrichment factors of benzonitrile and valeronitrile within the film were determined to be > 200 and > 100, respectively, yielding detection limits in the low ppm range. Furthermore, fast and complete desorption of the analyte was verified and assures reliable regeneration of the sensor. Lastly, we derive and experimentally validate equations for ATR spectroscopy with thin film adsorption layers to quantify the absolute mass of adsorbed pollutant in the film. An excellent agreement between recorded absorptions at target wavenumbers of the target analytes and corresponding simulations corroborates the validity of the chosen approach.

9) **High Frequency Modulation and (Quasi) Single-Sideband Emission of Mid-Infrared Ring and Ridge Quantum Cascade Lasers**

Citation:

Hinkov, B., Hayden, J., Szedlak, R., Martin-Mateos, P., Jerez, B., Acedo, P., Strasser, G., Lendl, B., *Opt. Express* **27** (2019), 10, 14716, DOI: 10.1364/OE.27.014716

Abstract:

We investigate the high frequency modulation characteristics of mid-infrared surface-emitting ring and edge-emitting ridge quantum cascade lasers (QCLs). In particular, a detailed comparison between circular ring devices and ridge-QCLs from the same laser material, which have a linear waveguide in a “Fabry-Pérot (FP) type” cavity, reveals distinct similarities and differences. Both device types are single-mode emitting, based on either 2nd- (ring-QCL) or 1st -order (ridge-QCL) distributed feedback (DFB) gratings with an emission wavelength around 7.56 µm. Their modulation characteristics are investigated in the frequency-domain using an optical frequency-to-amplitude conversion technique based on the ro-vibrational absorptions of CH_4. We observe that the amplitude of frequency tuning Δf over intensity modulation index m as function of the modulation frequency behaves similarly for both types of devices, while the ring-QCLs typically show higher values. The frequency-to-intensity modulation (FM-IM) phase shift shows a decrease starting from $\sim 72\circ$ at a modulation frequency of 800 kHz to about $0\circ$ at 160 MHz. In addition, we also observe a quasi single-sideband (qSSB) regime for modulation frequencies above 100 MHz, which is identified by a vanishing -1st -order sideband for both devices. This special FM-state can be observed in DFB QCLs and is in strong contrast to the behavior of regular DFB diode lasers, which do not achieve any significant sideband suppression. By analyzing these important high frequency characteristics of ring-QCLs and comparing them to ridge DFB-QCLs, it shows the potential of intersubband devices for applications in *e.g.* novel spectroscopic techniques and highly-integrated and high-bitrate free-space data communication. In addition, the obtained results close an existing gap in literature for high frequency modulation characteristics of QCLs.

10) **Pore Size-Dependent Structure of Confined Water in Mesoporous Silica Films from Water Adsorption-Desorption using ATR-FTIR Spectroscopy**

Citation:

Baumgartner, B., Hayden, J., Loizillon, J., Steinbacher, S., Grosso, D., Lendl, B.,

Accepted for publication in *Langmuir* (2019), DOI: 10.1021/acs.langmuir.9b01435

Abstract:

The local structure of water on chemically and structurally different surfaces is subject of ongoing research. In particular, confined spaces as found in mesoporous silica have a pronounced effect on the interplay between adsorbate-adsorbate and adsorbate-surface interactions. Mid-infrared spectroscopy is ideally suited to quantitatively and qualitatively study such systems as the probed molecular vibrations are highly sensitive to intermolecular interactions. Here, the quantity and structure of water adsorbed from the gas phase into silica mesopores at different water vapor pressures was monitored using mid-infrared attenuated total reflection (ATR) spectroscopy. Germanium ATR crystals were coated with different mesoporous silica films prepared by evaporation induced self-assembly. Quantitative analysis of the water bending vibration at 1640 cm^{-1} at varying vapor pressure allowed for retrieving porosity and pore size distribution of the mesoporous films. The results were in excellent agreement with those obtained from ellipsometric porosimetry. In addition, different degrees of hydrogen bonding of water as reflected in the band position and shape of the stretching vibrations (3000 – 3750 cm^{-1}) were analyzed and attributed to high-density, unordered bulk and low-density, surface-induced ordered water. Thereby, the progression of surface-induced ordered water and bulk water as a function of water vapor pressure was studied for different pore sizes. Small pores with 5 nm diameter showed a number of two ordered monolayers, while for pores > 12 nm the number of ordered monolayers is significantly larger and agrees with the number observed on planar SiO_2 surfaces.

11) **External Cavity Quantum Cascade Laser Based Mid-Infrared Dispersion Spectroscopy for Qualitative and Quantitative Analysis of Liquid-Phase Samples**

Citation:

Lindner, S., Hayden, J., Schwaighofer, A., Wolflehner, T., Kristament, C., González-Cabrera, M., Zlabinger, S., and Lendl, B.

Submitted for publication in *Appl. Spectrosc.* (2019)

Abstract:

Acquisition of classical absorption spectra of liquids in the mid-IR range with quantum cascade lasers (QCLs) is often limited in sensitivity by noise from the laser source. Alternatively, measurement of molecular dispersion (*i.e.* refractive index) spectra poses an

experimental approach that is immune to intensity fluctuations and further offers a direct relationship between the recorded signal and the sample concentration. In this work, we present an EC-QCL based Mach-Zehnder interferometer setup to determine dispersion spectra of liquid samples. We present two approaches for acquisition of refractive index spectra and compare the qualitative experimental results. Furthermore, the performance for quantitative analysis is evaluated. Finally, multivariate analysis of a spectrally complex mixture comprising three different sugars is performed. The obtained figures of merit by partial least squares (PLS) regression modelling compare well with standard absorption spectroscopy, demonstrating the potential of the introduced dispersion spectroscopic method for quantitative chemical analysis.

12) **Mesoporous Silica Films for Sensing Volatile Organic Compounds using Attenuated Total Reflection Spectroscopy**

Citation:
Baumgartner, B., Hayden, J. and Lendl, B.; Accepted for publication in *Sens Actuator B Chem* (2019), DOI: 10.1016/j.snb.2019.127194

Abstract:
The sensitivity of evanescent wave sensing of gaseous species can be vastly increased by enrichment materials that locally concentrate the analyte on the sensor. Here, we investigate functionalized mesoporous silica films as versatile enrichment layer for sensing volatile organic compounds (VOCs) from gas-phase. Attenuated total reflection (ATR) crystals were coated with silica films of different pore sizes and their capability to enrich three different aromatic hydrocarbons from a vapor stream was studied by means of FTIR spectroscopy. Thereby, single-digit ppmv limits of detection were achieved with an effective pathlength of only 6.3 µm. The selectivity introduced by the functionalization of the silica films effectively minimized interferences of water vapor, which gave access to the spectral fingerprint region between 1550 and 1450 cm^{-1}. This allowed to discriminate and quantify toluene, *p*-xylene and 1,2,4-trimethylbenzene in multicomponent mixtures at high humidity. Fast response and regeneration times and enrichment factors up to 32000 showcase the high potential of this material for evanescent wave sensing.

References

1. L. J. Carpenter, S. Reimann, J. B. Burkholder, C. Clerbaux, B. D. Hall, R. Hossaini, J. C. Laube, and S. A. Yvon-Lewis, *Ozone-Depleting Substances (ODSs) and Other Gases of Interest to the Montreal Protocol, Chapter 1 to Scientific Assessment of Ozone Depletion* (2014).

2. C. Di Natale, R. Paolesse, E. Martinelli, and R. Capuano, Anal. Chim. Acta **824**, 1 (2014), DOI: 10.1016/J.ACA.2014.03.014.

3. A. S. Modak, J. Breath Res. **1**, 014003 (2007), DOI: 10.1088/1752-7155/1/1/014003.

4. J. Zádor, C. A. Taatjes, and R. X. Fernandes, Prog. Energy Combust. Sci. **37**, 371 (2011), DOI: 10.1016/J.PECS.2010.06.006.

5. B. Brumfield, W. Sun, Y. Ju, and G. Wysocki, J. Phys. Chem. Lett. **4**, 872 (2013), DOI: 10.1021/jz400143c.

6. J. Hodgkinson and R. P. Tatam, Meas. Sci. Technol. **24**, 012004 (2013), DOI: 10.1088/0957-0233/24/1/012004.

7. www.tigeroptics.com; accessed: 2019; https://www.tigeroptics.com/technology.html#cavity-ring-down-spectroscopy.

8. www.lgrinc.com; accessed: 2019; http://www.lgrinc.com/advantages/.

9. J. Hayden, J. Westberg, C. L. Patrick, B. Lendl, and G. Wysocki, Opt. Lett. **43**, 5046 (2018), DOI: 10.1364/OL.43.005046.

10. J. Hayden, J. P. Waclawek, and B. Lendl, in *Quantum Sens. Nano Electron. Photonics XVI*, edited by M. Razeghi and E. Tournié (SPIE, 2019), p. 96.

11. J. Hayden, B. Baumgartner, J. P. Waclawek, and B. Lendl, Appl. Phys. B **125**, 159 (2019), DOI: 10.1007/s00340-019-7260-6.

12. G. A. Reider, in *Photonik - Eine Einführung Indie Grundlagen* (Springer Vienna, Vienna, 2012), pp. 35–92.

13. G. Herzberg, in *Mol. Spectra Mol. Struct. - II.* (Van Nostrand, 1945), pp. 370–500.

14. H. Moser, Development and Implementation of an Industrial Process Gas Monitoring System for H2S Based on Mid-Infrared Quantum Cascade Laser Spectroscopy, Technische Univerisät Wien, 2016.

15. I. E. Gordon, L. S. Rothman, C. Hill, R. V. Kochanov, Y. Tan, P. F. Bernath, M. Birk, V. Boudon, A. Campargue, K. V. Chance, B. J. Drouin, J.-M. Flaud, R. R. Gamache, J. T. Hodges, D. Jacquemart, V. I. Perevalov, A. Perrin, K. P. Shine, M.-A. H. Smith, J.

Tennyson, G. C. Toon, H. Tran, V. G. Tyuterev, A. Barbe, A. G. Császár, V. M. Devi, T. Furtenbacher, J. J. Harrison, J.-M. Hartmann, A. Jolly, T. J. Johnson, T. Karman, I. Kleiner, A. A. Kyuberis, J. Loos, O. M. Lyulin, S. T. Massie, S. N. Mikhailenko, N. Moazzen-Ahmadi, H. S. P. Müller, O. V. Naumenko, A. V. Nikitin, O. L. Polyansky, M. Rey, M. Rotger, S. W. Sharpe, K. Sung, E. Starikova, S. A. Tashkun, J. Vander Auwera, G. Wagner, J. Wilzewski, P. Wcisło, S. Yu, and E. J. Zak, J. Quant. Spectrosc. Radiat. Transf. **203**, 3 (2017), DOI: 10.1016/J.JQSRT.2017.06.038.

16. HITRANonline - Documentation: Units and definitions; accessed: 2019; https://hitran.org/docs/definitions-and-units/.

17. J. Tennyson, P. F. Bernath, A. Campargue, A. G. Császár, L. Daumont, R. R. Gamache, J. T. Hodges, D. Lisak, O. V. Naumenko, L. S. Rothman, H. Tran, J. M. Hartmann, N. F. Zobov, J. Buldyreva, C. D. Boone, M. D. De Vizia, L. Gianfrani, R. McPheat, D. Weidmann, J. Murray, N. H. Ngo, and O. L. Polyansky, Pure Appl. Chem. **86**, 1931 (2014), DOI: 10.1515/pac-2014-0208.

18. C. S. Goldenstein, V. A. Miller, R. Mitchell Spearrin, and C. L. Strand, J. Quant. Spectrosc. Radiat. Transf. **200**, 249 (2017), DOI: 10.1016/J.JQSRT.2017.06.007.

19. R. V. Kochanov, I. E. Gordon, L. S. Rothman, P. Wcisło, C. Hill, and J. S. Wilzewski, J. Quant. Spectrosc. Radiat. Transf. **177**, 15 (2016), DOI: 10.1016/J.JQSRT.2016.03.005.

20. J. B. McManus, M. S. Zahniser, D. D. Nelson, J. H. Shorter, S. C. Herndon, D. Jervis, M. Agnese, R. McGovern, T. I. Yacovitch, and J. R. Roscioli, Appl. Phys. B **119**, 203 (2015), DOI: 10.1007/s00340-015-6033-0.

21. J. B. McManus, P. L. Kebabian, and M. S. Zahniser, Appl. Opt. **34**, 3336 (1995), DOI: 10.1364/AO.34.003336.

22. D. D. Nelson, J. H. Shorter, J. B. McManus, and M. S. Zahniser, Appl. Phys. B Lasers Opt. **75**, 343 (2002), DOI: 10.1007/s00340-002-0979-4.

23. H. Moser, W. Pölz, J. P. Waclawek, J. Ofner, and B. Lendl, Anal. Bioanal. Chem. 1 (2016), DOI: 10.1007/s00216-016-9923-z.

24. J. Hayden, S. Hugger, F. Fuchs, and B. Lendl, Appl. Phys. B **124**, 29 (2018), DOI: 10.1007/s00340-018-6899-8.

25. G. Ramer and B. Lendl, in *Encycl. Anal. Chem.*, edited by R. A. Meyers (John Wiley & Sons, Ltd, Chichester, UK, 2006).

26. A. Hangauer, G. Spinner, M. Nikodem, and G. Wysocki, Opt. Express **22**, 23439 (2014), DOI: 10.1364/OE.22.023439.

27. M. Shurgalin, W. H. Parkinson, K. Yoshino, C. Schoene, and W. P. Lapatovich, Meas. Sci. Technol. **11**, 730 (2000), DOI: 10.1088/0957-0233/11/6/316.

28. G. Wysocki and D. Weidmann, Opt. Express **18**, 26123 (2010), DOI: 10.1364/OE.18.026123.

29. P. Martín-Mateos, J. Hayden, P. Acedo, and B. Lendl, Anal. Chem. **89**, 5916 (2017), DOI: 10.1021/acs.analchem.7b00303.

30. P. Martín-Mateos and P. Acedo, Opt. Express **22**, 15143 (2014), DOI: 10.1364/OE.22.015143.

31. J. Hayden, P. Martín-Mateos, P. Acedo, and B. Lendl, Proc. SPIE **10110**, 101100Z (2017), DOI: 10.1117/12.2252624.

32. A. Hangauer, G. Spinner, M. Nikodem, and G. Wysocki, Appl. Phys. Lett. **103**, (2013), DOI: 10.1063/1.4829036.

33. B. Hinkov, J. Hayden, R. Szedlak, P. Martin-Mateos, B. Jerez, P. Acedo, G. Strasser, and B. Lendl, Opt. Express **27**, 14716 (2019), DOI: 10.1364/OE.27.014716.
34. G. Plant, A. Hangauer, and G. Wysocki, IEEE J. Sel. Top. Quantum Electron. **23**, (2017), DOI: 10.1109/JSTQE.2016.2614496.
35. M. Nikodem, G. Plant, D. Sonnenfroh, and G. Wysocki, Appl. Phys. B Lasers Opt. **119**, 3 (2015), DOI: 10.1007/s00340-014-5938-3.
36. G. Plant, Y. Chen, and G. Wysocki, Opt. Lett. **42**, 2770 (2017), DOI: 10.1364/OL.42.002770.
37. W. Ding, L. Sun, L. Yi, and X. Ming, Appl. Opt. **55**, 8698 (2016).
38. MIRICO - Advanced Laser Gas Sensing Solutions Instruments; accessed: 2019; http://mirico.co.uk/.
39. *DIN 32645, Chemische Analytik – Nachweis-, Erfassungs- Und Bestimmungsgrenze Unter Wiederholbedingungen – Begriffe, Verfahren, Auswertung* (2008).
40. B. Neidhart and W. Wegscheider, editors , *Quality in Chemical Measurements* (Springer Berlin Heidelberg, Berlin, Heidelberg, 2001).
41. P. Werle, R. Mücke, and F. Slemr, Appl. Phys. B **57**, 131 (1993), DOI: 10.1007/BF00425997.
42. A. Genner, P. Martín-Mateos, H. Moser, J. P. Waclawek, and B. Lendl, in *Quantum Sens. Nano Electron. Photonics XVI*, edited by M. Razeghi, J. S. Lewis, G. A. Khodaparast, and E. Tournié (SPIE, 2019), p. 95.
43. G. Gagliardi and H.-P. Loock, editors , *Cavity-Enhanced Spectroscopy and Sensing* (Springer Berlin Heidelberg, 2014).
44. N. Hodgson and H. Weber, *Laser Resonators and Beam Propagation*, 2nd ed. (Springer, 2005).
45. D. Z. Anderson, J. C. Frisch, and C. S. Masser, Appl. Opt. **23**, 1238 (1984), DOI: 10.1364/AO.23.001238.
46. T. M. Crawford, in edited by S. C. Stotlar (International Society for Optics and Photonics, 1985), p. 295.
47. A. O'Keefe and D. A. G. Deacon, Rev. Sci. Instrum. **59**, 2544 (1988), DOI: 10.1063/1.1139895.
48. D. Romanini, I. Ventrillard, G. Méjean, J. Morville, and E. Kerstel, in *Cavity-Enhanced Spectrosc. Sens.*, edited by G. Gagliardi and H.-P. Loock (Springer Berlin Heidelberg, Berlin, Heidelberg, 2014), pp. 1–60.
49. N. Hodgson and H. Weber, *Laser Resonators and Beam Propagation*, Second Edi (Springer, 2005).
50. G. A. Reider, in *Photonik - Eine Einführung Indie Grundlagen*, edited by G. Reider, 3rd ed. (Springer Vienna, Vienna, 2012), pp. 141–178.
51. G. Reider, in *Photonik - Eine Einführung Indie Grundlagen*, edited by G. Reider, 3rd ed. (Springer, 2012), pp. 93–139.
52. D. Z. Anderson, Appl. Opt. **23**, 2944 (1984), DOI: 10.1364/AO.23.002944.
53. G. Gagliardi and H.-P. Loock, *Cavity-Enhanced Spectroscopy and Sensing* (Springer Berlin Heidelberg, 2014).
54. L.-S. Ma, J. Ye, P. Dubé, and J. L. Hall, J. Opt. Soc. Am. B **16**, 2255 (1999), DOI: 10.1364/JOSAB.16.002255.
55. R. Damaschini, Opt. Commun. **20**, 441 (1976), DOI: 10.1016/0030-4018(77)90225-5.

56. K. K. Lehmann, P. S. Johnston, and P. Rabinowitz, Appl. Opt. **48**, 2966 (2009), DOI: 10.1364/AO.48.002966.
57. R. W. Fox, C. W. Oates, and L. W. Hollberg, in *Exp. Methods Phys. Sci.* (2003), pp. 1–46.
58. J. M. Khosrofian and B. A. Garetz, Appl. Opt. **22**, 3406 (1983), DOI: 10.1364/AO.22.003406.
59. J. A. Arnaud, W. M. Hubbard, G. D. Mandeville, B. de la Clavière, E. A. Franke, and J. M. Franke, Appl. Opt. **10**, 2775 (1971), DOI: 10.1364/AO.10.002775.
60. V. Bauer, Injection of a Quantum Cascade Laser into a High-Finesse Optical Resonator, TU Wien, 2015.
61. Q. Photonics, Qioptiq Q-Shop | Winlens 3D; accessed: n.d.; http://www.qioptiq-shop.com/Optik-Software/Winlens-Optical-Design-Software/Winlens-3D/.
62. E. D. Black, Am. J. Phys. **69**, 79 (2001), DOI: 10.1119/1.1286663.
63. R. W. P. Drever, J. L. Hall, F. V. Kowalski, J. Hough, G. M. Ford, A. J. Munley, and H. Ward, Appl. Phys. B **31**, 97 (1983), DOI: 10.1007/BF00702605.
64. A. Abramovici, W. E. Althouse, R. W. Drever, Y. Gürsel, S. Kawamura, F. J. Raab, D. Shoemaker, L. Sievers, R. E. Spero, K. S. Thorne, R. E. Vogt, R. Weiss, S. E. Whitcomb, and M. E. Zucker, Science (80-.). **256**, 325 (1992), DOI: 10.1126/science.256.5055.325.
65. J. L. Hall, M. S. Taubman, and J. Ye, in *Handb. Opt. 2. Des. Fabr. Test. ; Sources Detect. ; Radiom. Photom.*, edited by M. Bass, third (McGraw-Hill Professional, New York, 2010).
66. A. Hangauer, Jia Chen, R. Strzoda, and M. C. Amann, IEEE J. Sel. Top. Quantum Electron. **17**, 1584 (2011), DOI: 10.1109/JSTQE.2011.2110640.
67. L. Tombez, F. Cappelli, S. Schilt, G. Di Domenico, S. Bartalini, and D. Hofstetter, Appl. Phys. Lett. **103**, 1 (2013), DOI: 10.1063/1.4813753.
68. G. Wysocki, R. F. Curl, F. K. Tittel, R. Maulini, J. M. Bulliard, and J. Faist, Appl. Phys. B **81**, 769 (2005), DOI: 10.1007/s00340-005-1965-4.
69. M. S. Taubman, T. L. Myers, B. D. Cannon, and R. M. Williams, Spectrochim. Acta - Part A Mol. Biomol. Spectrosc. **60**, 3457 (2004), DOI: 10.1016/j.saa.2003.12.057.
70. R. T. Ramos, A. J. Seeds, A. Bordonalli, P. Gallion, and D. Erasme, Opt. Lett. **19**, 4 (1994), DOI: 10.1364/OL.19.000004.
71. S. Borri, I. Galli, F. Cappelli, A. Bismuto, S. Bartalini, P. Cancio, G. Giusfredi, D. Mazzotti, J. Faist, and P. De Natale, Opt. Lett. **37**, 1011 (2012), DOI: 10.1364/ol.37.001011.
72. P. Laurent, A. Clairon, and C. Breant, IEEE J. Quantum Electron. **25**, 1131 (1989), DOI: 10.1109/3.29238.
73. J. Morville, D. Romanini, and E. Kerstel, in *Cavity Enhanc. Spectrosc. Sensing*, edited by G. Gagliardi and H.-P. Loock (Springer Berlin Heidelberg, 2014), pp. 163–209.
74. C. H. Henry, IEEE J. Quantum Electron. **18**, 259 (1982), DOI: 10.1109/JQE.1982.1071522.
75. B. Hinkov, A. Hugi, M. Beck, and J. Faist, Opt. Express **24**, 3294 (2016), DOI: 10.1364/OE.24.003294.
76. A. Hangauer and G. Wysocki, IEEE J. Sel. Top. Quantum Electron. **21**, 74 (2015), DOI: 10.1109/JSTQE.2015.2422073.
77. J. Morville, D. Romanini U, A. Kachanov, and M. Chenevier, Appl. Phys. B **78**, 465

(2004), DOI: 10.1007/s00340-003-1363-8.
78. J. Morville, S. Kassi, M. Chenevier, and D. Romanini, Appl. Phys. B **80**, 1027 (2005), DOI: 10.1007/s00340-005-1828-z.
79. B. Dahmani, L. Hollberg, and R. Drullinger, Opt. Lett. **12**, 876 (1987), DOI: 10.1364/OL.12.000876.
80. Jungho Kim, M. Lerttamrab, Shun Lien Chuang, C. Gmachl, D. L. Sivco, F. Capasso, and a. Y. Cho, IEEE J. Quantum Electron. **40**, 1663 (2004), DOI: 10.1109/JQE.2004.837666.
81. J. von Staden, T. Gensty, W. Elsäßer, G. Giuliani, and C. Mann, Opt. Lett. **31**, 2574 (2006), DOI: 10.1364/OL.31.002574.
82. F. P. Mezzapesa, L. L. Columbo, M. Brambilla, M. Dabbicco, S. Borri, M. S. Vitiello, H. E. Beere, D. A. Ritchie, and G. Scamarcio, Opt. Express **21**, 13748 (2013), DOI: 10.1364/OE.21.013748.
83. G. Berden and R. Engeln, *Cavity Ring-Down Spectroscopy: Techniques and Applications* (Wiley, 2010).
84. K. K. Lehmann and H. Huang, in *Front. Mol. Spectrosc.*, edited by J. Laane (Elsevier, 2009), pp. 623–658.
85. D. Romanini, I. Ventrillard, G. Méjean, J. Morville, and E. Kerstel, in *Cavity Enhanc. Spectrosc. Sens.*, edited by G. Gagliardi and H.-P. Loock (Springer, Berlin, Heidelberg, 2014), pp. 1–60.
86. R. C. Hilborn, Am. J. Phys. **50**, 982 (1982), DOI: 10.1119/1.12937.
87. M. Šimečková, D. Jacquemart, L. S. Rothman, R. R. Gamache, and A. Goldman, J. Quant. Spectrosc. Radiat. Transf. **98**, 130 (2006), DOI: 10.1016/J.JQSRT.2005.07.003.
88. W. Demtröder, in *Laserspektroskopie 1 Grundlagen*, 6th ed. (Springer, 2014), pp. 5–41.
89. L. S. Rothman, I. E. Gordon, Y. Babikov, A. Barbe, D. Chris Benner, P. F. Bernath, M. Birk, L. Bizzocchi, V. Boudon, L. R. Brown, A. Campargue, K. Chance, E. A. Cohen, L. H. Coudert, V. M. Devi, B. J. Drouin, A. Fayt, J.-M. Flaud, R. R. Gamache, J. J. Harrison, J.-M. Hartmann, C. Hill, J. T. Hodges, D. Jacquemart, A. Jolly, J. Lamouroux, R. J. Le Roy, G. Li, D. A. Long, O. M. Lyulin, C. J. Mackie, S. T. Massie, S. Mikhailenko, H. S. P. Müller, O. V. Naumenko, A. V. Nikitin, J. Orphal, V. Perevalov, A. Perrin, E. R. Polovtseva, C. Richard, M. A. H. Smith, E. Starikova, K. Sung, S. Tashkun, J. Tennyson, G. C. Toon, V. G. Tyuterev, and G. Wagner, J. Quant. Spectrosc. Radiat. Transf. **130**, 4 (2013), DOI: 10.1016/j.jqsrt.2013.07.002.
90. J. D. Lambert, *Vibrational and Rotational Relaxation in Gases* (Clarendon Pr., Oxford, 1977).
91. G. Wedler, in *Lehrb. Der Phys. Chemie*, edited by G. Wedler, 5th ed. (Wiley-VCH, Weinheim, 2004), pp. 812–813.
92. I. Glassman and B. L. Harris, J. Phys. Chem. **56**, 797 (1952), DOI: 10.1021/j150498a036.
93. L. Régalia-Jarlot, X. Thomas, P. Von der Heyden, and A. Barbe, J. Quant. Spectrosc. Radiat. Transf. **91**, 121 (2005), DOI: 10.1016/j.jqsrt.2004.05.042.
94. W. Demtröder, in *Laser Spectrosc. 1* (Springer Berlin Heidelberg, Berlin, Heidelberg, 2011), pp. 61–98.
95. K. N. Liou, in *An Introd. to Atmos. Radiat.*, edited by K. N. Liou (Academic Press, 2002), pp. 1–36.

96. R. N. Schwartz, Z. I. Slawsky, and K. F. Herzfeld, J. Chem. Phys. **20**, 1591 (1952), DOI: 10.1063/1.1700221.
97. P. Ehrenfest, Phys. Zeitschrift **15**, 633 (1914).
98. P. G. Kistemaker, A. Tom, and A. E. De Vries, Physica **48**, 414 (1970), DOI: 10.1016/0031-8914(70)90247-8.
99. M. G. Ferguson and A. W. Read, Trans. Faraday Soc. **61**, 1559 (1965), DOI: 10.1039/tf9656101559.
100. L. Landau and E. Teller, Phys. Zeitschrifft Der Sowjetunion **10**, 34 (1936).
101. P. F. Zittel and D. E. Masturzo, J. Chem. Phys. **90**, 977 (1989), DOI: 10.1063/1.456122.
102. A. D. Wood, M. Camac, and E. T. Gerry, Appl. Opt. **10**, 1877 (1971), DOI: 10.1364/AO.10.001877.
103. S. Bialkowski, *Photothermal Spectroscopy Methods for Chemical Analysis* (Wiley, 1996).
104. J. P. Waclawek, V. C. Bauer, H. Moser, and B. Lendl, Opt. Express **24**, 28958 (2016), DOI: 10.1364/OE.24.028958.
105. J. P. Waclawek, C. Kristament, H. Moser, and B. Lendl, Opt. Express **27**, 12183 (2019), DOI: 10.1364/OE.27.012183.
106. A. Miklós, S. Schäfer, and P. Hess, in *Encycl. Spectrosc. Spectrom.*, edited by J. C. Lindon, 3rd ed. (Elsevier, 1999), pp. 2151–2158.
107. A. Miklos, S. Schäfer, and P. Hess, in *Encycl. Spectrosc. Spectrom.*, edited by J. Lindon, G. Tranter, and D. Koppenaal, 3rd ed. (2015), pp. 2151–2158.
108. D. Pugh, in (1989), pp. 15–36.
109. A. Miklos, P. Hess, and Z. Bozoki, Rev. Sci. Instrum. **72**, 1937 (2001), DOI: 10.1063/1.1353198.
110. M. D. Wojcik, M. C. Phillips, B. D. Cannon, and M. S. Taubman, Appl. Phys. B **85**, 307 (2006), DOI: 10.1007/s00340-006-2394-8.
111. A. Rosencwaig, *Photoacoustics and Photoacoustic Spectroscopy* (Wiley, 1980).
112. L. Xiong, W. Bai, F. Chen, X. Zhao, F. Yu, and G. J. Diebold, Proc. Natl. Acad. Sci. U. S. A. **114**, 7246 (2017), DOI: 10.1073/pnas.1706040114.
113. L. Dong, A. A. Kosterev, D. Thomazy, and F. K. Tittel, Appl. Phys. B **100**, 627 (2010), DOI: 10.1007/s00340-010-4072-0.
114. H. Yi, W. Chen, S. Sun, K. Liu, T. Tan, and X. Gao, Opt. Express **20**, 9187 (2012), DOI: 10.1364/OE.20.009187.
115. F. G. C. Bijnen, J. Reuss, and F. J. M. Harren, Rev. Sci. Instrum. **67**, 2914 (1996), DOI: 10.1063/1.1147072.
116. F. J. M. Harren and S. M. Cristescu, in *Encycl. Anal. Chem.* (Wiley, 2019), pp. 1–29.
117. A. A. Kosterev, Y. A. Bakhirkin, R. F. Curl, and F. K. Tittel, Opt. Lett. **27**, 1902 (2002), DOI: 10.1364/OL.27.001902.
118. N. Ogawa and F. Kaneko, Eur. J. Phys. **34**, 1159 (2013), DOI: 10.1088/0143-0807/34/5/1159.
119. S. Li, L. Dong, H. Wu, A. Sampaolo, P. Patimisco, V. Spagnolo, and F. K. Tittel, Anal. Chem. **91**, 5834 (2019), DOI: 10.1021/acs.analchem.9b00182.
120. P. Patimisco, G. Scamarcio, F. K. Tittel, and V. Spagnolo, Sensors **14**, 6165 (2014), DOI: 10.3390/s140406165.

121. P. Patimisco, A. Sampaolo, H. Zheng, L. Dong, F. K. Tittel, and V. Spagnolo, Adv. Phys. X **2**, 169 (2017), DOI: 10.1080/23746149.2016.1271285.
122. P. Patimisco, A. Sampaolo, M. Giglio, S. dello Russo, V. Mackowiak, H. Rossmadl, A. Cable, F. K. Tittel, and V. Spagnolo, Opt. Express **27**, 1401 (2019), DOI: 10.1364/oe.27.001401.
123. J. Uotila, Use Of The Optical Cantilever Microphone In Photoacoustic Spectroscopy, 2009.
124. S. Li, L. Dong, H. Wu, A. Sampaolo, P. Patimisco, V. Spagnolo, and F. K. Tittel, Anal. Chem. **91**, 5834 (2019), DOI: 10.1021/acs.analchem.9b00182.
125. Y. Ma, R. Lewicki, M. Razeghi, and F. K. Tittel, Opt. Express **21**, 1008 (2013), DOI: 10.1364/OE.21.001008.
126. B. H. Lee, E. C. Wood, M. S. Zahniser, J. B. McManus, D. D. Nelson, S. C. Herndon, G. W. Santoni, S. C. Wofsy, and J. W. Munger, Appl. Phys. B **102**, 417 (2011), DOI: 10.1007/s00340-010-4266-5.
127. P. Malara, M. F. Witinski, F. Capasso, J. G. Anderson, and P. De Natale, Appl. Phys. B **108**, 353 (2012), DOI: 10.1007/s00340-012-4975-z.
128. P. Gorrotxategi-Carbajo, E. Fasci, I. Ventrillard, M. Carras, G. Maisons, and D. Romanini, Appl. Phys. B **110**, 309 (2013), DOI: 10.1007/s00340-013-5340-6.
129. P. Patimisco, A. Sampaolo, L. Dong, F. K. Tittel, and V. Spagnolo, Appl. Phys. Rev. **5**, 011106 (2018), DOI: 10.1063/1.5013612.
130. F. J. M. Harren, F. G. C. Bijnen, J. Reuss, L. A. C. J. Voesenek, and C. W. P. M. Blom, Appl. Phys. B Photophysics Laser Chem. **50**, 137 (1990), DOI: 10.1007/BF00331909.
131. Z. Bozóki, J. Sneider, G. Szabó, A. Miklós, M. Serényi, G. Nagy, and M. Fehér, Appl. Phys. B Lasers Opt. **63**, 399 (1996), DOI: 10.1007/BF01828745.
132. V. S. Starovoitov, J. F. Kischkat, M. P. Semtsiv, and W. Ted Masselink, Opt. Lett. **41**, 4955 (2016), DOI: 10.1364/OL.41.004955.
133. Z. Wang, Q. Wang, W. Zhang, H. Wei, Y. Li, and W. Ren, Opt. Lett. **44**, 1924 (2019), DOI: 10.1364/OL.44.001924.
134. A. Kachanov, S. Koulikov, and F. K. Tittel, Appl. Phys. B **110**, 47 (2013), DOI: 10.1007/s00340-012-5250-z.
135. P. Patimisco, S. Borri, I. Galli, D. Mazzotti, G. Giusfredi, N. Akikusa, M. Yamanishi, G. Scamarcio, P. De Natale, and V. Spagnolo, Analyst **140**, 736 (2015), DOI: 10.1039/C4AN01158A.
136. J. Westberg, Faraday Modulation Spectroscopy - Theoretical Description and Experimental Realization for Detection of Nitric Oxide, Umea University, 2013.
137. J. Westberg, L. Lathdavong, C. M. Dion, J. Shao, P. Kluczynski, S. Lundqvist, and O. Axner, J. Quant. Spectrosc. Radiat. Transf. **111**, 2415 (2010), DOI: 10.1016/J.JQSRT.2010.06.017.
138. R. J. Brecha, L. M. Pedrotti, and D. Krause, J. Opt. Soc. Am. B **14**, 1921 (1997), DOI: 10.1364/JOSAB.14.001921.
139. M. Gianella, T. H. P. Pinto, X. Wu, and G. A. D. Ritchie, J. Chem. Phys. **147**, 054201 (2017), DOI: 10.1063/1.4985900.
140. W. Herrmann, W. Rohrbeck, and W. Urban, Appl. Phys. **22**, 71 (1980), DOI: 10.1007/BF00897935.
141. E. J. Zhang, B. Brumfield, and G. Wysocki, Opt. Express **22**, 15957 (2014), DOI:

10.1364/OE.22.015957.
142. B. Brumfield, W. Sun, Y. Wang, Y. Ju, and G. Wysocki, Opt. Lett. **39**, 1783 (2014), DOI: 10.1364/OL.39.001783.
143. C. L. Patrick, J. Westberg, and G. Wysocki, Anal. Chem. acs. analchem.8b04359 (2018), DOI: 10.1021/acs.analchem.8b04359.
144. C.-Y. Chang and J.-T. Shy, Appl. Opt. **54**, 8526 (2015), DOI: 10.1364/AO.54.008526.
145. Y. Wang, M. Nikodem, E. Zhang, F. Cikach, J. Barnes, S. Comhair, R. a Dweik, C. Kao, and G. Wysocki, Sci. Rep. **5**, 9096 (2015), DOI: 10.1038/srep09096.
146. H. Ganser, W. Urban, and J. Brown, Mol. Phys. **101**, 545 (2003), DOI: 10.1080/00268970210159460.
147. W. Zhao, B. Fang, X. Lin, Y. Gai, W. Zhang, W. Chen, Z. Chen, H. Zhang, and W. Chen, Anal. Chem. **90**, 3958 (2018), DOI: 10.1021/acs.analchem.7b04949.
148. D. Jacob, M. Vallet, F. Bretenaker, A. Le Floch, and R. Le Naour, Appl. Phys. Lett. **66**, 3546 (1995), DOI: 10.1063/1.113811.
149. R. Engeln, G. Berden, E. van den Berg, and G. Meijer, J. Chem. Phys. **107**, 4458 (1998), DOI: 10.1063/1.474808.
150. J. Westberg and G. Wysocki, Appl. Phys. B **123**, 168 (2017), DOI: 10.1007/s00340-017-6743-6.
151. B. Brumfield and G. Wysocki, Opt. Express **20**, 29727 (2012), DOI: 10.1364/oe.20.029727.
152. Y. Wang, M. Nikodem, and G. Wysocki, Opt. Express **21**, 741 (2013), DOI: 10.1364/OE.21.000740.
153. C. A. Zaugg, R. Lewicki, T. Day, R. F. Curl, and F. K. Tittel, Proc. SPIE **7945**, 79450O (2010), DOI: 10.1117/12.874819.
154. S. Borri, P. Patimisco, I. Galli, D. Mazzotti, G. Giusfredi, N. Akikusa, M. Yamanishi, G. Scamarcio, P. De Natale, and V. Spagnolo, Appl. Phys. Lett. **104**, 091114 (2014), DOI: 10.1063/1.4867268.
155. B. Baumgartner, J. Hayden, J. Loizillon, S. Steinbacher, D. Grosso, and B. Lendl, Langmuir (2019), DOI: 10.1021/acs.langmuir.9b01435.
156. A. A. Kosterev, T. S. Mosely, and F. K. Tittel, Appl. Phys. B **85**, 295 (2006), DOI: 10.1007/s00340-006-2355-2.
157. L. Dong, R. Lewicki, K. Liu, P. R. Buerki, M. J. Weida, and F. K. Tittel, Appl. Phys. B **107**, 275 (2012), DOI: 10.1007/s00340-012-4949-1.
158. N. Truong, S. Büscher, F. Kühnemann, and M. A. Harith, in *AIP Conf. Proc.* (AIP, 2009), pp. 3–8.
159. J. Fischer, R. R. Gamache, A. Goldman, L. S. Rothman, and A. Perrin, J. Quant. Spectrosc. Radiat. Transf. **82**, 401 (2003), DOI: 10.1016/S0022-4073(03)00166-3.
160. R. T. V. Kung and R. E. Center, J. Chem. Phys. **62**, 2187 (1975), DOI: 10.1063/1.430786.
161. M. E. Whitson and R. J. McNeal, J. Chem. Phys. **66**, 2696 (1977), DOI: 10.1063/1.434217.
162. R. Frey, J. Lukasik, and J. Ducuing, Chem. Phys. Lett. **14**, 514 (1972), DOI: 10.1016/0009-2614(72)80252-5.
163. S. Matteuci, Y. Yampolskii, B. D. Freeman, and I. Pinnau, in *Membr. Gas Vap. Sep.*, edited by Y. Yampolskii, I. Pinnau, and B. Freeman (John Wiley & Sons, Ltd, 2015), pp.

1–47.
164. I. Galli, S. Bartalini, R. Ballerini, M. Barucci, P. Cancio, M. De Pas, G. Giusfredi, D. Mazzotti, N. Akikusa, and P. De Natale, Optica **3**, 385 (2016), DOI: 10.1364/OPTICA.3.000385.
165. M. Hippler, C. Mohr, K. A. Keen, and E. D. McNaghten, J. Chem. Phys. **133**, 044308 (2010), DOI: 10.1063/1.3461061.
166. K. M. Manfred, L. Ciaffoni, and G. A. D. Ritchie, Appl. Phys. B-Lasers Opt. **120**, 329 (2015), DOI: 10.1007/s00340-015-6140-y.
167. V. Motto-Ros, M. Durand, and J. Morville, Appl. Phys. B **91**, 203 (2008), DOI: 10.1007/s00340-008-2950-5.
168. C. C. Chan and T. Tamir, Opt. Lett. **10**, 378 (1985), DOI: 10.1364/ol.10.000378.
169. W. Rigrod, IEEE J. Quantum Electron. **19**, 1679 (1983), DOI: 10.1109/JQE.1983.1071787.
170. T. Tomberg, T. Hieta, M. Vainio, and L. Halonen, Analyst **144**, 2291 (2019), DOI: 10.1039/C9AN00058E.
171. V. Motto-Ros, J. Morville, and P. Rairoux, Appl. Phys. B **87**, 531 (2007), DOI: 10.1007/s00340-007-2618-6.
172. S. Ohshima and H. Schnatz, J. Appl. Phys. **71**, 3114 (1992), DOI: 10.1063/1.351006.
173. J. C. Habig, J. Nadolny, J. Meinen, H. Saathoff, and T. Leisner, Appl. Phys. B **106**, 491 (2012), DOI: 10.1007/s00340-011-4804-9.
174. S. G. Baran, G. Hancock, R. Peverall, G. A. D. Ritchie, and N. J. Van Leeuwen, Analyst **134**, 243 (2009), DOI: 10.1039/b811793d.
175. J. P. Waclawek, H. Moser, and B. Lendl, Opt. Express **24**, 6559 (2016), DOI: 10.1364/OE.24.006559.
176. F. J. M. Harren, F. G. C. Bijnen, J. Reuss, L. A. C. J. Voesenek, and C. W. P. M. Blom, Appl. Phys. B **50**, 137 (1990), DOI: 10.1007/BF00331909.
177. S. Schäfer, A. Miklós, A. Pusel, and P. Hess, Chem. Phys. Lett. **285**, 235 (1998), DOI: 10.1016/S0009-2614(98)00032-3.
178. X. Yin, L. Dong, H. Wu, H. Zheng, W. Ma, L. Zhang, W. Yin, S. Jia, and F. K. Tittel, Sensors Actuators B Chem. **247**, 329 (2017), DOI: 10.1016/J.SNB.2017.03.058.
179. G. Giusfredi, I. Galli, D. Mazzotti, P. Cancio, and P. De Natale, J. Opt. Soc. Am. B **32**, 2223 (2015), DOI: 10.1364/JOSAB.32.002223.
180. T. Hausmaninger, W. Ma, and O. Axner, ArXiv (2018).
181. T. Hausmaninger, G. Zhao, W. Ma, and O. Axner, J. Quant. Spectrosc. Radiat. Transf. **205**, 59 (2018), DOI: 10.1016/J.JQSRT.2017.10.007.
182. O. Axner, P. Kluczynski, and Å. M. Lindberg, J. Quant. Spectrosc. Radiat. Transf. **68**, 299 (2001), DOI: 10.1016/S0022-4073(00)00032-7.
183. G. Giusfredi, S. Bartalini, S. Borri, P. Cancio, I. Galli, D. Mazzotti, and P. De Natale, Phys. Rev. Lett. **104**, 110801 (2010), DOI: 10.1103/PhysRevLett.104.110801.
184. F. J. M. Harren, F. G. C. Bijnen, J. Reuss, L. A. C. J. Voesenek, and C. W. P. M. Blom, Appl. Phys. B Photophysics Laser Chem. **50**, 137 (1990), DOI: 10.1007/BF00331909.
185. D. S. Baer, J. B. Paul, M. Gupta, and A. O'Keefe, Appl. Phys. B **75**, 261 (2002), DOI: 10.1007/s00340-002-0971-z.
186. A. A. Kosterev, Y. A. Bakhirkin, F. K. Tittel, S. Blaser, Y. Bonetti, and L. Hvozdara, Appl. Phys. B **78**, 673 (2004), DOI: 10.1007/s00340-004-1519-1.

187. J. Courtois, K. Bielska, and J. T. Hodges, J. Opt. Soc. Am. B **30**, 1486 (2013), DOI: 10.1364/JOSAB.30.001486.
188. G. C. Bjorklund, M. D. Levenson, W. Lenth, and C. Ortiz, Appl. Phys. B Photophysics Laser Chem. **32**, 145 (1983), DOI: 10.1007/BF00688820.
189. C. E. Wieman and L. Hollberg, Rev. Sci. Instrum. **62**, 1 (1991), DOI: 10.1063/1.1142305.
190. R. Terabayashi, V. Sonnenschein, H. Tomita, N. Hayashi, S. Kato, L. Jin, M. Yamanaka, N. Nishizawa, A. Sato, K. Nozawa, K. Hashizume, T. Oh-hara, and T. Iguchi, Hyperfine Interact. **238**, 1 (2017), DOI: 10.1007/s10751-016-1390-6.